PB86-116530

System for Measurement of Small Vibrations at Material Interfaces Induced by Electrostrictive Forces

(U.S.) Health Effects Research Lab.
Research Triangle Park, NC

Oct 85

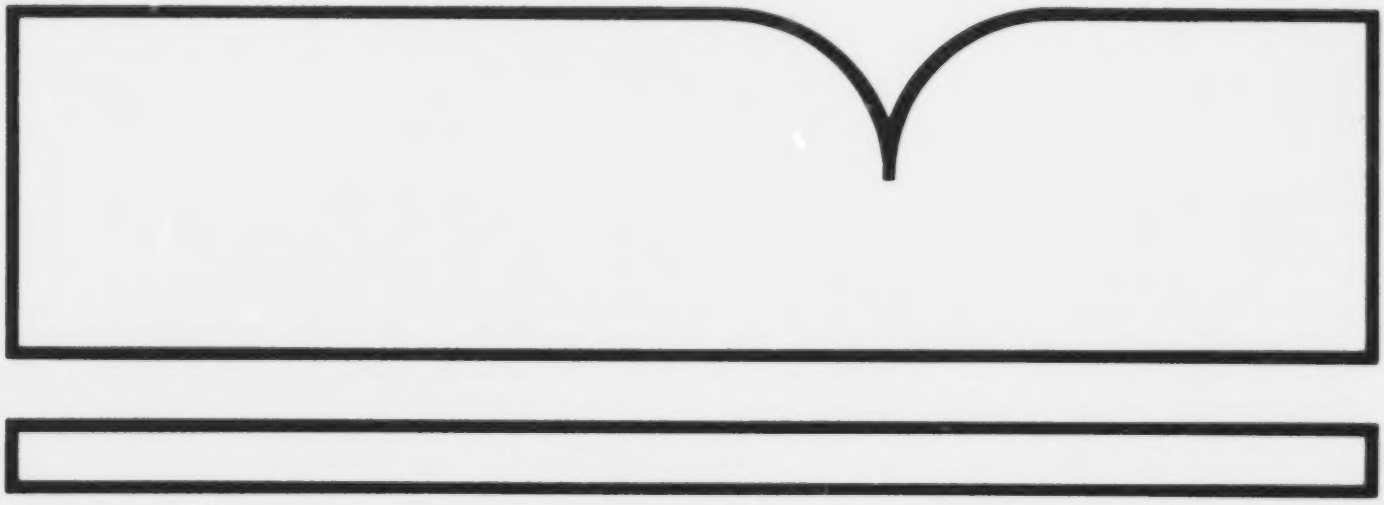

U.S. Department of Commerce
National Technical Information Service
NTIS

PB86-116530

EPA/600/1-85/021
October 1985

A SYSTEM FOR MEASUREMENT OF SMALL VIBRATIONS AT MATERIAL INTERFACES INDUCED BY ELECTROSTRICTIVE FORCES

by

Joseph S. Ali and William T. Joines

Experimental Biology Division
Health Effects Research Laboratory
Research Triangle Park, NC 27711

Health Effects Research Laboratory
Office of Research and Development
U.S. Environmental Protection Agency
Research Triangle Park, North Carolina 27711

REPRODUCED BY
NATIONAL TECHNICAL
INFORMATION SERVICE
U.S. DEPARTMENT OF COMMERCE
SPRINGFIELD, VA. 22161

TECHNICAL REPORT DATA
(Please read Instructions on the reverse before completing)

1. REPORT NO.	2.	3. RECIPIENT'S ACCESSION NO.
EPA/600/1-85/021		PB86 116530/AS

4. TITLE AND SUBTITLE	5. REPORT DATE
A SYSTEM FOR MEASUREMENT OF SMALL VIBRATIONS AT MATERIAL INTERFACES INDUCED BY ELECTROSTRICTIVE FORCES	October 1985
	6. PERFORMING ORGANIZATION CODE
7. AUTHOR(S)	8. PERFORMING ORGANIZATION REPORT NO.
Joseph S. Ali and William T. Joines	
9. PERFORMING ORGANIZATION NAME AND ADDRESS	10. PROGRAM ELEMENT NO.
same as #12	ACGF1A
	11. CONTRACT/GRANT NO.
12. SPONSORING AGENCY NAME AND ADDRESS	13. TYPE OF REPORT AND PERIOD COVERED
Health Effects Research Laboratory Office of Research and Development U.S. Environmental Protection Agency Research Triangle Park, NC 27711	14. SPONSORING AGENCY CODE EPA/600/11

15. SUPPLEMENTARY NOTES

16. ABSTRACT

The mechanisms of interaction of ELF and ELF-modulated RF fields with biological systems is presently an active area of research. Some models propose that field-induced forces may influence certain observed biological effects such as RF hearing and calcium ion efflux. To investigate the validity of the field-induced force model for the calcium-ion efflux effect, a system is needed which is capable of exposing samples to ELF fields or to ELF-modulated RF fields. At the same time the induced vibration caused by the forces of electrostriction must be monitored, preferably by a noncontacting method.

A microwave phase-sensitive receiver was designed to sense the small vibrations. Limitations on the receiver sensitivity imposed by phase noise is discussed. Phase noise measurement systems were designed and used to characterize the key receiver components. A limiting amplifier in the IF section of the receiver eliminates the need for knowledge of the reflection coefficient of the object of interest for quantitative vibration measurements.

A special exposure cell is described which is a section of X-band waveguide which has been modified by the addition of a center conductor to form a rectangular transmission line. The center conductor with a sample placed under the waveguide broad wall is excited by a low-frequency or low-frequency amplitude modulated signal. In addition an X-band signal is fed through the waveguide, scattered by the sample and detected by the phase-sensitive receiver.

The fields and the resulting forces on certain standard shaped samples are derived. With the measurement of the Young's modulus and Poisson's ratio of the samples, the resulting vibration amplitude of the field-induced vibration is estimated. Actual vibration measurements verified with a piezoelectric crystal indicate a vibration sensitivity of about 1 nanometer peak-to-peak. Vibrations in this range were predicted to occur in certain calcium-ion efflux studies. This system therefore promises to help unravel some of the uncertainties surrounding the interaction of RF fields with biological systems.

17. KEY WORDS AND DOCUMENT ANALYSIS

a. DESCRIPTORS	b. IDENTIFIERS/OPEN ENDED TERMS	c. COSATI Field/Group

18. DISTRIBUTION STATEMENT	19. SECURITY CLASS *(This Report)*	21. NO. OF PAGES
RELEASE TO PUBLIC	UNCLASSIFIED	159
	20. SECURITY CLASS *(This page)*	22. PRICE
	UNCLASSIFIED	

EPA Form 2220-1 (Rev. 4-77) PREVIOUS EDITION IS OBSOLETE

NOTICE

This document has been reviewed in accordance with U.S. Environmental Protection Agency policy and approved for publication. Mention of trade names or commercial products does not constitute endorsement or recommendation for use.

FOREWORD

The many benefits of our modern, developing, industrial society are accompanied by certain hazards. Careful assessment of the relative risk of existing and new man-made environmental hazards is necessary for the establishment of sound regulatory policy. These regulations serve to enhance the quality of our environment in order to promote the public health and welfare and the productive capacity of our Nation's population.

The complexities of environmental problems originate in the deep interdependent relationships between the various physical and biological segments of man's natural and social world. Solutions to these environmental problems require an integrated program of research and development using input from a number of disciplines. The Health Effects Research Laboratory, Research Triangle Park, NC and Cincinnati, OH conducts a coordinated environmental health research program in toxicology, epidemiology and clinical studies using human volunteer subjects. A wide range of pollutants known or suspected to cause health problems are studied. The research focuses on air pollutants, water pollutants, toxic substances, hazardous wastes, pesticides, and non-ionizing radiation. The laboratory participates in the development and revision of air and water quality criteria and health assessment documents on pollutants for which regulatory actions are being considered. Direct support to the regulatory function of the Agency is provided in the form of expert testimony and preparation of affidavits as well as expert advice to the Administrator to assure the adequacy of environmental regulatory decisions involving the protection of the health and welfare of all U.S. inhabitants.

F. Gordon Hueter, Ph.D.
Director
Health Effects Research Laboratory

ABSTRACT

The mechanisms of interaction of ELF and ELF-modulated RF fields with biological systems is presently an active area of research. Some models propose that field-induced forces may influence certain observed biological effects such as RF hearing and calcium ion efflux. To investigate the validity of the field-induced force model for the calcium-ion efflux effect a system is needed which is capable of exposing samples to ELF fields or to ELF-modulated RF fields. At the same time the induced vibration caused by the forces of electrostriction must be monitored preferably by a noncontacting method.

A microwave phase-sensitive receiver was designed to sense the small vibrations. Limitations on the receiver sensitivity imposed by phase noise is discussed. Phase noise measurement systems were designed and used to characterize the key receiver components. A limiting amplifier in the IF section of the receiver eliminates the need for knowledge of the reflection coefficient of the object of interest for quantitative vibration measurements.

A special exposure cell is described which is a section of X-band waveguide which has been modified by the addition of a center conductor to form a rectangular transmission line. The center conductor with a sample placed under the waveguide broad wall is excited by a low-frequency or low-frequency amplitude modulated signal. In addition an X-band signal is fed through the waveguide, scattered by the sample and detected by the phase-sensitive receiver.

The fields and the resulting forces on certain standard shaped samples are derived. With the measurement of the Young's modulus and Poisson's ratio of the samples, the resulting vibration amplitude of the field-induced vibration is estimated. Actual vibration measurements verified with a piezoelectric crystal indicate a vibration sensitivity of about 1 nanometer peak-to-peak.

Vibrations in this range were predicted to occur in certain calcium-ion efflux studies. This system therefore promises to help unravel some of the uncertainties surrounding the interaction of RF fields with biological systems.

This report covers a period from October 1, 1982 to April 15, 1985 and work was completed as of April 15, 1985.

CONTENTS

	Page
Foreword	iii
Abstract	iv
Figures	ix
Tables	xii
Acknowledgements	xiii
I. Introduction	1
II. Signal Scattered from a Linearly Vibrating Rigid Body	7
III. Receiver Design	12
3.1 Receiving Systems	12
3.1.1 Doppler Transceiver	12
3.1.2 Homodyne Receiver	15
3.1.3 Sideband Heterodyne Receiver	16
Basic Operation	16
Low Noise Baseband Amplifier	20
Low Pass Filter Design	29
3.2 Sensitivity of the Sideband Heterodyne Receiver	32
3.2.1 Phase Noise	32
Detection of Phase Noise	35
Residual Phase Noise of the RF Amplifier	39
Residual Phase Noise of the Limiting Amplifier	45
Residual Phase Noise of the Low Noise IF Amplifier	49
Residual Phase Noise of Mixers	49
3.2.2 Oscillator Phase Noise	55
3.2.3 Mixer Conversion Loss Reduction	56

Page

3.2.4 Overall Receiver Sensitivity. 59

3.3 Calibration. 65

IV. Exposure Cell Design. 71

4.1 Exposure Cell Design Approach. 71

4.2 Properties of the Exposure Cell. 71

4.3 Performance. 77

V. Deflection of Tissue Models 81

5.1 Derivation of Electrostrictive (Maxwell Stress) Force. . . 81

5.2 Force at a Dielectric Interface. 83

5.3 E Field Normal to the Surface of a Dielectric Ellipsoid in a Uniform Field 86

5.3.1 Special Case: Spheroid 91

5.3.2 Special Case: Prolate Spheroid 93

5.4 Derivation of the Vertical Force on a Half-Prolate Spheroid with its Base on a Ground Plane 96

5.5 Calculation of Displacement and Expected Receiver Signal . 99

5.5.1 Mechanics of Elastic Bodies 99

5.5.2 Approximation of a Half-Prolate Spheroid by a Prismatic Bar 100

5.5.3 Measurement of Young's Modulus and Poisson's Ratio for Agar Gels 103

5.5.4 Calculation of Displacement 109

5.5.5 Calculation of Expected Receiver Signal 111

5.6 Measurement of Displacement. 112

5.6.1 Experimental Data: Displacement of Half-Prolate Spheroid. 112

5.6.2 Experimental Data: Resonance Frequencies 120

VI. Conclusions 128

Page

Appendix A Correlation Effect or the Reduction in Apparent Oscillator Noise at Close Range 133

References 139

FIGURES

Number		Page
2-1	A Linearly Vibrating Object in the Presence of an RF Field.	8
2-2	The One-Sided Line Spectra of the Signal Received from the Scattered Field of a Linearly Vibrating Object	8
3-1	Diagram of the Microwave Associates Model MA-86502 Doppler Transceiver.	13
3-2	Diagram of a Homodyne Receiver with a Manual Phase Shifter.	13
3-3	Block Diagram of the Sideband Heterodyne Receiver Used for All Experimental Work	17
3-4	Frequency Response of Filter F1 Used to Derive the Receiver Local Oscillator Signal	19
3-5	Schematic Drawing of the Low Noise Baseband Amplifier. . . .	21
3-6	Frequency Response of the Low Noise Baseband Amplifer. . . .	22
3-7	Model for Analysis of the Noise Characteristics of the Low Noise Baseband Amplifier..	24
3-8a	Low Pass Prototype Butterworth Filter.	30
3-8b	Low Pass Butterworth Filter.	30
3-9	Frequency Response of the Low Pass Butterworth Filter. . . .	31
3-10	Typical Phase Noise Spectrum of an Oscillator.	33
3-11	The Received Signal from a Doppler Radar Swamped by Oscillator Phase Noise	33
3-12	Block Diagram of Quadrature Phase Detection Method for the Measurement of Phase Noise	37
3-13	General Residual Phase Noise Measurement Circuit	40
3-14	Experimental Setup for Residual Phase Noise Measurements . .	41

FIGURES (continued)

Number		Page
3-15	Residual Phase Noise of the Magnum Microwave Model MO 64P Mixer and the Miteq Model AMF-3B-8012-4 Low Noise RF Amplifier	42
3-16	Relationship Between Two Power Levels and Their Sum (in dB).	44
3-17a	Circuit for Measurement of Basic System Sensitivity for Residual Phase Noise Measurements for Devices Which Operate at 30 MHz	46
3-17b	Circuit for Measurement of the Residual Phase Noise of Devices Which Operate at 30 MHz.	46
3-18	Residual Phase Noise of the Limiting Amplifier for a Series of RF Drive Levels	47
3-19	Residual Phase Noise of the Low Noise IF Amplifier.	48
3-20	Noise of the 30 MHz Phase Detector for a Series of RF Drive Levels	50
3-21	Residual Phase Noise of the 30 MHz Phase Detector for a Series of RF Drive Levels	51
3-22	Phase Detector Constant ($k\phi$) Versus RF Port Input Level at 6 mW LO Power.	53
3-23	Single Sideband Phase Noise of the Receiver System Oscillators	54
3-24	Conversion Loss of the Magnum Model MO 64P Mixer Versus RF Input for a Series of LO Power Levels	57
3-25	Conversion Loss of the Anaren Model 7H0118 Mixer with and without DC Bias.	58
3-26	Receiver Sensitivity Versus Carrier Offset Frequency for a Series of Signal Strengths.	61
3-27	Receiver Sensitivity Versus Carrier Offset Frequency with Time Averaging	67
4-1	The Exposure Cell	72
4-2	Waveguide Cross-Section	74
4-3	Diagram of the First Few Field Modes of WR-112 Waveguide	74

FIGURES (continued)

Figure		Page
4-4	Exposure Cell Cross-Section	74
4-5	Exposure Cell Return Loss at the Coaxial Port	79
4-6	Exposure Cell TDR Plot at the Coaxial Port.	80
5-1	Field Vector Definitions for Fields Normal to a Dielectric Interface.	84
5-2	Field Vector Definitions for Fields Parallel to a a Dielectric Interface.	84
5-3	A Dielectric Ellipsoid in an Electric Field	87
5-4	Approximation of a Half-Prolate Spheroid by a Prismatic Bar	101
5-5	Apparatus for Measurement of Young's Modulus.	104
5-6	Young's Modulus Versus Concentration for Agar Gels. . . .	108
5-7	Half-Prolate Spheroid Molds	114
5-8	Measured Single Sideband to Carrier Ratio and Vibration Amplitude Versus Vibration Frequency for the 0.6% Agar Gel, 2 mm Dia. Base Half-Prolate Spheroid.	117
5-9	Measured Single Sideband to Carrier Ratio and Vibration Amplitude Versus Vibration Frequency for the 0.6% Agar Gel, 3.5 mm Dia. Base Half-Prolate Spheroid.	118
5-10	Measured Single Sideband to Carrier Ratio and Vibration Amplitude Versus Vibration Frequency for the 0.6 Agar Gel, 5 mm Dia. Base Half-Prolate Spheroid.	119
5-11	Measured Single Sideband to Carrier Ratio and Vibration Amplitude Versus Vibration Frequency for the 0.6% Agar Gel, 2 mm Cube.	126
5-12	Measured Single Sideband to Carrier Ratio and Vibration Amplitude Versus Vibration Frequency for the 0.6% Agar Gel, 4 mm Cube.	127
A-1	A Simple Radar System for Analysis of the Correlation Effect.	134

TABLES

Number		Page
3-1	Noise Specifications for the Precision Monolithics, Inc., Model OP-27FZ Operational Amplifier	26
3-2	Comparison of the Receiver Sensitivity Calculated from the Noise Figure and the Actual Receiver Sensitivity at Selected Carrier Offset Frequencies for a Series of Carrier Signal Levels	63
3-3	Mixer M2 Conversion Loss and Calculated Receiver Noise Figure for a Series of Signal Levels.	64
3-4	Comparison of Measured and Expected Single-Sideband Carrier Ratios (SSBCR) for a Series of Received Power Levels.	70
5-1	Experimental Data for the Determination of Young's Modulus of Agar Gels.	105
5-2	Experimental Data for the Determination of Poisson's Ratio of 0.6% c Agar Gel.	106
5-3	Comparison of Calculated and Measured Vibration Amplitudes in the Sub-Resonant Region for 0.6% Agar Gel Half-Prolate Spheroid Samples on a Ground Plane in an 8.33 kV/m Electric Field.	115
5-4	Comparison of the Measured Major Resonance Frequencies of 0.6% Agar Gel Half-Prolate and Cubical Shaped Samples with Those Obtained from Basic Vibration Models of Elastic Bodies.	121
A-1	Apparent Reduction in Oscillator Noise.	138

ACKNOWLEDGEMENTS

The authors are indebted to Professors Rhett T. George, Robert B. Kerr, Loren W. Nolte and Thomas M. Gallie, all of Duke University, and Edwin Mantiply who read the manuscript and offered many valuable comments. We also acknowledge the contributions of Drs. Ronald J. Spiegel and Carl F. Blackman for their helpful suggestions during the course of the work, and of Paul Killough for constructing the gell molds, E. Baker Bailey for fabricating the electronic circuitry, Barbara Crabtree for producing a high quality manuscript with limited equipment, and the EPA Graphics Department for preparing the figures.

Chapter I

INTRODUCTION

It was only about ten years ago that there was an active debate within the non-ionizing radiation bioeffects research community on the possible existence of non-thermal biological effects [Schwan, 1972]. Today the debate has been quelled and attention is now focused on the discovery of the mechanisms of interaction of EM fields with organisms which will explain the phenomena observed in the last ten years at field intensities well below thermalizing levels [Adey, 1981; Barnes, 1977]. Among these low level effects are defects in developing chick embryos with pulse-modulated magnetic fields [Delgado et al, 1982]; changes in the chromosomes of an insect called the midge with radiation between 64 and 69 GHz [Kremer et al, 1983] and calcium ion efflux from chick brains in vitro [Bawin et al, 1975]. The calcium ion efflux effect has been observed in vitro with modulated fields of a few nanowatts per square centimeter in air. The effect has also been observed with the direct exposure to ELF fields [Blackman et al, 1982]. Simply stated, ELF fields and amplitude modulated RF fields can affect the flow of calcium ions from the brain cells to which they are loosely bound. The effect may have health implications because calcium ions play a powerful role in the excitation of nerve impulses [Lerner, 1984]. The calcium ion efflux is known to occur in the outermost two millimeters of the chick brain tissue [Blackman et al, 1983]. One view of the cell membranes envisions a "field of lipid (fat) with rocks of protein that float around in the fat and protrude outward and inward like a field of corn" [Lerner, 1984] with calcium ions loosely bound to these proteins. One

can easily envision these loosely bound calcium ions being shaken off the cell membrane if the membrane were to be set in motion.

One mechanism of interaction relying on the concept of a mechanical vibration influencing the efflux of calcium has been proposed by Spiegel [1982; 1983]. Earlier work by Joines et al [1981] had shown that field-induced forces within the organ of Corti (in the inner ear) could be strong enough to evoke RF hearing effects at power densities near the threshold of these sensations. Spiegel's model suggests that when a dielectric object (a chick brain) is surrounded by a medium with a dielectric constant which differs from that of the object and is immersed in an alternating electric field, the forces of electrostriction cause a pressure on the surface of the object. The pressure causes a mechanical deformation of the object which may influence the binding of calcium ions to the surface of the brain. Spiegel calculated the range of the deformation to be between 1.0 nm and 100 nm for an incident power density of 1.0 mW/cm^2. Power densities near this level were used by Blackman et al [1980] in a calcium-ion efflux study of ELF-modulated, 147 MHz radiofrequency radiation. In Spiegel's model the calcium ions may either be shaken off by the vibration or squeezed out by the accompanying volume change of the brain. No experimental work has yet been done to test the validity of this model.

To investigate the validity of this field-induced force model, a system was needed which is capable of exposing samples to ELF fields or to ELF-modulated RF fields. At the same time the induced vibration caused by the forces of electrostriction must be monitored preferably by a noncontacting method. A microwave phase-sensitive receiver was the type of device envisioned as a possible remote sensor of mechanical vibration. It is undesirable to use contacting monitoring methods because the sensor would distort the

applied electric field thereby altering the exposure environment.

Rather than using chick brains in the development phase for the exposed object which have irregular shapes, are complex and have charged molecules protruding from their surfaces, a homogeneous, regularly shaped material was used which had mechanical properties similar to brain tissue. With regular geometrically shaped samples, the field at the surface of the object is amenable to analytical solution.

An exposure cell was needed which would facilitate the exposure of samples to the alternating fields while also permitting the exposure of the sample to an interrogating field to monitor the vibration. The exposure cell should provide a uniform exposure field over a volume large enough to accomodate the sample. The exposure cell should also have a frequency range of up to about 500 MHz to enable the application of either ELF or ELF-modulated fields to the samples.

A fundamental requirement for the receiver or vibration detector was that it be well characterized in its performance. It was particularly important to know the limits of the receiver sensitivity in terms of its ability to measure vibration amplitudes. This knowledge would permit setting an upper limit on what motion might be caused by electrostrictive forces if no motion were observed in a particular experiment. It is also of interest to identify the receiver components that limit receiver sensitivity and the reasons involved. With this information subsequent redesigns of refinement efforts could be properly directed. Consequently an analysis of the receiver sensitivity became an area of focus.

A calibrated receiver was desired for this work. This would permit quantitative vibration amplitude measurements which could be compared to

calculated values for simple models with standard shapes. As will be seen, quantitative measurement capability can be achieved but not without some loss in sensitivity. A desirable feature of the receiver is for it to have a calibration channel. Some "standard vibrator" should be provided for which the vibration amplitude is known and which can be used to verify the accuracy of measured vibration amplitudes. The standard should be capable of vibrating over the frequency and amplitude ranges expected of the tissue models while under electric field exitation.

To substantiate that electrostrictive forces are the cause of any observed vibration, the forces on the dielectric object due to the applied electric field should be calculated (which in turn requires a determination of the surface electric fields). The calculated force can then be used to determine the motion of the test object. Once the motion is known, the expected receiver signal can be calculated. This can then be compared to the measured receiver signal.

There have been a variety of microwave receivers designed for motion detection. These instruments are generally referred to as Doppler radars or as microwave interferometers. Although in many cases the hardware implementation for either type of receiver is the same, this author prefers to reserve the term Doppler radar for the traditional application in which the target is either approaching or receding from the transmitter continuously. In this case the carrier frequency of the reflected signal is indeed shifted from that of the transmitter frequency. For the case of vibratory motion, the carrier frequency of the return signal is not shifted and hence the term Doppler radar seems inappropriate. Interferometers on the other hand whether optical or RF always rely on phase comparisons with a reference path signal.

There exists a considerable body of work in the area of microwave interferometers for vibration measurements. Some of this work has been directed towards biomedical applications [Bramanti, 1981; Buchan et al, 1979; Marsden et al, 1979]. Stuckly et al [1979] used a Doppler transceiver at X-band to monitor arterial wall movement of peripheral arteries. The receiver was not calibrated for measurement of displacement; however the study did demonstrate that the system had sufficient sensitivity to detect the desired signal. Later work by Thansandote et al [1982] compared microwave interferometers operating at 9.3 GHz and 915 MHz in applications similar to the earlier work by Stuchly. The 915 MHz interferometer was able to detect a vibrating object deeper in a medium, however the sensitivity was greater with the 9.3 GHz unit. Griffin [1978] used a microwave interferometer based on a three port circulator to measure chest movement during respiration, hand tremors and movement of the lower limbs due to the arterial pulse. His design achieved a calibrated displacement measurement; however accurate positioning of the subject relative to the antenna was required. Sensitivity of Griffin's design was on the order of 1 mm.

Kleinman et al [1979] designed a receiver for measuring the scattered signal from a linearly oscillating object in a 10 GHz plane wave. The receiver had three signal processing paths and could function as an AM receiver, a phase-sensitive receiver or as a synchronous receiver. The test object was a 5 3/4 inch diameter aluminum disk attached to a vibrator and placed seven feet from the antennas of the transmitter and receiver. The receiver when used in the phase-sensitive mode could detect as little as 25 μ vibration of the disk.

Optical techniques [Drain, 1980] have achieved extraordinary vibration sensitivities. A laser interferometer system [Brown et al, 1983] designed to

optically measure the physical motion induced by a microwave pulse on the lens of a rat's eye had a sensitivity in vibration measurements of 2 nm. A fiber-optic interferometer [Drake et al, 1984] designed to measure the vibration of the tympanic membrane of a live cricket achieved a sensitivity of about 1 nm. The fiber-optic approach eliminated the need for inconvenient mirror alignment for illumination of confined areas with the laser beam. An electronically stabilized laser interferometer was built by Luymes [1983] to measure the small electrostrictive strains of hard crystals such as diamond and quartz. This system, based on the Michelson interferometer, was very complicated but yielded a sensitivity of 10^{-4} nm.

Although greater sensitivity can in general be obtained with optical techniques than with microwaves, preliminary work with a microwave system indicated that a sensitivity comparable to all but the Luymes interferometer could be obtained with a microwave system at far less cost.

Chapter II

SIGNAL SCATTERED FROM A LINEARLY VIBRATING RIGID BODY

A rigid body, A, with position

$$x(t) = x_o \sin \omega_m t \qquad (2\text{-}1)$$

is assumed centered at the origin of a rectangular coordinate system and vibrating sinusoidally along the x-axis with radian frequency ω_m and amplitude x_o as shown in Fig. 2-1. An RF source located at (+d, 0) illuminates the vibrating object with a continuous E-M wave travelling from S to A. A portion of the radiation incident upon A will be scattered back to the source, S. We wish to examine the effect of the linearly vibrating object on the reflected wave received by S. A similar problem was analyzed by Alexander [1980] in a study of the spectrum signatures of aircraft and missiles.

If the signal at the source is

$$V_o \sin \omega t \qquad (2\text{-}2)$$

then at that instant the phase of the signal at A is

$$\phi_A(t) = \omega t - \frac{2\pi}{\lambda}(d-x(t)) \qquad (2\text{-}3)$$

where λ is the wavelength of the transmitted wave. The phase of the signal at the receiver reflected from the target is

$$\phi_{S(ref)}(t) = \omega t - 2(\frac{2\pi}{\lambda})(d-x(t)). \qquad (2\text{-}4)$$

The return signal at the source after travelling path SAS is

$$V_{rec} = \rho V_o \sin(\omega t - 2(\frac{2\pi}{\lambda})(d-x(t))) \qquad (2\text{-}5)$$

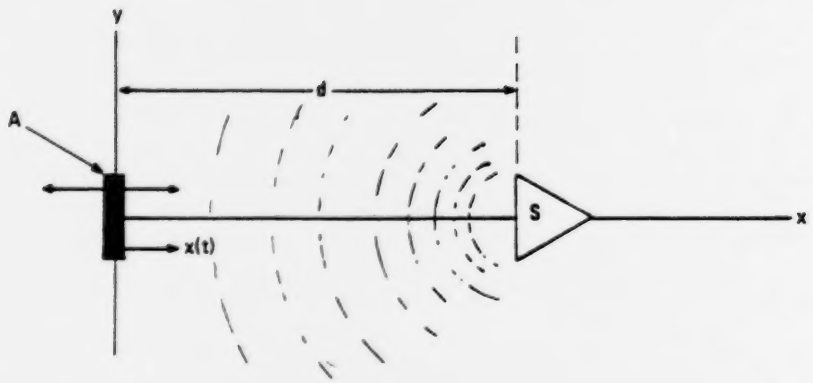

Figure 2-1. A Linearly Vibrating Object in the Presence of an RF Field.

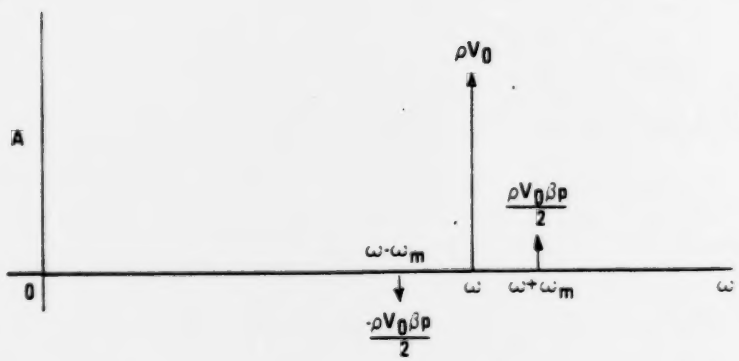

Figure 2-2. The One-Sided Line Spectra of the Signal Received from the Scattered Field of a Linearly Vibrating Object.

where ρ is the ratio of the amplitude of the received signal to the amplitude of the signal at the source. Rearranging terms gives

$$V_{rec} = \rho V_o \sin(\omega t + \frac{4\pi x(t)}{\lambda} - \frac{4\pi d}{\lambda}) \quad .(2\text{-}6)$$

or

$$V_{rec} = \rho V_o \sin(\omega t + \frac{2\omega}{c} x(t)) \quad (2\text{-}7)$$

where the constant phase shift term has been dropped. If x(t) is a sinusoidal vibration, then V_{rec} is

$$V_{rec} = \rho V_o \sin(\omega t + \frac{2\omega}{c} x_o \sin \omega_m t). \quad (2\text{-}8)$$

Let

$$\beta_p \equiv \frac{2\omega}{c} x_o \quad (2\text{-}9)$$

where β_p is the phase modulation index. Then

$$V_{rec} = \rho V_o \sin(\omega t + \beta_p \sin \omega_m t). \quad (2\text{-}10)$$

Eq. 2-10 can be identified as a phase modulated wave [Carlson, 1975, p. 240] since the phase is proportional to the message, $x_o \sin \omega_m t$.

To insure unambigious demodulation

$$\beta \leq \pi \text{ radians.} \quad (2\text{-}11)$$

Expanding Eq. 2-10

$$V_{rec} = \rho V_o [\sin \omega t \cos(\beta_p \sin \omega_m t) + \cos \omega t \sin(\beta_p \sin \omega_m t)]. \quad (2\text{-}12)$$

But

$$\cos(\beta_p \sin \omega_m t) = J_o(\beta_p) + \sum_{n \text{ even}}^{\infty} 2J_n(\beta_p)\cos n\omega_m t \quad (2\text{-}13)$$

and

$$\sin(\beta_p \sin \omega_m t) = \sum_{n \text{ odd}}^{\infty} 2 J_n(\beta_p)\sin n\omega_m t \quad (2\text{-}14)$$

where $J_n(\beta_p)$ is the Bessel function of the first kind. Substituting Eq. 2-13

and Eq. 2-14 into Eq. 2-12 we get

$$V_{rec} = \rho V_o \sin \omega t[J_o(\beta_p) + \sum_{n \text{ even}}^{\infty} 2 J_n(\beta_p) \cos n\omega_m t]$$

$$+ \rho V_o \cos \omega t [\sum_{n \text{ odd}}^{\infty} 2 J_n(\beta_p) \sin n\omega_m t] \quad (2\text{-}15)$$

or

$$V_{rec} = \rho V_o[J_o(\beta_p)\sin \omega t + 2 J_1(\beta_p)\cos \omega t \sin \omega_m t$$
$$+ 2J_2(\beta_p) \sin \omega t \cos 2\omega_m t$$
$$+ 2J_3(\beta_p) \cos \omega t \sin 3\omega_m t + \ldots]. \quad (2\text{-}16)$$

But

$$\sin \omega_m t \cos \omega t = 1/2[\sin(\omega_m t - \omega t) + \sin(\omega_m t + \omega t)]$$
$$= 1/2[\sin(\omega + \omega_m)t - \sin(\omega - \omega_m)t] \quad (2\text{-}17)$$

therefore

$$V_{rec} = \rho V_o[J_o(\beta_p)\sin \omega t + J_1(\beta_p)[\sin(\omega+\omega_m)t - \sin(\omega-\omega_m)t]$$
$$+ J_2(\beta_p)[\sin(\omega+2\omega_m)t + \sin(\omega-2\omega_m)t]$$
$$+ J_3(\beta_p)[\sin(\omega+3\omega_m)t - \sin(\omega-3\omega_m)t]$$
$$+ \ldots]] \quad (2\text{-}18)$$

where

$$\beta_p = 2\omega x_o/c = 4\pi x_o/\lambda. \quad (2\text{-}19)$$

A series expansion of the first order Bessel functions of integral order is [Ramo et al, 1965, p. 208]:

$$J_n(\beta_p) = \sum_{m=o}^{\infty} \frac{(-1)^m(\beta_p/2)^{n+2m}}{m!(n+m)!}. \quad (2\text{-}20)$$

Writing the first few terms of the expansion

$$J_n(\beta_p) = \frac{\beta_p^n}{2^n n!}\left[1 - \frac{\beta_p^2}{2(2n+2)} + \frac{\beta_p^4}{2\cdot4(2n+2)(2n+4)}\right.$$
$$\left. - \frac{\beta_p^6}{2\cdot4\cdot6(2n+2)(2n+4)(2n+6)} + \ldots\right]. \quad (2\text{-}21)$$

For small β_p

$$J_2, J_3 \ldots J_n \ll J_0 \text{ and } J_1 \tag{2-22a}$$

$$J_0(\beta_p) \simeq 1 \tag{2-22b}$$

and $$J_1(\beta_p) \simeq \beta_p/2. \tag{2-22c}$$

Therefore

$$V_{rec} \simeq \rho V_o[\sin \omega t + \frac{\beta_p}{2}[\sin(\omega+\omega_m)t - \sin(\omega-\omega_m)t]]. \tag{2-23}$$

Figure 2-2 is the one-sided line spectra of the received signal. The information we are after is the vibration amplitude, x_o, which is contained in the phase modulation index β_p. In Eq. 2-19, λ is fixed for a constant carrier frequency; therefore a determination of β_p is equivalent to finding x_o. The ratio of one sideband to the carrier in Fig. 2-2 is

$$\frac{\rho V_o \beta_p/2}{\rho V_o} = \beta_p/2. \tag{2-24}$$

Substituting for the expression for β_p from Eq. 2-19 we get

$$\beta_p/2 = \frac{4\pi x_o}{2\lambda} = \frac{2\pi x_o}{\lambda}. \tag{2-25}$$

Expressing this ratio in dB

$$\beta_p/2|_{db} = 20 \log_{10} \frac{2\pi x_o}{\lambda}. \tag{2-26}$$

Therefore the sideband to carrier ratio depends only on the vibration amplitude for a fixed carrier frequency. This observation will be exploited in the calibration of the receiver system.

Chapter III

RECEIVER DESIGN

3.1 Receiving Systems

Let us consider the kinds of receiver that could be used to detect the phase-modulated waveform of the scattered signal. Desirable properties of the receiver are:

1. High sensitivity
2. Calibrated output in terms of vibration amplitude
3. Simplicity consistent with good performance
4. Low cost

Three receivers will be considered: the Doppler transceiver, the homodyne receiver and the sideband heterodyne receiver. Each receiver satisfies at least some of these goals.

3.1.1 Doppler Transceiver

One possible receiver is a doppler transceiver module such as the Microwave Associates Model MA-86502. This module consists of a Gunn oscillator, a circulator and a mixer. A block diagram is shown in Figure 3-1. The Gunn oscillator operates at 10.525 GHz. The transceiver operates as a homodyne receiver in that a portion of the oscillator signal is mixed with the received signal to shift the received signal down to baseband. The matching screw causes a portion of the incident power to be reflected. It is adjusted

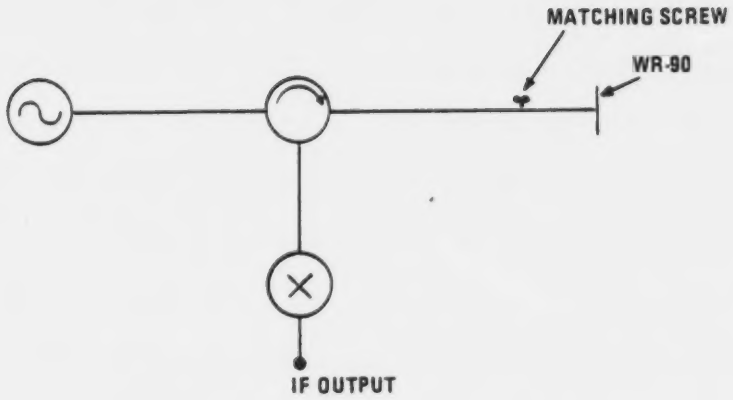

Figure 3-1. Diagram of the Microwave Associates Model MA-86502 Doppler Transceiver.

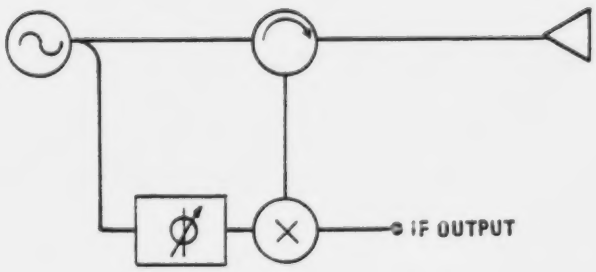

Figure 3-2. Diagram of a Homodyne Receiver with a Manual Phase Shifter.

to set the required bias level on the mixer diode. The ferrite circulator provides isolation between the oscillator and the mixer as well as serving to route the received power to the mixer diode.

This receiver has some limitations for this application. This unit cannot be calibrated to measure an unknown vibration amplitude unless the reflection coefficient of the target is known. It is impossible to measure signal levels within the transceiver because of the integrated assembly. Also the relative phase between the reference and received signals cannot be controlled which is necessary for quadrature phase detection. (The quadrature phase detection method is discussed further in the next section and in section 3.2.1 below.)

The doppler transceiver was designed to detect the doppler frequency shift that results from an approaching or receding target. The doppler-shifted frequency for a target moving with a velocity $v(t) = dx/dt$ can easily be derived from Eq. 2-4. Since ω_i, the instantaneous radian frequency, is

$$\omega_i = d\phi/dt, \tag{3-1}$$

the radian doppler shifted frequency is

$$\omega_i = \omega + 4\pi v(t)/\lambda \ . \tag{3-2}$$

For constant velocity the radian doppler frequency shift ω_d, is

$$\omega_d \equiv 4\pi v_o/\lambda \tag{3-3}$$

and so

$$\omega_i = \omega + \omega_d \tag{3-4}$$

where ω_d is positive for an approaching target and negative for a receding target.

Since the signal returned from a target moving with a uniform velocity has a different frequency than the transmitted signal, the mixer in the transceiver is performing the function of frequency translation. The difference frequency signal at the IF output terminal typically has a frequency of under 4 kHz.

3.1.2 Homodyne Receiver

Another possible receiver for detecting a phase modulated return signal is the homodyne receiver shown in Fig. 3-2. This receiver is similar to the doppler transceiver considered in the previous section in that it too has a zero IF frequency, that is the RF signal is frequency translated directly to baseband without the use of an intermediate frequency. There are several important differences however between the doppler transceiver and the homodyne receiver as configured here. For one, a manual phase shifter has been included to control the relative phase between the reference signal and the received signal. If the phase shifter is adjusted such that the DC output from the mixer or phase detector is zero volts DC, then the two RF signals into the phase detector are in phase quadrature (that is, 90° out of phase) and the method is called "quadrature phase detection". The output of the receiver will then be proportional to the phase modulation.

One of the difficulties with this system is that the reflection coefficient (ρ) directly affects the amplitude of the receiver output signal. This is an undesirable property since the reflection coefficient is not a parameter of interest nor would it be easy to measure if the system were to be used in an open region.

Another difficulty with this system is that the vibration frequency sidebands of the received signal are shifted to the region where they must compete with the flicker noise of the mixer diodes. The origin of flicker noise is not well understood but it is believed to be a surface phenomenon. Flicker noise has an inverse relationship between the noise power and frequency and is exhibited primarily by semiconductors. Although the

doppler transceiver and the homodyne receiver offer the advantage of being simple, the possibility of making quantitative displacement measurements led to consideration of the receiver discussed in the following section.

3.1.3 Sideband Heterodyne Receiver

Basic Operation

A receiver that mitigates the flicker noise problem of the homodyne receiver is the sideband heterodyne receiver. This receiver uses a second oscillator with a frequency at the desired IF frequency to shift the frequency of the first conversion from RF to an IF frequency instead of directly to baseband as in the homodyne receiver. The effects of diode flicker noise are known to limit mixer sensitivity up to about 200 kHz. Therefore choosing an IF frequency above 200 kHz will improve the overall receiver noise figure.

A block diagram of the receiver used for all work to be described herein is shown in Fig. 3-3. The receiver components are interconnected partly with coaxial cable and partly with waveguide. A 10.525 GHz, phase-locked source (OSC 1) supplies RF power for the vibration measurement. Power is routed through a waveguide circulator and to a waveguide switch. In one switch position, RF power is routed to a calibration cell containing a piezoelectric crystal. Some power is reflected from the crystal back to the receiver while the remaining power is absorbed in a waveguide termination. The piezoelectric crystal is driven by an audio frequency signal generator (OSC 3). The vibration amplitude of the crystal is known, and hence as described in chapter II, a phase modulated signal with known sideband to carrier power ratio is reflected back to the receiver. This waveguide leg therefore serves as a convenient calibration path. In the second switch

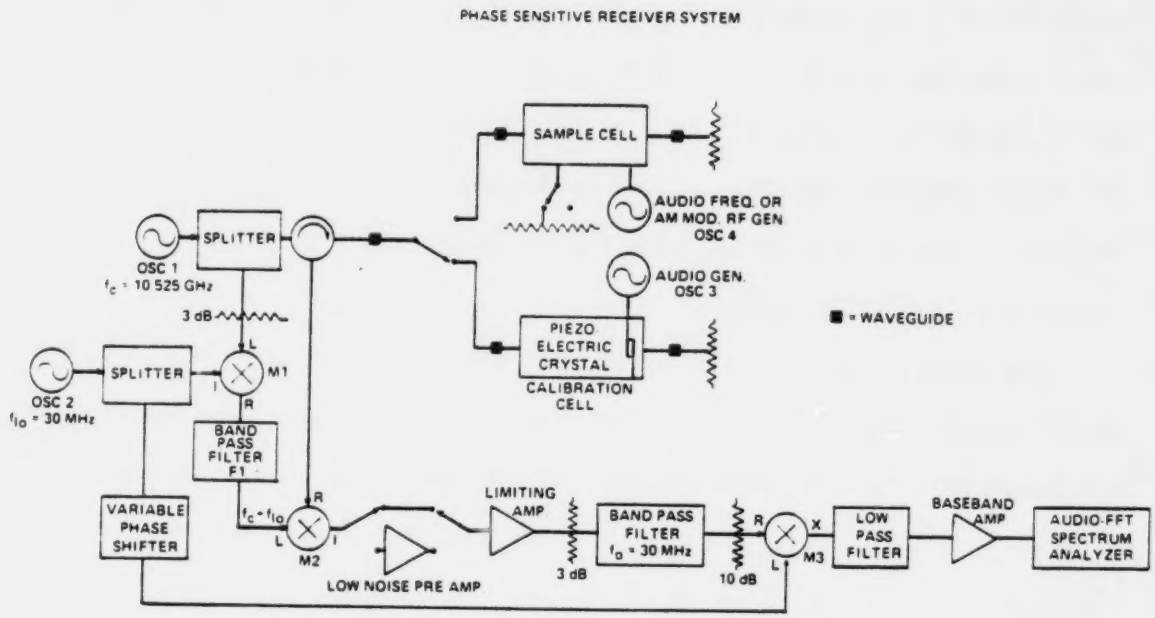

Figure 3-3. Block Diagram of the Sideband Heterodyne Receiver Used for All Experimental Work.

position, RF power is routed toward the sample cell which is described further in Chapter IV. The sample cell permits the simultaneous exposure of a sample to ELF or amplitude-modulated RF signals and vibration monitoring of the resultant vibration. The signal reflected from either the sample in the sample cell or the piezoelectric crystal is directed to mixer M 2. The local oscillator (LO) signal for M 2 is derived from mixing signals from OSC 1 and OSC 2 in the mixer M 1. The IF output of mixer M 1 contains both the sum (10.555 GHz) and the difference (10.495 GHz) frequencies of oscillators OSC 1 and OSC 2. Bandpass filter F 1 (Microwave Filter Co., Inc., Syracuse, NY, Model 3740C-10.5625 SMA) is needed therefore to select one of the mixer products. Fig. 3-4 shows the response characteristics of filter F 1 as it passes the 10.555 GHz signal.

The output signal from mixer M 2 is at 30 MHz since that is the difference frequency between the RF and LO signals to mixer M 2. The sum frequency component will be very small because this 21 GHz signal is well above the operating frequency of mixer M 2. It can also be ignored because it will be rejected by the IF amplifier which is tuned to 30 MHz. It is important to note here that this receiver will not be sensitive to long-term drift of the RF oscillator OSC 1 because the frequency of the IF signal from mixer M 2 will always be at the IF oscillator frequency, OSC 2. Since the bandwidth of the IF amplifiers is 10 MHz and since the information bandwidth is only approximately 400 Hz, there are no long-term drift problems in this receiver for this application.

The low-noise pre-amplifier (Trontech, Inc., Neptune, N.J., Model L30A) has a 1.2 dB noise figure while the limiting amplifier (RHG Electronics Lab Inc., Deer Park, N.Y., Model ICSL 3010) has a 10 dB noise figure. The

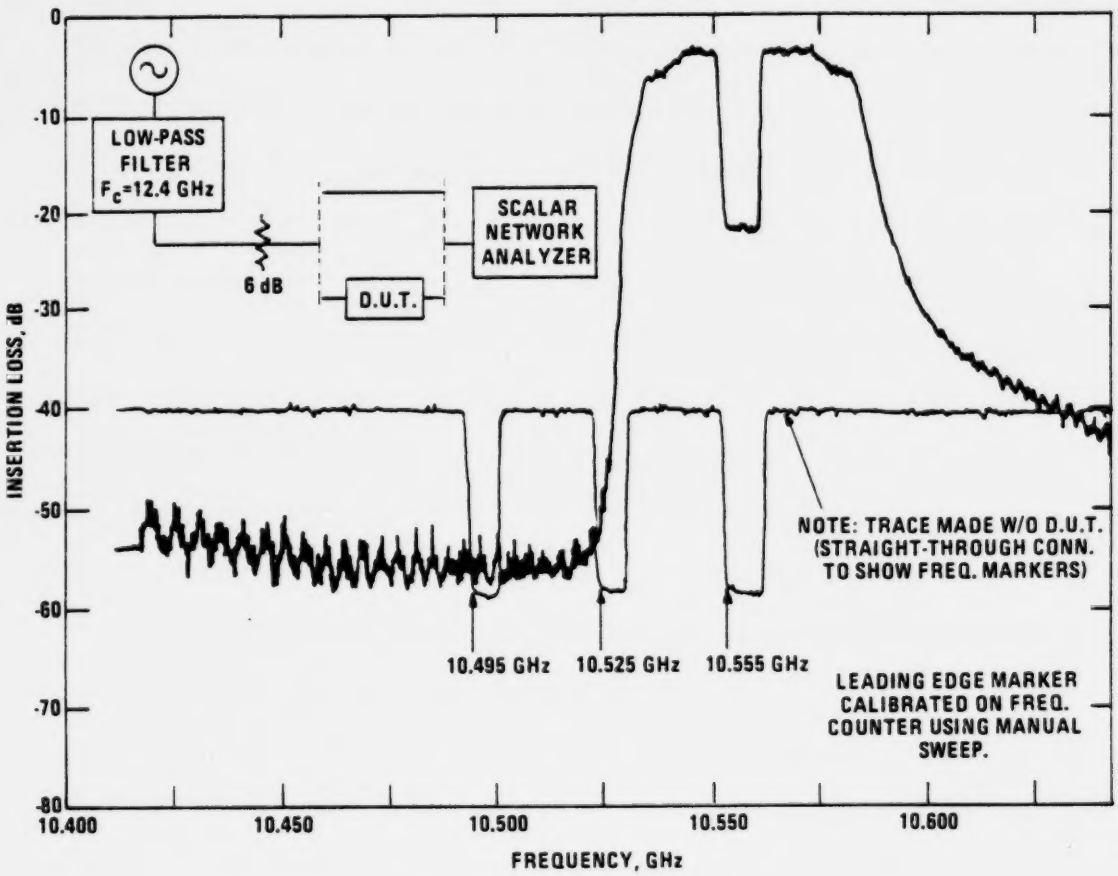

Figure 3-4. Frequency Response of Filter F1 Used to Derive the Receiver Local Oscillator Signal.

pre-amp. is used when the return signal from the sample cell is small enough to permit its use. When it is used (at approximately a -30 dBm mixer output and below) the pre-amp improves the overall receiver noise figure. The limiting amplifier maintains a constant output level over an input range of -70 dBm to -5 dBm. The limiting amplifier serves a very useful purpose. It permits calibration of the system to be maintained over a wide range of return signal levels. In addition the limiting amplifier eliminates AM noise that may be present on the return signal. The limiter output is then attenuated and passed through a 30 MHz bandpass filter and then further attenuated. The attenuation is needed to make the phase detector, M 3, operate linearly. The output of the phase detector, M 3, is then routed to a low-pass filter to remove the RF leakage signals at 30 MHz and its harmonics. After filtering, the signal is amplified with a low-noise variable gain baseband amplifier to raise the signal level to that needed for the low-frequency spectrum analyzer (Hewlett-Packard, Model 3582A).

Low Noise Baseband Amplifier

A special low-noise amplifier was needed to amplify the low-level signal from the phase detector. Since the lowest frequency of interest was set at 1 Hz, an AC-coupled amplifier was chosen. This served to eliminate DC drift considerations from the amplifier. The circuit schematic for the amplifier is shown in Fig. 3-5 while the measured frequency response is plotted in Fig. 3-6. The first two stages use an ultra-low-noise, precision operational amplifier (Precision Monolithics, Inc., Santa Clara, CA, Model OP-27FZ). The first stage has a fixed gain of one hundred and one while the second stage has a fixed gain of fifty-one. A ten-turn potentiometer is used between the first and second stage to control the gain. This method of gain control has the following advantages: the bandwidth of the amplifier

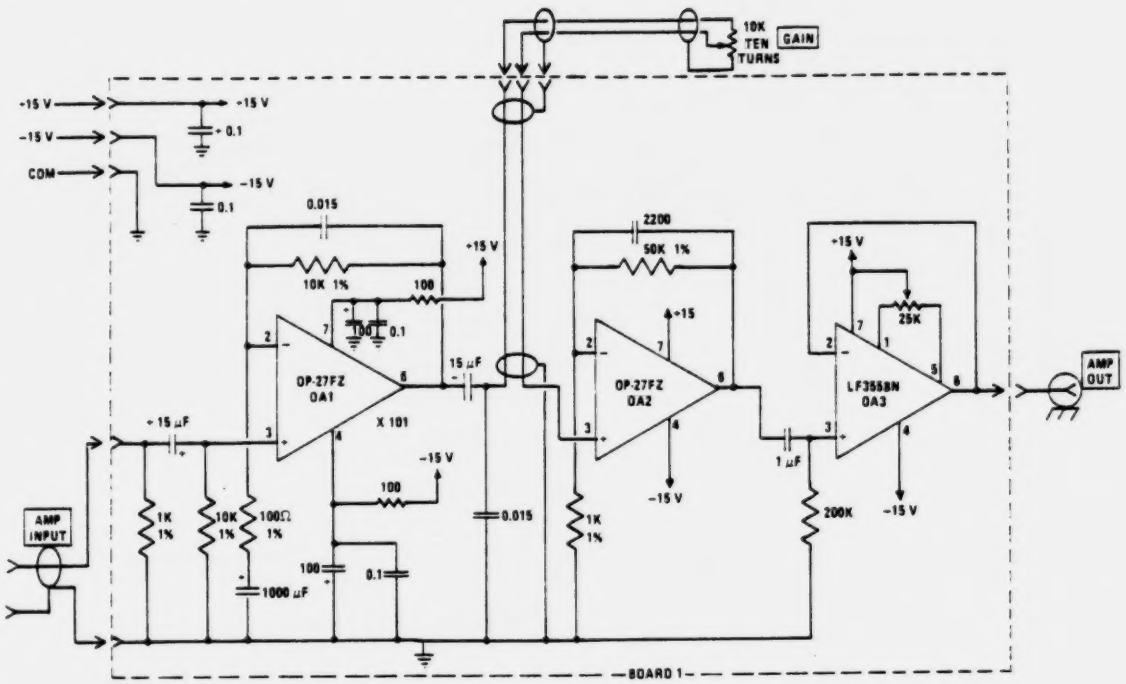

Figure 3-5. Schematic Drawing of the Low Noise Baseband Amplifier.

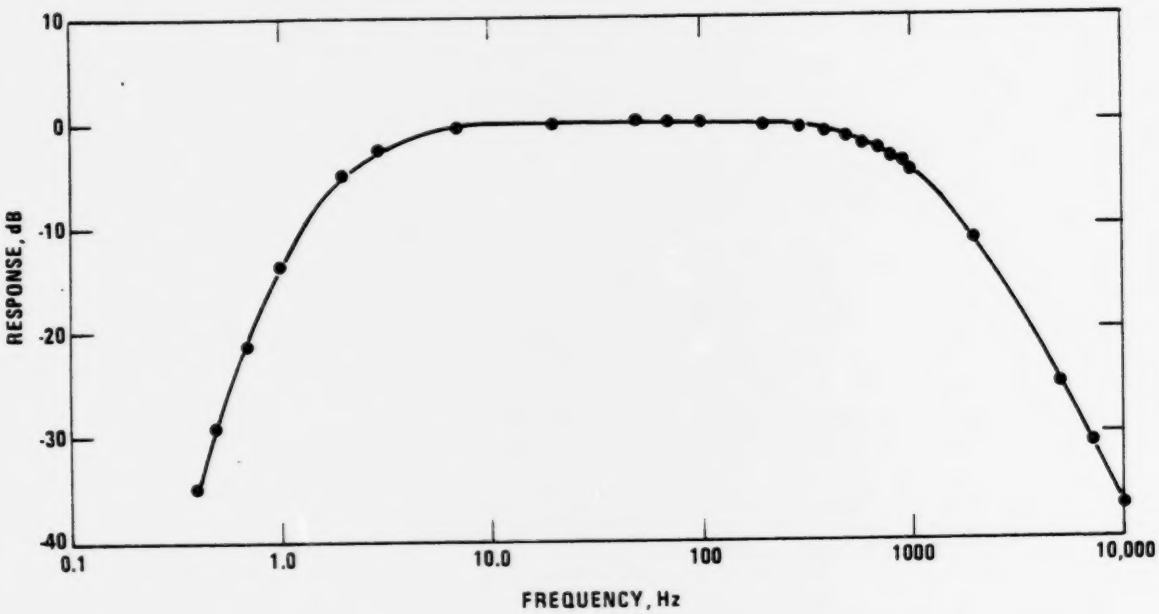

Figure 3-6. Frequency Response of the Low Noise Baseband Amplifer.

is independent of the gain setting; the gain is a linear function of the potentiometer shaft rotation, and the noise of the first stage, and hence the overall amplifier noise referred to the input, is also independent of gain.

The most important design criterion for the amplifier is the noise consideration. Noise is developed from many sources. There is the Johnson noise associated with the source impedances, current and voltage white noise in the amplifier and current and voltage flicker noise also associated with the amplifier. The low-frequency noise in the amplifier used here can be analyzed using the amplifier noise model [Soderquist, 1975] shown in Fig. 3-7 where E_{t1} and E_{t2} are the RMS voltages over a given bandwidth of the thermal or Johnson noise due to the source resistors R_{S1} and R_{S2}, E_N is the RMS voltage due to noise voltage in the amplifier and I_{N1} and I_{N2} are the RMS currents due to noise currents generated in the amplifier. The noise currents I_{N1}, I_{N2} will flow through R_{S1} and R_{S2} respectively, producing a voltage noise. The total input-referred RMS noise voltage over the frequency range of f_L to f_H is then

$$E_{NT}(f_H-f_L) = \sqrt{E_N^2+(I_{N1}R_{S1})^2+(I_{N2}R_{S2})^2+E_{t1}^2+E_{t2}^2} \qquad (3\text{-}5)$$

where all the noise sources are assumed uncorrelated and assumed to have Gaussian amplitude distributions. E_t, the thermal noise of the source resistor is given by

$$E_t = \sqrt{4kTR_S(f_H-f_L)} \qquad (3\text{-}6)$$

where K is Boltzman's constant ($1.38\text{X}10^{-23}$ J/°K) and T is the absolute temperature in Kelvin degrees. At room temperature the factor $\sqrt{4kT}$ is $1.28\text{X}10^{-10}$ therefore

$$E_t = 1.28\text{X}10^{-10}\sqrt{R(f_H-f_L)} \qquad (3\text{-}7)$$

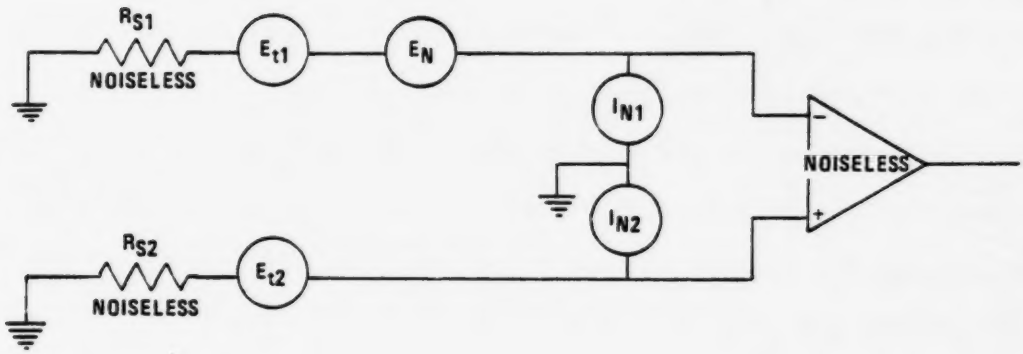

Figure 3-7. Model for Analysis of the Noise Characteristics of the Low Noise Baseband Amplifier.

The term E_N is given by

$$E_N = e_n \sqrt{f_{ce} \ln(f_H/f_L) + (f_H - f_L)} \qquad (3\text{-}8)$$

where e_n is the white noise voltage spectral density and f_{ce} is the voltage noise corner frequency. The first term under the square root sign in Eq. 3-8 is a flicker noise term while the second term is a white noise term. The noise corner frequency is the frequency at which the flicker noise spectral density is equal to the white noise spectral density. The expression for I_N is similar and is given by

$$I_N = i_n \sqrt{f_{ci} \ln(f_H/f_L) + (f_H - f_L)} \qquad (3\text{-}9)$$

where i_n is the white noise current spectral density and f_{ci} is the current noise corner frequency.

The pertinent noise specifications for the OP-27FZ amplifier are given in Table 3-1.

Table 3-1

Noise Specifications for the Precision Monolithics Inc.
Model OP-27FZ Operational Amplifier

Parameter	Symbol	Value (MAX)	Units
Input Noise Voltage Density	e_n @ 10 Hz	5.5	$nV/\sqrt{Hz}$
	e_n @ 1000 Hz	3.8	$nV/\sqrt{Hz}$
Input Noise Current Density	i_n @ 10 Hz	4.0	$pA/\sqrt{Hz}$
	i_n @ 1000 Hz	0.6	$pA/\sqrt{Hz}$
Corner Freq.	f_{ce}	2.7	Hz
Corner Freq.	f_{ci}	140	Hz

Using values in Table 3-1 and Eq. 3-5, the total input-referred RMS noise voltage can calculated. Strictly speaking the noise equivalent bandwidth must be used in the calculation which is the same as the half-power bandwidth only for a perfect ("brick wall") filter. In these calculations nominal cutoff frequencies of 1 Hz and 1000 Hz are used. The thermal noise terms depend on the source resistances. The source resistance for the op-amp. inverting input is 100 Ω (Fig. 3-5) while the source resistance of the non-inverting input is the low-pass filter source impedance, 50 Ω , (Fig. 3-8b). Using Eq. 3-7 the thermal noise voltage terms are

$$E_{t1} = 1.28X10^{-10}\sqrt{50\ \Omega\ (1000-1)}$$
$$= 28.6\ nV_{RMS}$$

$$E_{t2} = 1.28X10^{-10}\sqrt{100\ \Omega\ (1000-1)}$$
$$= 40.5\ nV_{RMS}.$$

Using Eq. 3-8 the E_N term in Eq. 3-5 is

$$E_N = 3.8\frac{nV}{\sqrt{Hz}}\sqrt{2.7Hz\ln(1000/1)+(1000-1)}$$

$$= 121\ nV_{RMS}.$$

Using Eq. 3-9 the remaining terms are

$$I_{N1}R_{S1} = 0.6\frac{pA}{\sqrt{Hz}}\sqrt{140Hz\ \ln(1000/1)+(1000-1)}\cdot 50\ \Omega$$
$$= 1.33\ nV_{RMS}$$

$$I_{N2}R_{S2} = 0.6\frac{pA}{\sqrt{Hz}}\sqrt{140Hz\ \ln(1000/1)+(1000-1)}\cdot 100\ \Omega.$$
$$= 2.66\ nV_{RMS}.$$

Inserting all these values into Eq. 3-5, E_{NT} is

$$E_{NT} = \sqrt{(121)^2+(1.33)^2+(2.66)^2+(28.6)^2+(40.5)^2}\ nV_{RMS}$$

$$E_{NT} = 1.31\ nV_{RMS}.$$

A commonly used approximation for converting the RMS value of a variable with a Gaussian distribution to a peak to peak value is to multiply the RMS value by 6 [Soderquist, 1975]:

$$V_{NOISEpp} \simeq 6\ X\ E_{NT\ RMS} \qquad (3\text{-}10)$$

$$\approx 6 \times 131 \text{ nV}_{RMS}$$

$$= 0.78 \text{ } \mu V_{pp}.$$

Therefore the expected input-referred noise voltage of the baseband amplifier is about 0.8 μV peak to peak for a pass band from 1 Hz to 1000 Hz.

To compare the predicted amplifier performance to measured data, the calculated noise should be expressed differently. The audio spectrum analyzer can display a signal in dBV/$\sqrt{Hz}$. Therefore it is useful to express the amplifier noise in these units at a particular frequency of interest. If 10 Hz is chosen for the calculation then using values from Table 3-1.

$$e_n = 5.5 \text{ nV}/\sqrt{Hz}$$

$$i_n = 4\text{pA}/\sqrt{Hz}$$

$$R_{S1}\ i_n = 50 \times 4 = 200 \text{ pV}/\sqrt{Hz} = 0.2 \text{ nV}/\sqrt{Hz}$$

$$R_{S2}\ i_n = 100 \times 4 = 400 \text{ pV}/\sqrt{Hz} = 0.4 \text{ nV}/\sqrt{Hz}$$

$$e_{t1} = 1.28 \times 10^{-10}\sqrt{R} = 1.28 \times 10^{-10}\sqrt{50} = 0.91 \text{ nV}/\sqrt{Hz}$$

$$e_{t2} = 1.28 \times 10^{-10}\sqrt{100} = 1.28 \text{ nV}/\sqrt{Hz}$$

$$e_{NT} = \sqrt{e_n^2+(i_nR_{S1})^2+(i_nR_{S2})^2+e_{t1}^2+e_{t1}^2+e_{t2}^2}$$

$$= \sqrt{(5.5)^2+(0.2)^2+(0.4)^2+(.91)^2+(1.28)^2} \text{ nV}/\sqrt{Hz}$$

$$e_{NT}\Big|_{10Hz} = 5.7 \text{ nV}/\sqrt{Hz} \text{ MAX.}$$

This value expressed in dBV/$\sqrt{Hz}$ is

$$e_{NT}\Big|_{dBV} = 20 \log(5.7\times10^{-9}\text{V}/1\text{V}) = -165 \text{ dBV}/\sqrt{Hz}$$

To compare this to the measured amplifier noise the amplifier gain must be added because the noise is observed with the spectrum analyzer at the amplifier output. The amplifier gain is 2,575, which is +68 dB. Therefore the calculated noise at the amplifier output at 10 Hz is

$$-165 \text{ dBV}/\sqrt{Hz} + 68\text{dB} = -97 \text{ dBV}/\sqrt{Hz} \text{ (MAX)}$$

The measured value on the spectrum analyzer at 10 Hz was -100 dBV/$\sqrt{Hz}$. Noise considerations to follow of other system components will demonstrate

that this level of the noise is sufficiently low that this amplifier does not limit overall receiver sensitivity. Therefore the amplifier design is adequate for the receiver.

Low Pass Filter Design

A three-pole, low pass pi-filter was designed using modern filter design theory to suppress the RF signals at multiples of 30 MHz that leak through the phase detector, M 3. For the third order Butterworth filter the prototype circuit (Fig. 3-8a) has element values $C_1 = 1.000$, $L_2 = 2.000$, and $C_3 = 1.000$. A cutoff frequency of 1.59 MHz was selected to allow the use of a standard value of inductance while providing desired performance. To transform the prototype values to the actual values for the desired frequency range and impedance levels, Eq. (3-11a) and (3-11b) were used with R equal to 50 ohms

$$C_n' = C_n/2\pi f_c R \qquad (3\text{-}11a)$$

$$L_n' = RL_n/2\pi f_c. \qquad (3\text{-}11b)$$

The final circuit (Fig. 3-8b) was constructed with a shield as shown which improved the high frequency insertion loss by reducing stray coupling from the input circuit to the output. From universal Butterworth filter response curves for a three-pole filter, the attenuation should be 60 dB per decade. At 30 MHz the attenuation should be greater than 60 dB. The filter response (Fig. 3-9) deteriorates somewhat above about 25 MHz. This is due in part to the lumped-element construction technique resulting in some series inductance in the capacitor leads as well as the winding capacitance of the inductor.

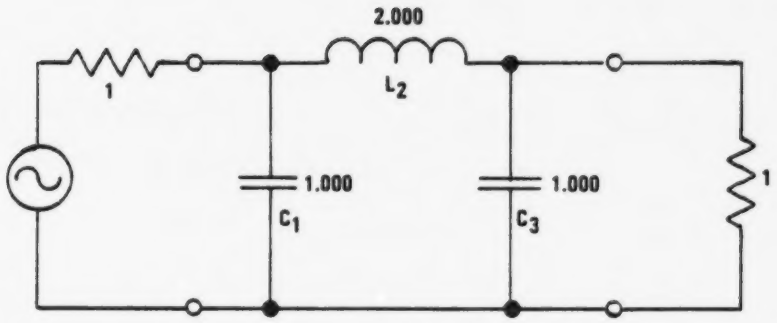

Figure 3-8a. Low Pass Prototype Butterworth Filter.

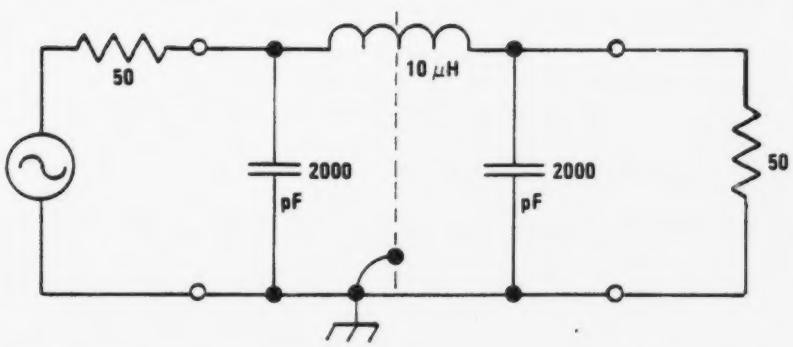

Figure 3-8b. Low Pass Butterworth Filter.

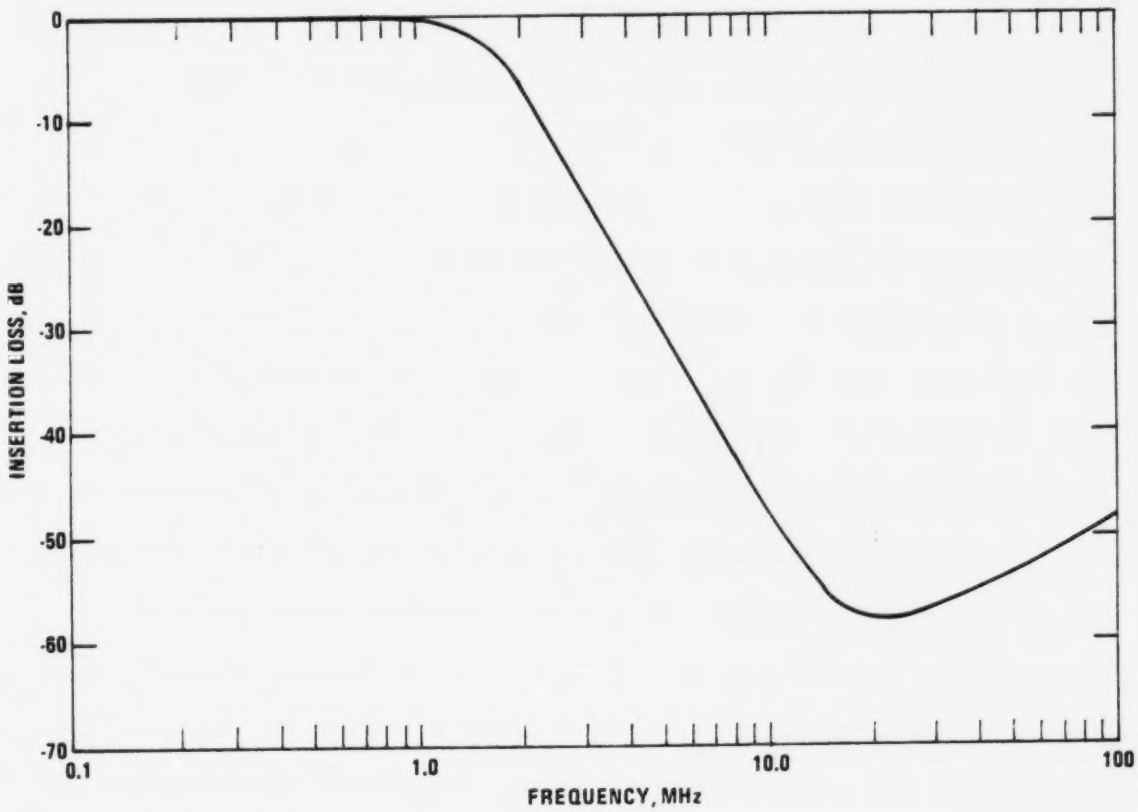

Figure 3-9. Frequency Response of the Low Pass Butterworth Filter.

3.2 Sensitivity of the Sideband Heterodyne Receiver

3.2.1 Phase Noise

Short-term frequency stability has been described as residual FM noise, single-sideband (SSB) phase noise or phase jitter. The latter term is normally used to describe short-term frequency stability when it is observed in the time domain. Short-term frequency instability is a random noise phenomenon that broadens the spectrum of an oscillator by modulating the frequency (or phase) of an ideal oscillator. The frequency spectrum of an oscillator exhibiting phase noise would appear as shown in Fig. 3-10. The short-term frequency stability of a transmitter oscillator in a doppler radar can be the limiting factor in the overall receiver sensitivity. In this application the received signal may be shifted only a few kilohertz from the transmitter frequency, and the clutter from stationary scatterers may be large compared to the target echo. The phase noise can limit the sensitivity of the receiver in this case. Fig. 3-11 shows the spectral line at f_R buried in the phase noise of the transmitter oscillator.

Although the phase noise has a continuous spectral density, the noise can be thought of as being generated by the summation of an infinite number of sine wave oscillators each modulating the carrier frequency by a different amount. From Fig. 3-10 it is evident that as the modulating frequency increases, the amplitude of the modulation source decreases rapidly. Since single-sideband phase noise and FM noise are both commonly used [Payne, 1982], it is important to understand the relationship between these two equivalent forms of expression for the short-term frequency stability.

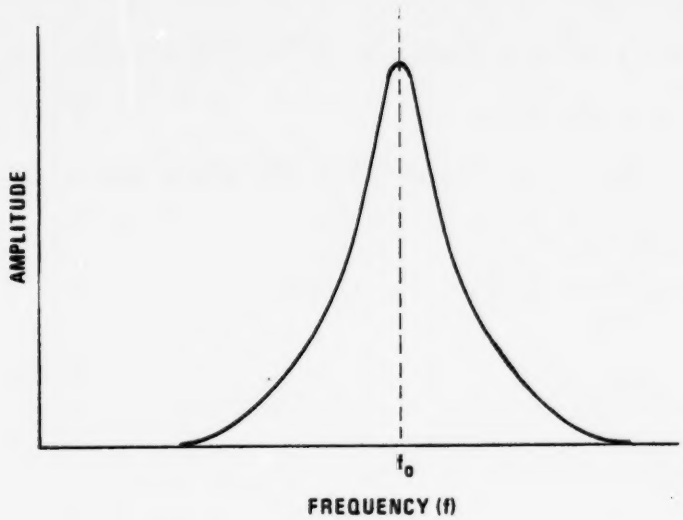

Figure 3-10. Typical Phase Noise Spectrum of an Oscillator.

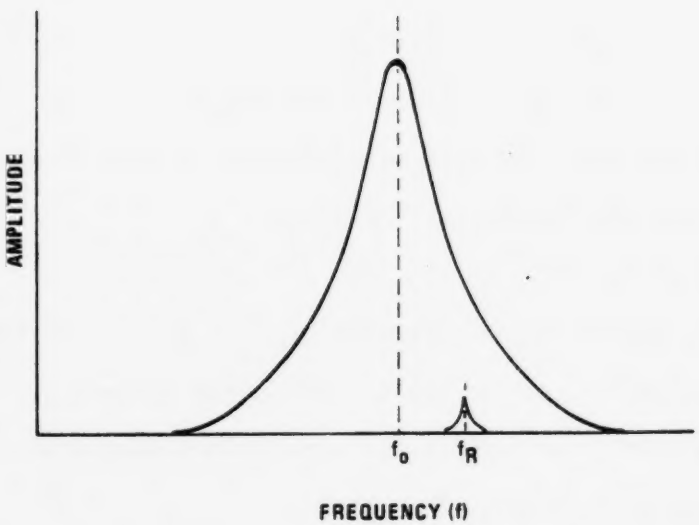

Figure 3-11. The Received Signal from a Doppler Radar Swamped by Oscillator Phase Noise.

Let the voltage from a sinusoidal oscillator be

$$V(t) = E \sin (2\pi f_c t + \theta(t)) \tag{3-12}$$

where $\theta(t)$ represents the random noise component. Using the model described above of the noise being a summation of individual sinusoidal oscillators,

$$\theta(t) = \Delta\phi \sin 2\pi f_m t \tag{3-13}$$

where $\Delta\phi$ is the peak phase deviation or the phase deviation constant. Then for phase modulation

$$V(t) = E \sin (2\pi f_c t + \Delta\phi \sin 2\pi f_m t) \tag{3-14}$$

and for FM

$$\omega_i = d\theta(t)/dt = 2\pi f_c + \Delta\phi 2\pi f_m \cos 2\pi f_m t \tag{3-15}$$

$$f_i = f_c + \Delta\phi f_m \cos 2\pi f_m t. \tag{3-16}$$

Let

$$\Delta\phi f_m = \Delta f \tag{3-17}$$

where Δf is the frequency deviation constant or the peak frequency deviation. $\Delta\phi$ can therefore be expressed as

$$\Delta\phi = \Delta f/f_m. \tag{3-18}$$

Substituting this into Eq. 3-14 we get

$$V(t) = E \sin (2\pi f_c t + \Delta f/f_m \sin 2\pi f_m t). \tag{3-19}$$

The ratio of the peak frequency deviation to the modulation frequency is called the frequency modulation index, m,

$$m \equiv \Delta f/f_m. \tag{3-20}$$

The frequency spectrum of a phase-modulated sine wave for small modulation index was derived above. Noting the similarity between Eq. 2-10 and Eqs. 3-14 and 3-19, the formula for the single-sideband to carrier ratio (Eq. 2-24) can be used here to obtain

$$E_{SB}/E_C = m/2 = \Delta f/2f_m = \frac{\Delta\phi}{2}. \tag{3-21}$$

Expressing this relationship in dB we get

$$E_{SB}/E_C\Big|_{dB} = 20 \log(\Delta f/2f_m)\ dB = 20 \log\ (\Delta\phi/2). \qquad (3\text{-}22)$$

When this quantity is expressed on a per hertz of bandwidth basis, then it is referred to as L(f) [Shoaf et al, 1973]. For random fluctuations the frequency deviation constant, Δf, is replaced by the RMS frequency deviation:

$$\Delta f_{RMS} = \Delta f/\sqrt{2}. \qquad (3\text{-}23)$$

Substituting Eq. 3-23 into Eq. 3-22 and assuming a 1 Hz bandwidth we get

$$L(f) = E_{SB}/E_C\Big|_{dB} = 20 \log(\Delta f_{RMS}\sqrt{2}/2f_m) \qquad (3\text{-}24)$$

$$L(f) = 20 \log\ (\Delta f_{RMS}/\sqrt{2}\ f_m). \qquad (3\text{-}25)$$

Eq. 3-25 is therefore the expression that relates the single sideband phase noise to the RMS frequency deviation. For example, if the SSB phase noise was -60 dBc in a 1 Hz bandwidth 1,000 Hz from the carrier, then this noise is equivalent to

$$-60 = 20 \log\ \left(\frac{\Delta f_{RMS}}{1000\sqrt{2}}\right)$$

$$\Delta f_{RMS} = 1.414 \text{ Hz}$$

also in 1 Hz bandwidth.

Therefore, a -60 dBc SSB phase noise at 1000 Hz from the carrier is equivalent to 1.414 Hz RMS frequency deviation at 1000 Hz from the carrier if both are measured with the same bandwidth. To convert the SSB phase noise from one measuring bandwidth, B_1, to another, B_2, the formula

$$P_2/P_1\Big|_{dB} = 10 \log\ (B_2/B_1) \qquad (3\text{-}26)$$

is used [Manassewitsch, 1980] where P_i is the noise power measured with bandwidth B_i.

Detection of Phase Noise

For moderate phase noise, L(f) can be measured directly on a spectrum

analyzer if the AM noise is known to be small in comparison to the phase noise. A combined AM and phase modulation (PM) noise spectrum is indicated if there is an asymmetry in the spectrum about the carrier. For low phase noise (such as from high quality phase-locked sources) the quadrature phase detection method [Shoaf et al, 1973; Hewlett-Packard Co., 1981; Manassewitsch, 1980; Payne, 1982] has high sensitivity and in addition provides rejection of AM noise. A block diagram of this method is shown in Fig. 3-12. Typically the source to be measured, S_1, and a stable source, S_2, are fed into the RF and LO ports of a double-balanced mixer. The two sources must be at the same frequency and 90° out of phase. Quite often a DC-coupled feedback signal to the reference oscillator is used to phase-lock the two sources and maintain the phase quadrature. The bandwidth of the feedback signal must be below the lowest frequency of interest in the phase noise output. If the bandwidth is too large, the feedback control system will cancel the noise.

Operation of the method can be derived as follows by examining the product term of the mixer:

$$y(t) = AB \cos(\omega_c t + \phi(t)) \sin \omega_c t$$

$$= AB \sin \omega_c t[\cos \omega_c t \cos \phi(t) - \sin \omega_c t \sin \phi(t)]. \quad (3\text{-}27)$$

Expanding further and using trig. identities

$$y(t) = -\frac{AB}{2} \sin \phi(t) + \frac{AB}{2} \sin(2\omega_c t + \phi(t)). \quad (3\text{-}28)$$

Passing this signal through the low pass filter leaves

$$v(t) = -\frac{AB}{2} \sin \phi(t) = -k_\phi \sin \phi(t). \quad (3\text{-}29)$$

The phase noise, $\phi(t)$, is very small therefore

$$v(t) \approx k_\phi \phi(t) \quad (3\text{-}30)$$

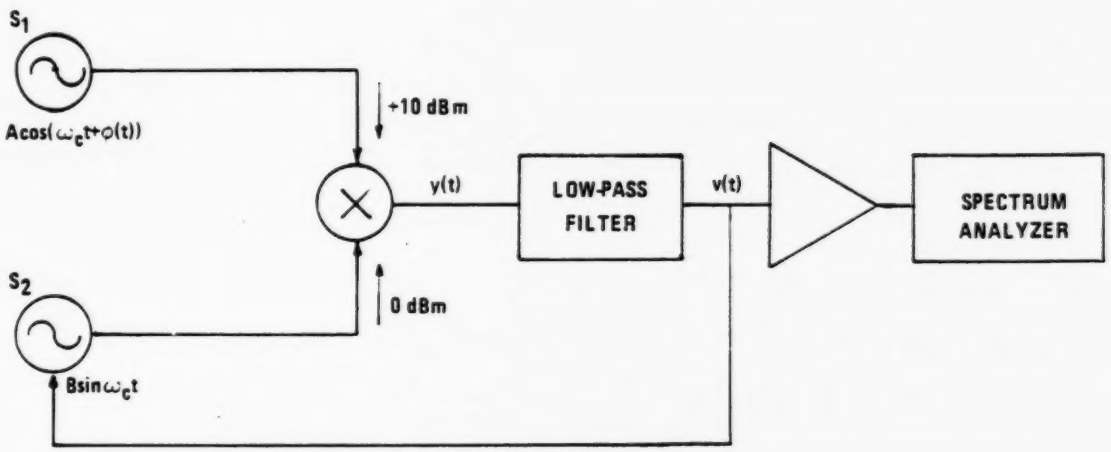

Figure 3-12. Block Diagram of Quadrature Phase Detection Method for the Measurement of Phase Noise.

where k_ϕ is the phase detector constant.

When the noise model described above, which represents the noise as a summation of sinusoids, is used, then

$$\phi(t) = \Delta\phi \sin \omega_m t \tag{3-31}$$

and

$$v_m(t) = k_\phi \Delta\phi \sin \omega_m t. \tag{3-32}$$

The RMS voltage of this signal is

$$V_{RMS} = (k_\phi \Delta\phi)/\sqrt{2}. \tag{3-33}$$

Solving for $\Delta\phi$ we get

$$\Delta\phi = \sqrt{2}\ V_{RMS}/k_\phi. \tag{3-34}$$

From Eq. 3-22, the equation for the SSB phase noise in a one Hertz bandwidth is

$$L(f) = [\Delta\phi/2]^2. \tag{3-35}$$

Substituting Eq. 3-34 into Eq. 3-35 we get

$$L(f) = 2[V_{RMS}/2k_\phi]^2. \tag{3-36}$$

This equation is used whenever the oscillator under test is much noiser than the reference. It is also used in the measurement of residual phase noise (RPN) as will be discussed below.

If two equally noisy sources are used, L(f), the SSB phase noise, is calculated as follows

$$L(f) = [V_{RMS}/2k_\phi]^2 \tag{3-37}$$

which is half the value in Eq. 3-36 with the obvious designation of half the noise power to each source.

Residual phase noise (RPN) is a term normally applied to a frequency synthesizer to characterize its phase noise exclusive of the noise of the reference oscillator. (A frequency synthesizer is an instrument that generates many frequencies from one or a few reference sources.) Absolute

phase noise on the other hand includes the noise of the reference oscillator in the device output. It is clear then that for oscillators only absolute phase noise is meaningful whereas for amplifiers one could consider either residual or absolute phase noise. Residual phase noise of frequency synthesizers is measured with a system configured as shown in Fig. 3-13. In Fig. 3-13 two identical devices (synthesizers) are driven from a common reference. If the phase shifts through the devices are equal, the phase noise of the reference cancels at the mixer (phase detector) and the measured noise is the sum of the residual phase noise of the devices under test (DUT). If devices such as limiters, amplifiers, filters, etc. are to be tested, only one such device is used and the test setup is then referred to as a differential phase noise measurement system [Shoaf et al, 1973] but the measured noise is still referred to as residual phase noise. It is assumed in both cases that the signals arriving at the phase detector are in phase quadrature.

Residual Phase Noise of the RF Amplifier

Mixer M 2 in the block diagram (Fig. 3-3) is a microwave mixer with a specified optimum LO power of 10 mW. In the initial design of this receiver an RF amplifier (Miteq Inc., Hauppauge, N.Y. Model AMF-3B-8012-4) was included between mixer M 2 and filter F 1 to raise the level of the LO signal to that required by mixer M 2. The following experiment demonstrates clearly how the residual phase noise of a device can limit the sensitivity of a receiver, particularly one that must receive a signal having small information (modulation) sidebands relative to the carrier. The experimental setup for the quadrature phase detection is shown (Fig. 3-14).

First the system sensitivity is recorded (Fig. 3-15) by connecting the system without the DUT and setting attenuator P_1 equal to 0.0 dB. The

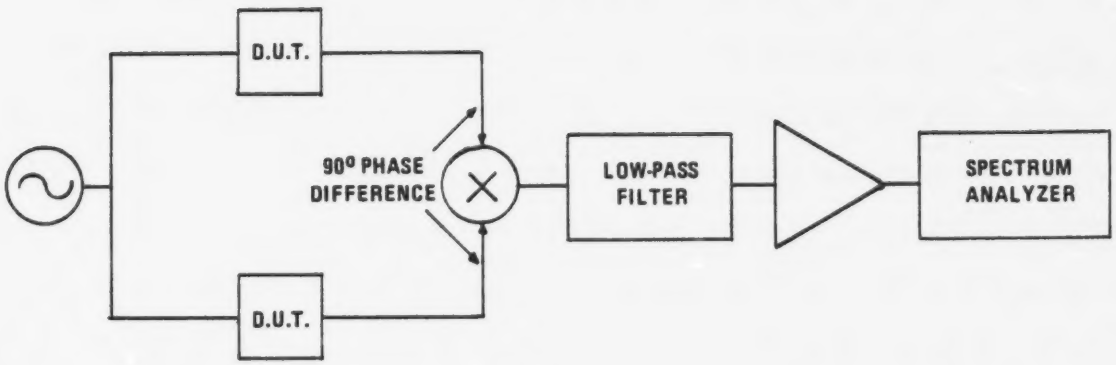

Figure 3-13. General Residual Phase Noise Measurement Circuit.

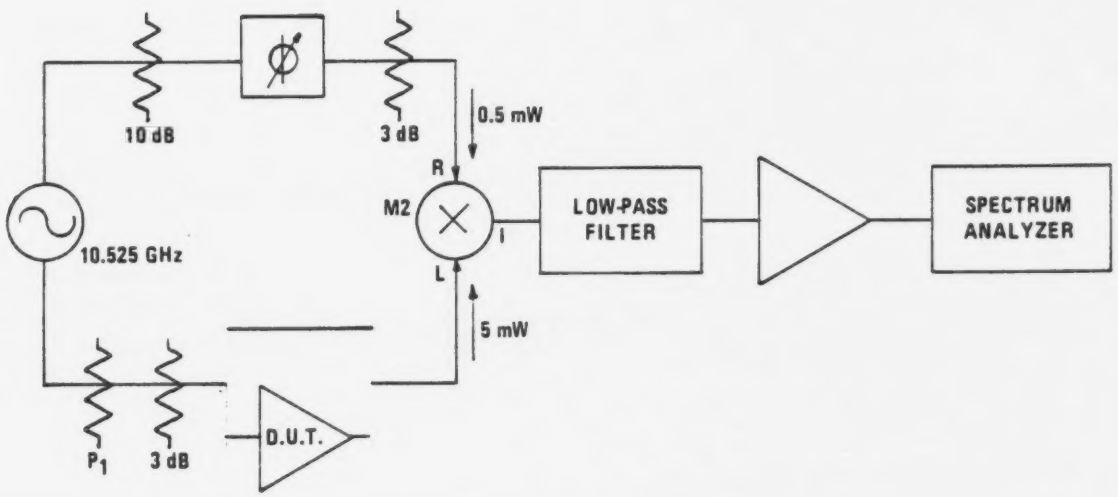

Figure 3-14. Experimental Setup for Residual Phase Noise Measurements.

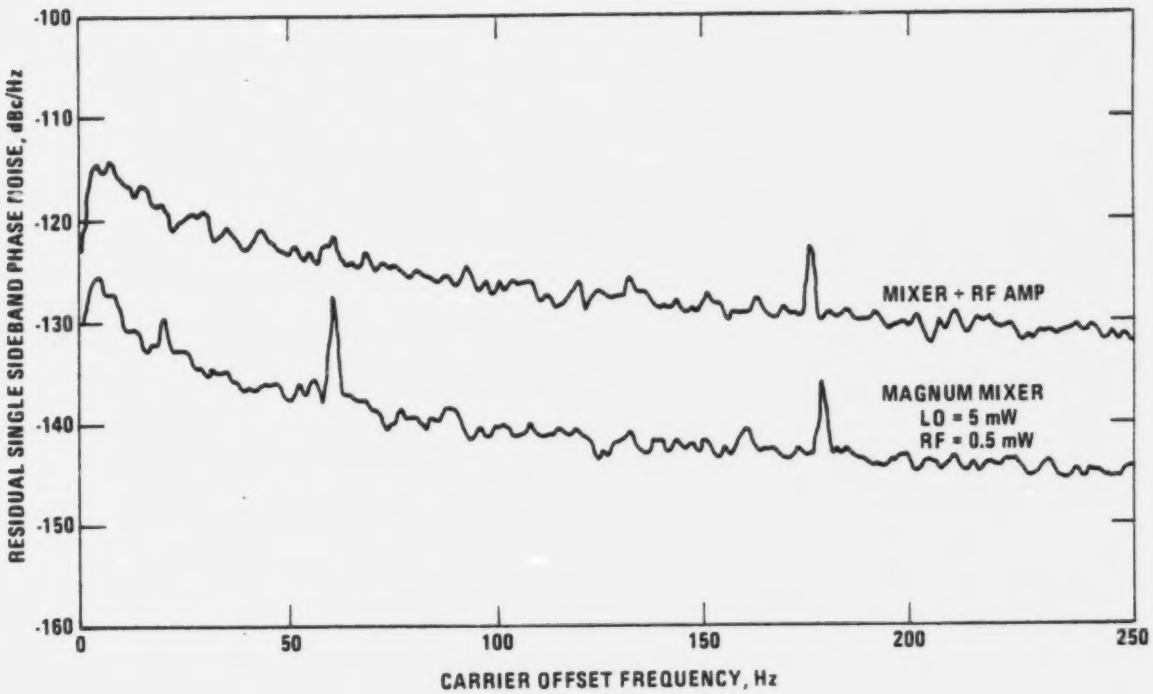

Figure 3-15. Residual Phase Noise of the Magnum Microwave Model M0 64P Mixer and the Miteq Model AMF-3R-8012-4 Low Noise RF Amplifier

phase detector constant k_ϕ is measured next by adjusting the manual phase shifter until a maximum DC voltage is produced at the phase detector I port. Repeating Eq. 3-36 derived earlier for convenience

$$L(f) = 2[V_{RMS}/2k_\phi]^2.$$

Converting this to dB

$$L(f)\Big|_{dBc/\sqrt{Hz}} = 10 \log 2 + 20 \log V_{RMS} - 20 \log (2k_\phi). \qquad (3\text{-}38)$$

The second term is the phase detector output in $dBV/\sqrt{Hz}$. The analyzer reading is the phase detector output increased by the gain of the amplifier, 68 dB. Therefore expressing L(f) in terms of the analyzer reading, V_{anal}

$$L(f)\Big|_{dBc/\sqrt{Hz}} = +\ 3dB + V_{anal}\Big|_{dBV/\sqrt{Hz}} - 68\ dB - 20 \log (2k_\phi). \qquad (3\text{-}39)$$

This equation is used repeatedly as the basis for all vertical axis calibrations in the measurements to follow.

The phase shifter is now adjusted for quadrature detection at the phase detector by monitoring the DC output voltage of the detector and adjusting the phase shifter until 0.0 volts is obtained. The lower trace (Fig. 3-15) shows the residual phase noise of the mixer M 2 (Magnum Microwave Corp., Sunnyvale, CA. Model M064P) out to a sideband frequency of 250 Hz. With this mixer used as the phase detector, this noise represents the best sensitivity obtainable.

To measure the phase noise of the RF amp, the DUT is connected and P_1 is set equal to 20 dB to maintain the same power level to the L port of the phase detector. The upper trace of Fig. 3-15 shows the SSB phase noise for the mixer (phase detector) plus the RF amplifier. Since in the top trace the SSB phase noise is more than 10 dB greater than in the lower trace, the top trace is essentially the phase noise of the RF amplifier. The relationship between two power levels and their sum is shown in Fig. 3-16. The

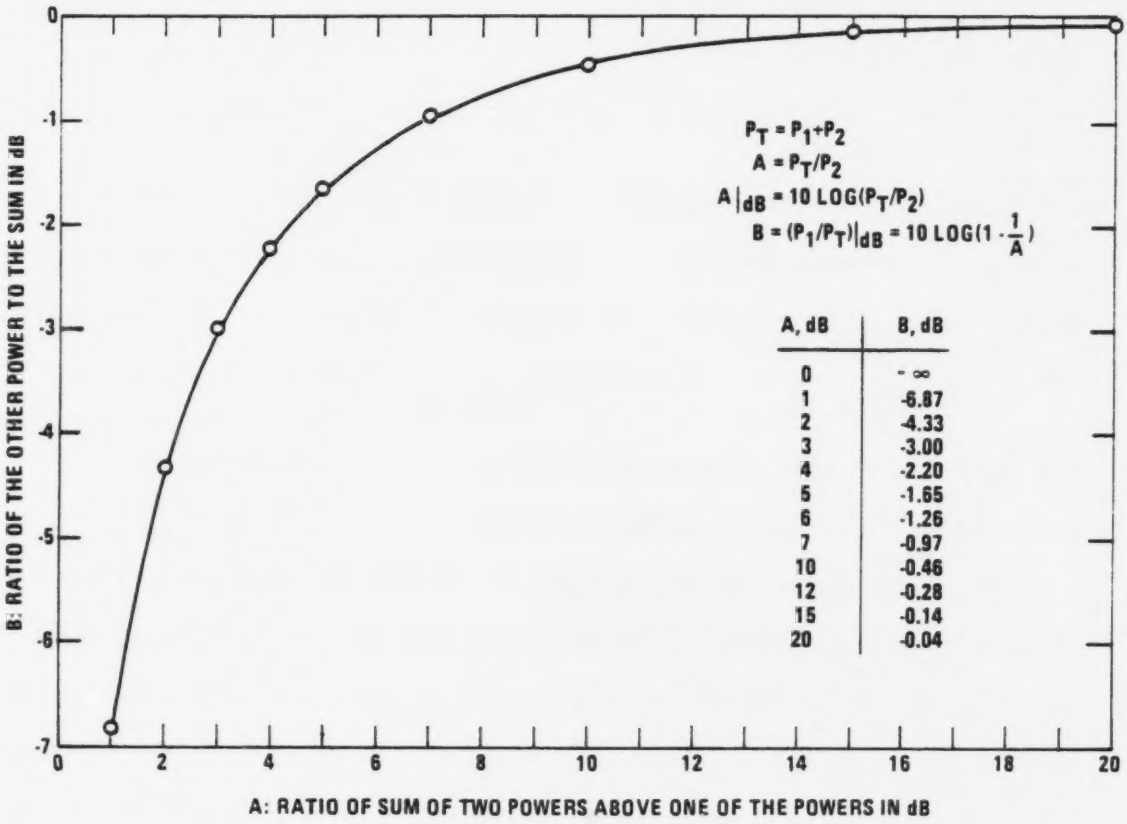

A, dB	B, dB
0	- ∞
1	-6.87
2	-4.33
3	-3.00
4	-2.20
5	-1.65
6	-1.26
7	-0.97
10	-0.46
12	-0.28
15	-0.14
20	-0.04

Figure 3-16. Relationship Between Two Power Levels and Their Sum (in dB).

difference (in dB) between the top trace and the bottom trace is the value to be read on the abscissa of Fig. 3-16 since the top trace represents the sum of two powers and the bottom trace is one of those powers. Fig. 3-16 reveals how much to reduce the top trace values to obtain the level of the second power (the RF amp. noise in this case). For example since the difference between the traces is about 14 dB, the RF amplifier phase noise is about 0.2 dB lower than the noise represented by the top trace.

The RF amplifier has degraded the sensitivity by 14 dB when compared to the microwave mixer noise. This level of residual phase noise was deemed excessive and therefore the RF amplifier was not used in the final receiver design.

Residual Phase Noise of the Limiting Amplifier

The same measurement procedure was used to measure the residual phase noise of the limiting amplifier in the IF leg of the receiver. The measurement circuit (Fig. 3-17a) used the IF oscillator (OSC 2) as the source and the mixer (M 3) as the phase detector. The circuit in Fig. 3-17b was used for the limiting amplifier. The phase detector constant was 220 mV/radian in each case. Fig. 3-18 shows the residual phase noise of the phase detector and of the limiting amplifier as a function of RF drive level to the limiting amp. The bottom curve is the noise level of the baseband amplifier discussed in Section 3.1.3. The curve labeled "mixer" represents the sensitivity of the phase noise measurement circuit. The four curves above the "mixer" curve are the residual phase noise with the labeled RF drive levels applied to the limiting amplifier. The figure shows that the best performance is obtained from the limiting amplifier with the maximum RF drive level, -5 dBm. Figure 3-18 also shows the predominance of flicker noise at low offset

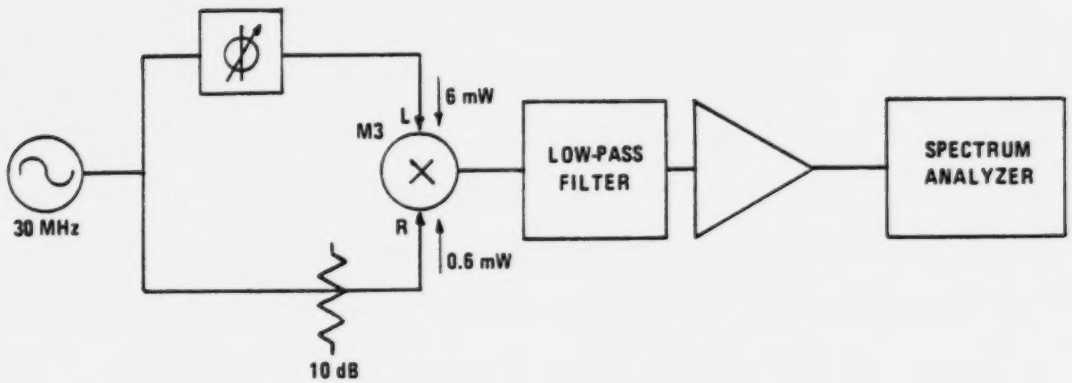

Figure 3-17a. Circuit for Measurement of Basic System Sensitivity for Residual Phase Noise Measurements for Devices Which Operate at 30 MHz.

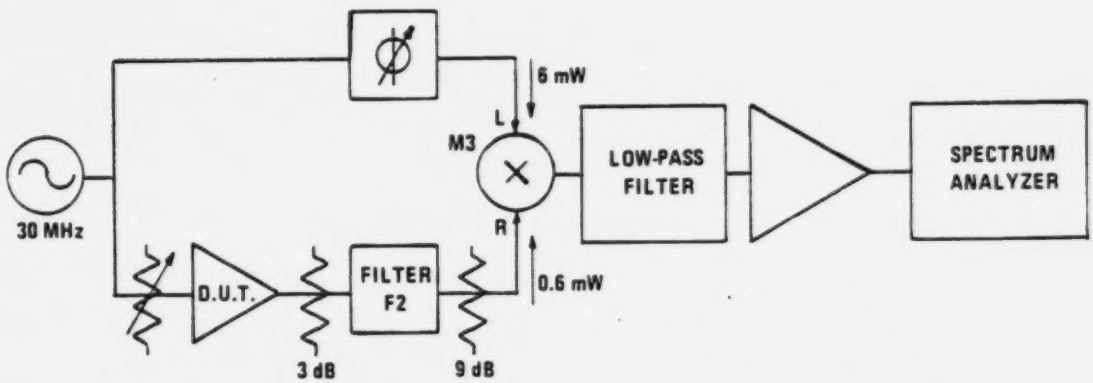

Figure 3-17b. Circuit for Measurement of the Residual Phase Noise of Devices Which Operate at 30 MHz.

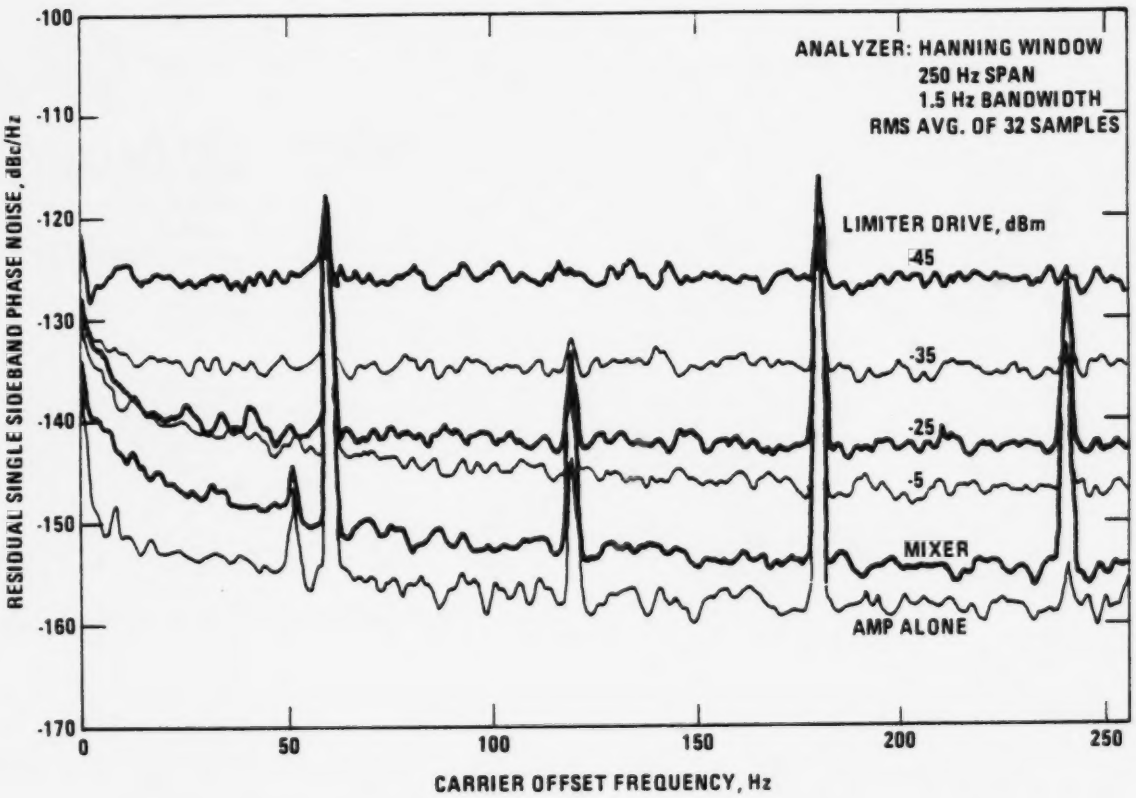

Figure 3-18. Residual Phase Noise of the Limiting Amplifier for a Series of RF Drive Levels.

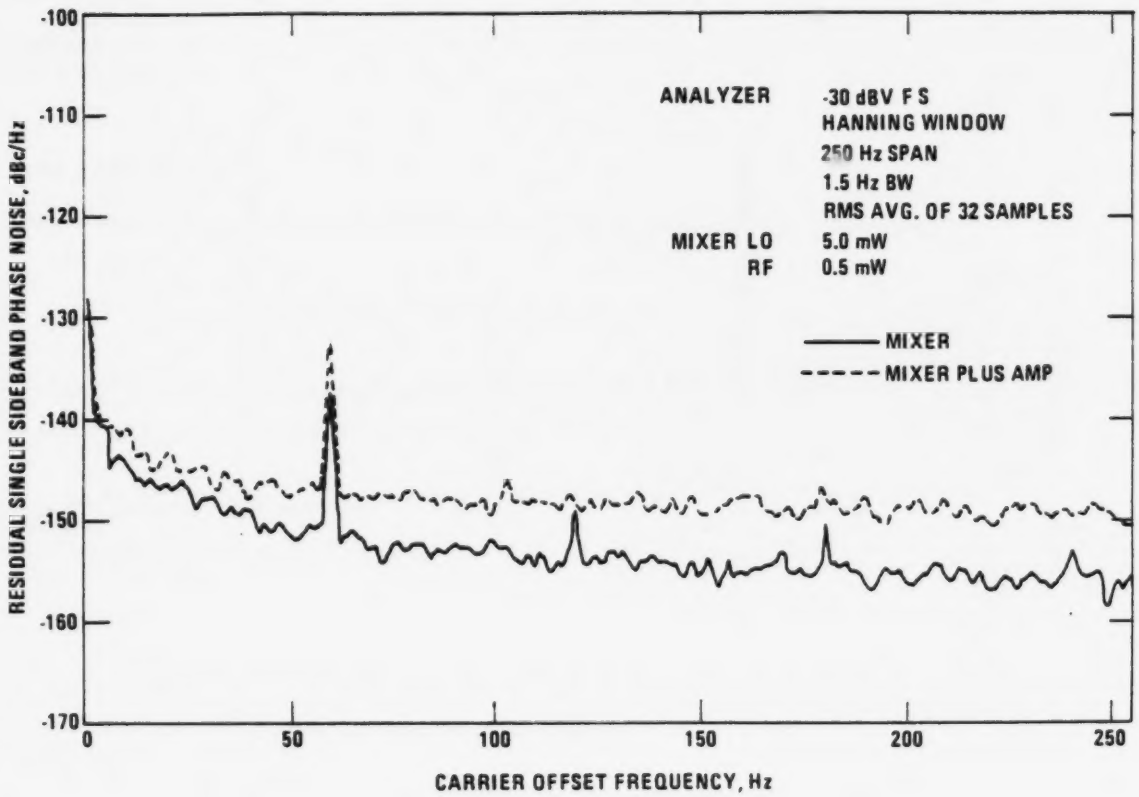

Figure 3-19. Residual Phase Noise of the Low Noise IF Amplifier.

frequencies for high drive levels and the gradual swamping of the flicker noise by the white noise of the limiting amplifier as the RF drive level is reduced. This occurs because as more stages of the limiting amplifier leave the saturation region and enter the active region, the unit behaves more like a high gain amplifier with the overall noise being governed by the thermal noise of the first stage. The large spectral lines in Fig. 3-18 are at the power line frequency and its harmonics. These enter the system via unavoidable ground loops.

Residual Phase Noise of the Low Noise IF Amplifier

The measurement system used for the limiting IF amplifier was used to measure the residual phase noise of the Low Noise IF amplifier. The top trace in Fig. 3-19 is the sum of the amplifier and phase detector noise while the bottom trace is the phase detector noise alone.

A visual comparison of the residual phase noises of the phase detector, limiting amplifier and the Low Noise IF amplifier indicates that the limiting amplifier is the device that will limit the system sensitivity.

Residual Phase Noise of Mixers

Early mixers used point contact diodes which produced a fairly large amount of flicker noise. Newer mixers use Schottky barrier diodes which have reduced flicker noise. Within the family of Schottky diodes the diode construction also greatly affects the mixer noise at low frequencies [Hewlett-Packard Co., 1974] with the following diode types listed in order of decreasing flicker noise: passivated n-type, passivated-p type, hybrid and mesh. Each of these diodes exhibit a 1/f noise power characteristic versus frequency but the noise corner frequency is much less for the mesh diode than for the passivated n-type if all comparisons are performed at the same diode DC current. Besides diode selection, operating the diodes

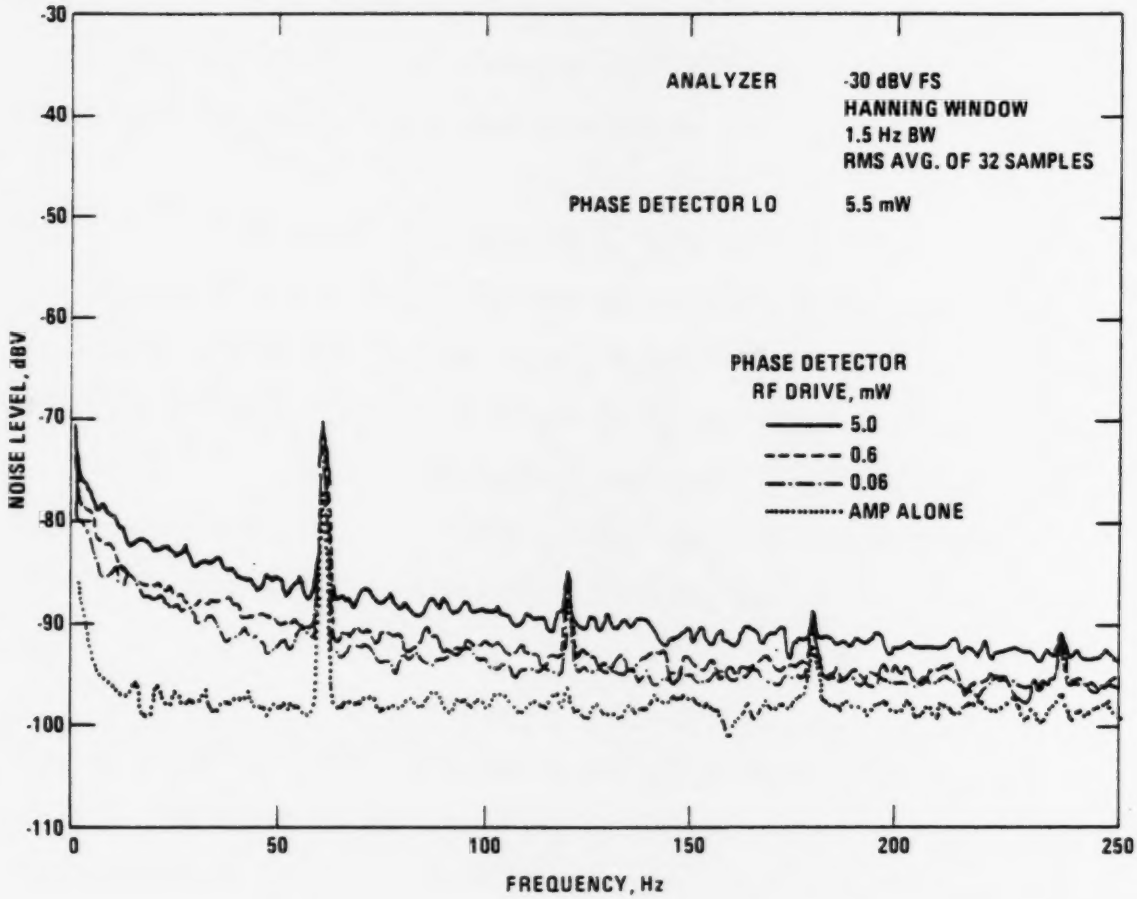

Figure 3-20. Noise of the 30 MHz Phase Detector for a Series of RF Drive Levels.

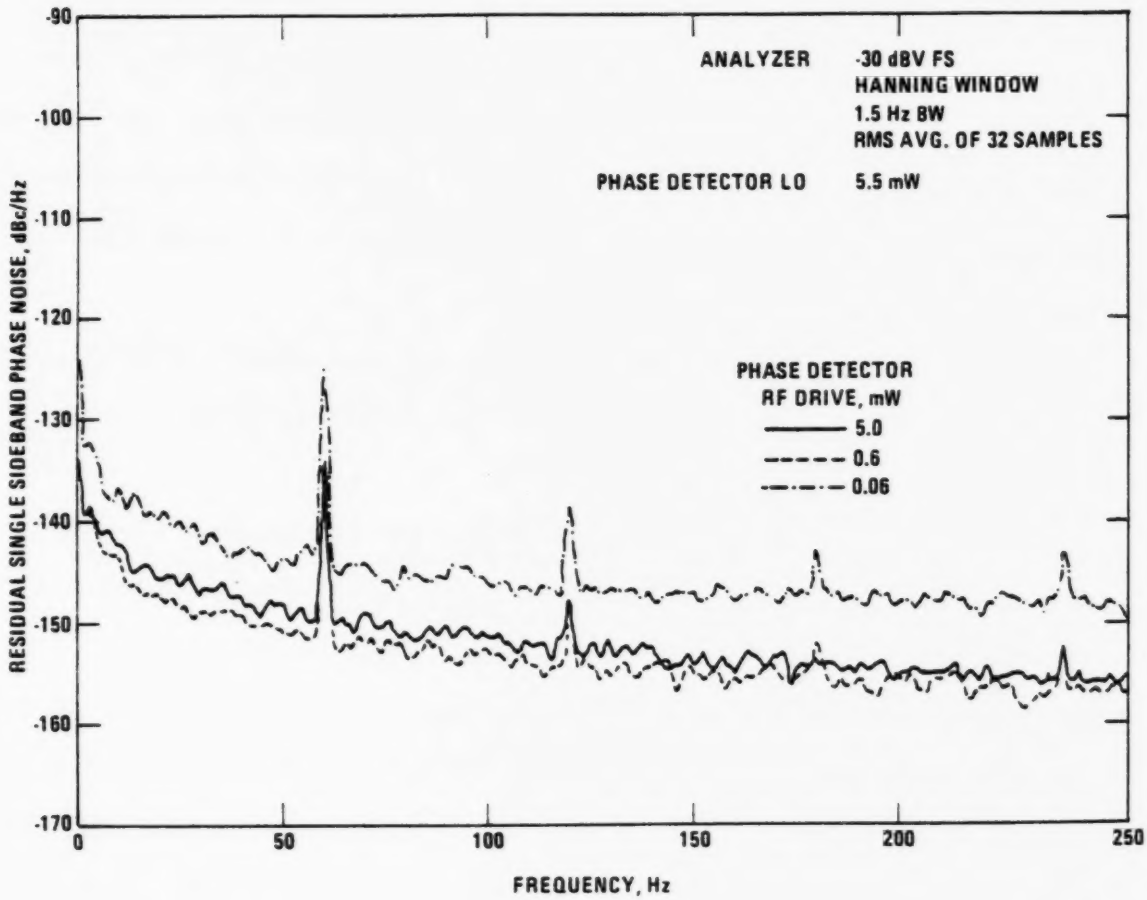

Figure 3-21. Residual Phase Noise of the 30 MHz Phase Detector for a Series of RF Drive Levels.

at low bias currents also significantly reduces flicker noise. The noise temperature ratio, which is the ratio of diode noise power to the power generated by a resistor having the same value of resistance as the diode, is typically reduced about 10 dB as the diode current is reduced from 1 mA to 20 μA. These data were measured [Hewlett-Packard Co., 1974] using DC current. Anand [1969] investigated the generation of flicker noise at audio frequencies by biasing an X-band mixer with an RF signal. He measured the noise temperature ratio of point contact, back, and Schottky diodes under X-band exitation and found that the Schottky diode produced the lowest noise temperature ratios.

Figures 3-20 and 3-21 show the subtle interplay between variables, particularly the RF drive level and the phase detector constant, and how they affect the residual phase noise. Fig. 3-20 shows that actual noise level in dBV at the analyzer versus frequency for various RF drive levels and constant LO power. As expected the lowest absolute noise level is obtained at the lowest RF drive level. Notice that not much change occurs in dropping from the 0.6 mW level to the .06 mW level. This is because the noise at these levels is produced almost entirely by the 5.5 mW LO bias. However as the RF drive level is reduced, so is the phase detector constant (Fig. 3-22) and the reduction in phase detector constant swamps the benefit obtained from the reduced flicker noise. The composite result is shown in Fig. 3-21 where the residual phase noise is plotted versus frequency. Note that the lowest drive level produces the largest SSB phase noise. Figure 3-21 also reveals that there is little change in SSB phase noise at the 5 mW drive level (or at approximately equal LO and RF drive levels) compared to the noise at the 0.6 mW drive level because the increases in absolute

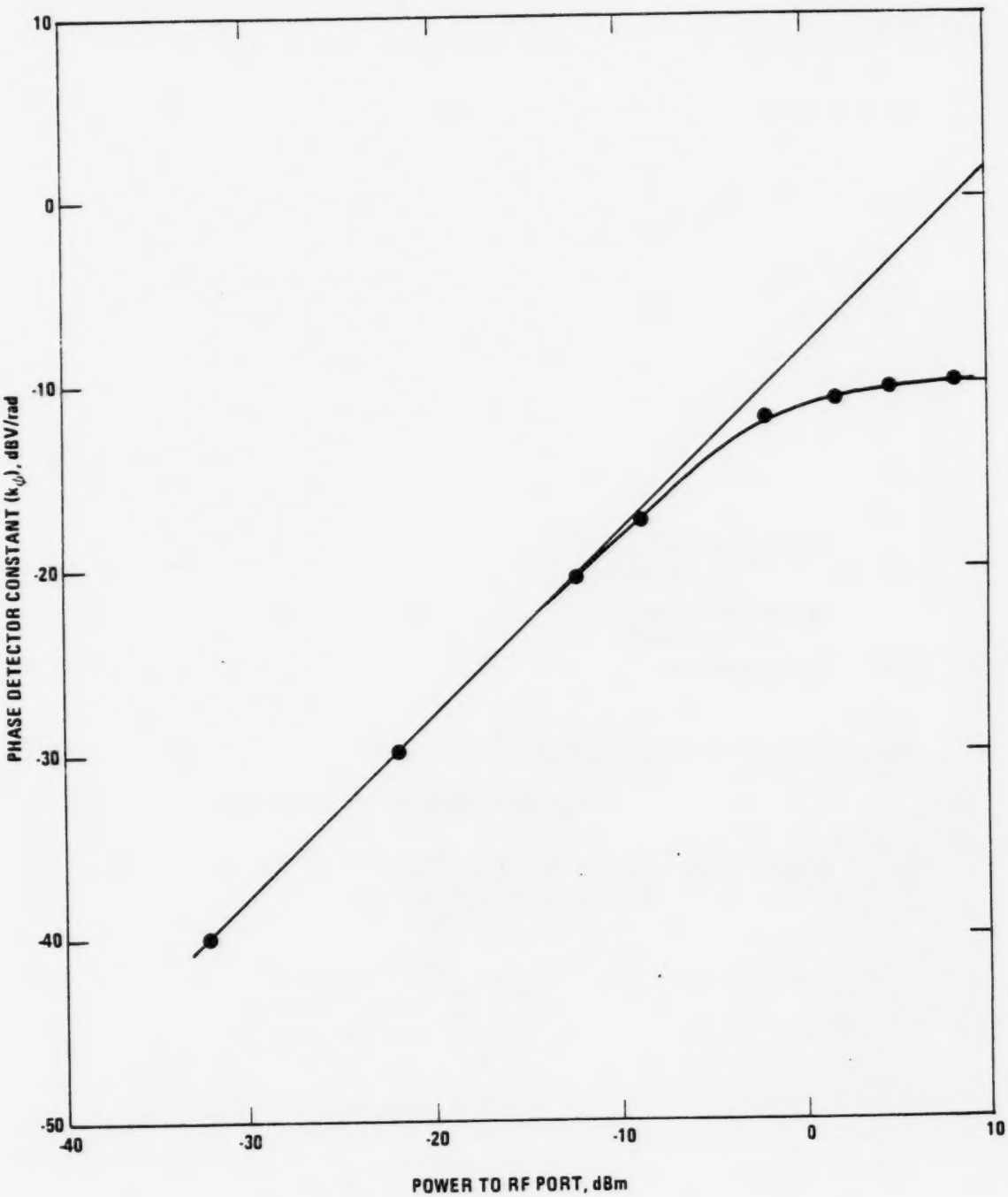

Figure 3-22. Phase Detector Constant ($k\phi$) Versus RF Port Input Level at 6 mW LO Power.

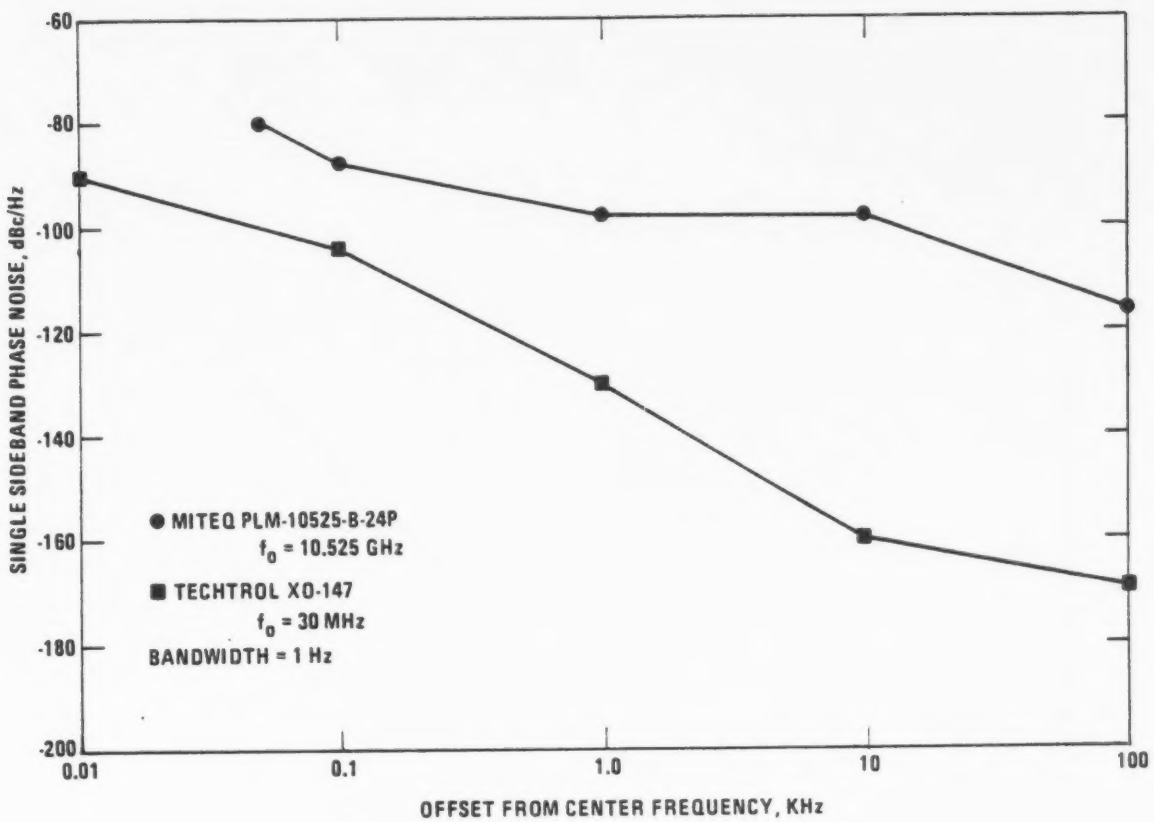

Figure 3-23. Single Sideband Phase Noise of the Receiver System Oscillators.

noise level is closely matched by the corresponding increase in phase detector constant.

3.2.2 Oscillator Phase Noise

All real oscillators have phase noise. If the phase noise of an oscillator is examined in the frequency domain, the noise sidebands will progressively increase as the oscillator's center frequency is approached. When the noise power per unit bandwidth is plotted versus frequency, the frequency dependence will vary from f^0 for white phase noise far from the carrier to f^{-3} for flicker frequency noise close to the carrier [Shoaf et al, 1973; Prouty et al, 1981].

The most sensitive method for measurement of the oscillator phase noise in the frequency domain requires that phase quadrature be maintained between two sources. This amounts to a requirement for a low-noise reference with FM capability. Since this equipment was not available, the manufacturer's specification is presented in Fig. 3-23 instead of actual data. It may appear upon first examination that the sensitivity of the sideband heterodyne receiver described above would be limited to a large degree by the SSB phase noise of the X-band source particularly (since it has much larger noise than the 30 MHz oscillator). It is true that, in general, for long ranges, i.e. for a long time delay between the reference (LO) signal to the phase detector and the signal to the RF port, that the sensitivity would be limited. However the correlation effect, [Skolnik, 1970; Shreve, 1966] derived in Appendix A, reduces the apparent oscillator noise in relation to the factor $f_m T$, the product of the offset frequency from the carrier and the round-trip time delay. The relevant equation (Eq.

A-26) derived in the appendix is

$$\left.\frac{P_{SB}}{P_{DC}}\right|_{dB} = \left. L(f)\right|_{dB} + 19\ dB + 20\ \log\ (f_m T) \qquad (3\text{-}40)$$

For example, if the product $f_m T$ is 10^{-4}, then the noise at the phase detector output is reduced by about 61 dB.

In the receiver system described in section 3.1.3 the transit time to target and back to the receiver will be short. Also f_m is only of interest up to about 200 Hz. An approximate calculation of the path difference in centimeters in the two signals arriving at the phase detector in the sideband heterodyne system used here yields a time delay of about 7.5 ns. The factor, $f_m T$, is then 1.5×10^{-6}, for f_m equal to 200 Hz, the highest frequency of interest. From Table A-1 in appendix A, the apparent reduction in oscillator noise is about 100 dB. For sideband frequencies closer to the carrier, the noise reduction would be even greater. Using Fig. 3-23 the SSB phase noise of the Miteq source at 200 Hz offset from the carrier is -91 dBc/Hz. When the correlation effect is taken into consideration, the apparent noise drops to -191 dBc/Hz at 200 Hz. When compared to other noise considerations, the oscillators in the receiver system used here can be omitted as the devices limiting the sensitivity of the system. This is true because of the short time delays in the receiver.

3.2.3 Mixer Conversion Loss Reduction

In the initial sideband receiver design, mixer M 2 was of the ordinary microwave double-balanced variety requiring 10 mW of LO power. This power was to be supplied with the RF amplifier described earlier. It was shown earlier that the RF amplifier introduced excessive residual phase noise into the system and was therefore deleted from the final design. This

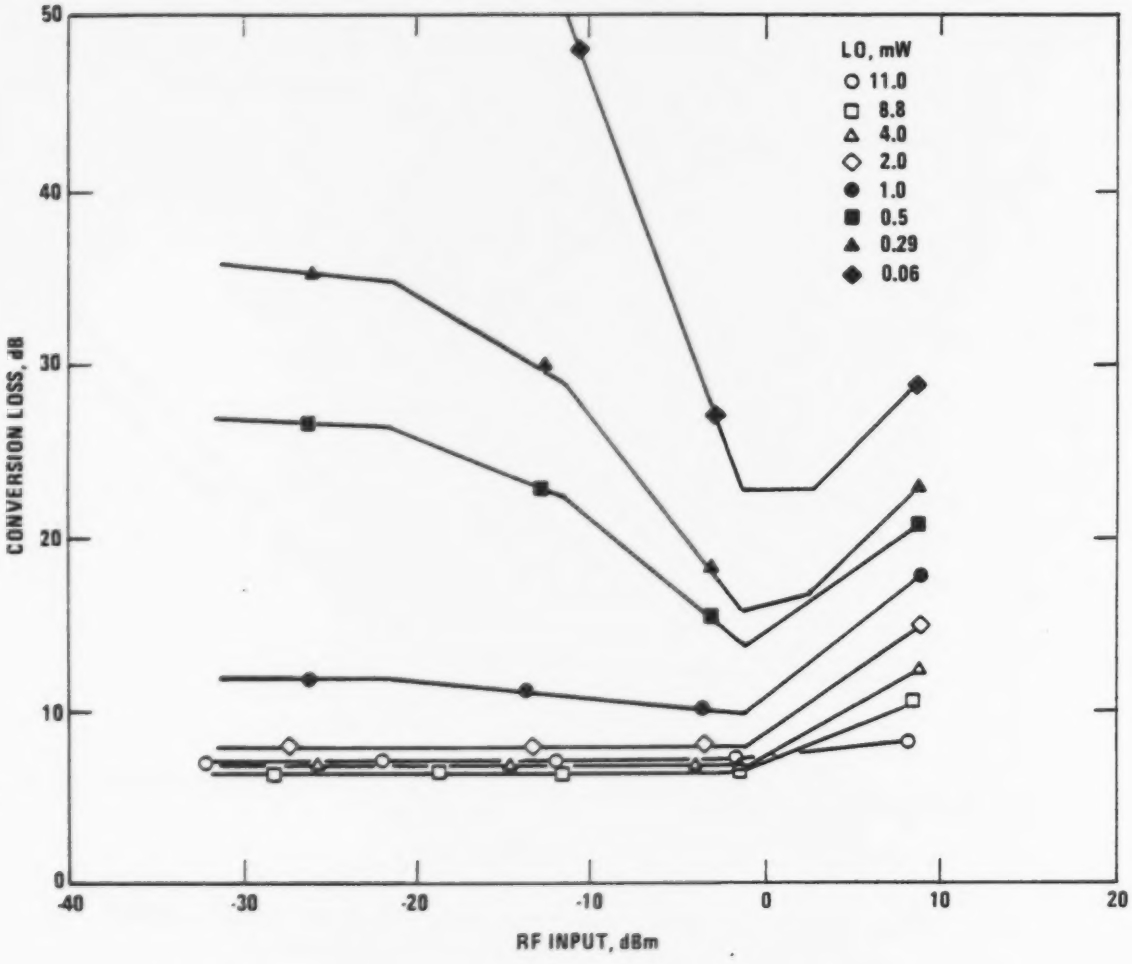

Figure 3-24. Conversion Loss of the Magnum Model MO 64P Mixer Versus RF Input for a Series of LO Power Levels.

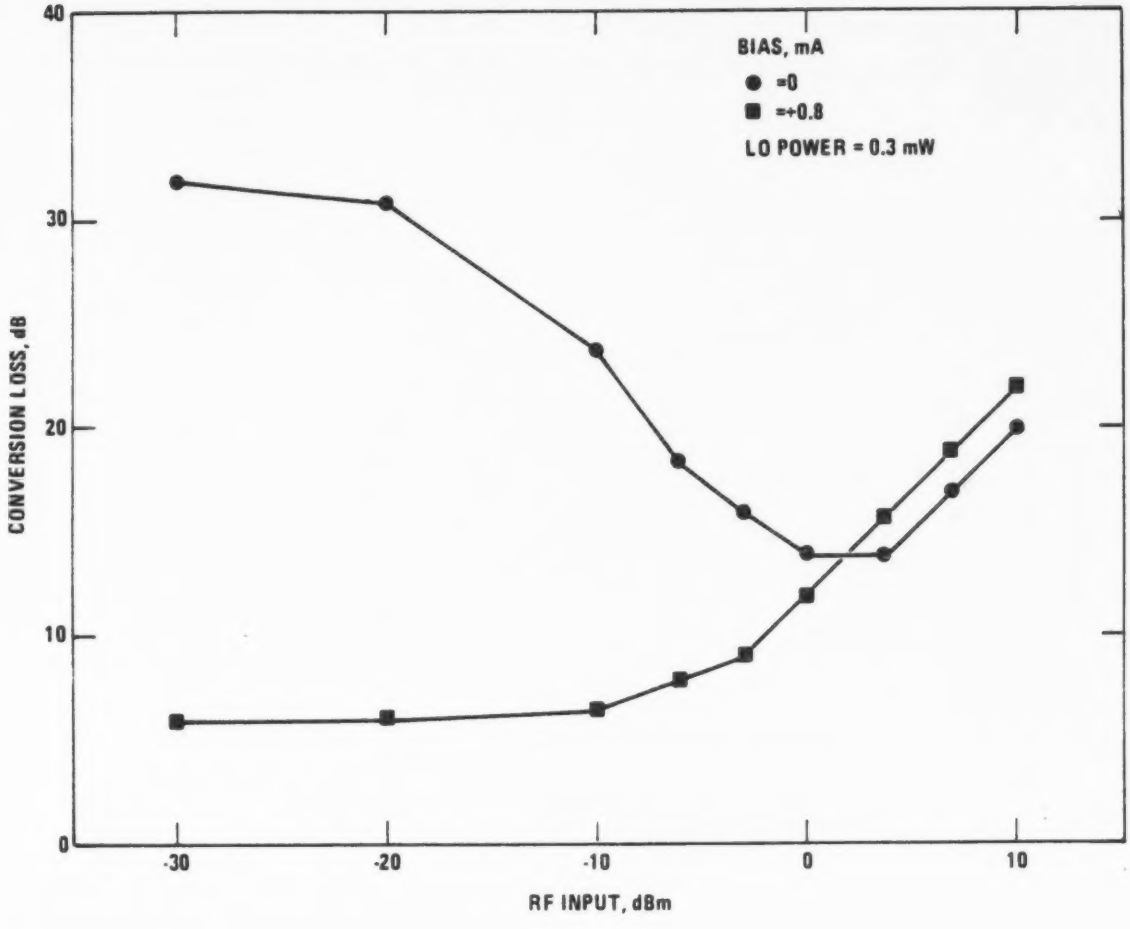

Figure 3-25. Conversion Loss of the Anaren Model 7H0118 Mixer with and without DC Bias.

meant that the Magnum mixer would be operating under starved LO conditions. Data was taken to measure the conversion loss of the mixer for various RF input levels with local oscillator power as the parameter. Fig. 3-24 indicates that for an LO power of less than about 1 mW, the conversion loss is degraded substantially. Without the RF amplifier, the signal at the LO port is about 0.3 mW. Therefore from Fig. 3-24 the conversion loss for an RF input of -20 dBm would result in a conversion loss of about 35 dB.

This problem was solved with the use of an externally biased microwave mixer (Anaren Microwave Inc., Syracuse, NY, Model 7H0118). This mixer is a 90° hybrid, single-balanced mixer with provision for applying a DC bias current to the two diodes. The mixer also has an AC coupled IF port to block the DC voltage from the succeeding stage. Performance of this mixer was measured (Fig. 3-25) at 0.3 mW of LO power for a range of powers to the RF port. The zero bias curve represents operation essentially the same as an ordinary unbiased microwave mixer and this curve can be compared to the corresponding curve in Fig. 3-24. The 0.8 mA bias curve shows the dramatic reduction in conversion loss obtainable under starved LO conditions with an external bias. The final receiver system therefore incorporates this mixer operating at an 0.8 mA bias.

3.2.4 Overall Receiver Sensitivity

Receiver sensitivity is ordinarily specified through the noise figure. The input to this receiver will be defined as the RF input port of mixer M2 (Fig. 3-3). The noise figure for a receiver having a mixer input is [Skolnik, 1962]

$$F|_{dB} = L_c|_{db} + 10 \log(t_r + F_{IF} - 1) \qquad (3\text{-}41)$$

where L_c is the conversion loss of the mixer, t_r is the noise temperature ratio of the mixer diodes, and F_{IF} is the noise figure of the IF amplifier following the mixer. The noise temperature ratio has an inverse frequency relationship in the flicker noise frequency range (<~200 kHz). Above this frequency the noise temperature ratio approaches unity. Since the IF frequency in this receiver is 30 MHz, the noise temperature ratio can be considered unity and the receiver noise figure becomes

$$F(dB) = L_c + F_{IF}\ dB. \qquad (3\text{-}42)$$

Knowing the noise figure, the receiver sensitivity in dBm can be computed with the following equation:

$$\text{Sensitivity (dBm)} = F(dB) + 10 \log (kT) + 10 \log B \qquad (3\text{-}43)$$

where k is Boltzman's constant, T is absolute temperature in Kelvin degrees and B is the equivalent noise bandwidth. At room temperature the quantity kT is equal to -174 dBm/Hz. Also for all phase noise and sensitivity measurements the equivalent noise bandwidth is determined by the spectrum analyzer since it is the narrowest band component in the system. For the 250 Hz range and with a Hanning passband-filter shape the analyzer has a 1.5 Hz noise bandwidth. The sensitivity can therefore be written as

$$\text{Sensitivity (dBm)} = F(dB) + 1.8 - 174 \qquad (3\text{-}44)$$

or

$$\text{Sensitivity (dBm)} \approx F(dB) - 172\ dBm. \qquad (3\text{-}45)$$

Equations 3-42 and 3-45 would yield the true receiver noise figure and sensitivity respectively if Johnson noise were the main contributor to each measure. However in previous sections we have demonstrated that with high dynamic range signals (i.e. small sidebands with respect to the carrier) the residual phase noise generated by components in the system can limit

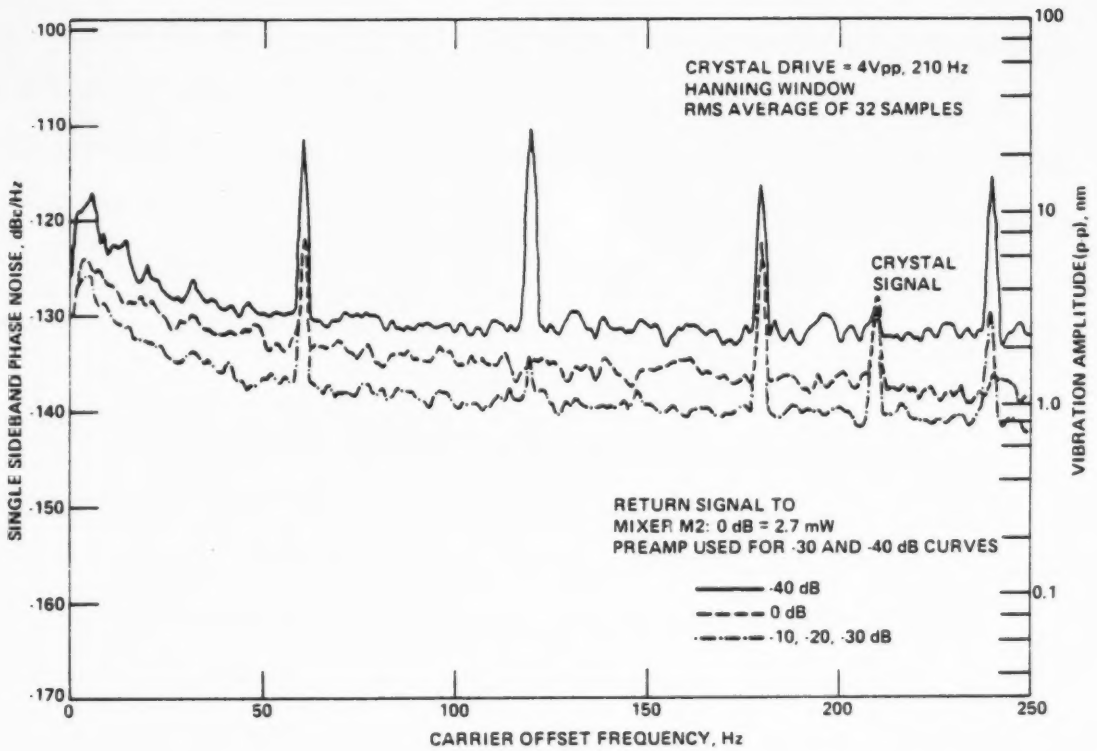

Figure 3-26. Receiver Sensitivity Versus Carrier Offset Frequency for a Series of Signal Strengths.

the receiver sensitivity. A comparison of the actual measured sensitivity compared to the value calculated with Eq. 3-45 is instructive.

The sensitivity of the sideband heterodyne receiver in terms of its overall single-sideband phase noise (L(f)) up to 250 Hz offset frequency for a series of signal strengths is shown in Figure 3-26. The phase noise was measured over a 40 dB range of signal strength in 10 dB increments with 0 dB corresponding to 2.7 mW. On the right side of the figure the equivalent peak to peak vibration amplitude is specified. The actual sensitivity (noise power) in dBm can be found from Fig. 3-26 if the signal power in dBm is added to the quantity L(f). The actual sensitivity was determined using Fig. 3-26 at 12.5, 25, 50, 100 and 250 Hz over the 40 dB signal level range and is presented in Table 3-2.

To compute the sensitivity based on the noise figure and Eq. 3-43, the conversion loss of mixer M2 must be determined at the signal strengths used in Fig. 3-26. The curve for the conversion loss of mixer M2 versus RF input power was already presented in Fig. 3-25. Using this figure and Eq. 3-42 the receiver noise figure was calculated and is presented in Table 3-3. It should be noted that the noise figure of the limiting amplifier (10 dB) was used as F_{IF} for the first three signal levels and that the noise figure the low noise IF amplifier (1 dB) was used for the last two signal levels. With the calculated receiver noise figure versus signal strength now in hand, Eq. 3-45 can be used to compute the sensitivity. The results are also shown in Table 3-2. For example at a signal level of +4.3 dBm the receiver noise figure is 24 dB and subtracting 172 dBm yields a calculated sensitivity of -148 dBm.

Table 3-2

Comparison of the Receiver Sensitivity Calculated from the Noise Figure and the Actual Receiver Sensitivity at Selected Carrier Offset Frequencies for a Series of Carrier Signal Levels

Mixer M2 Signal Level (dBm)	Sensitivity from Noise Figure (dBm)	Actual Sensitivity (dBm)				
		Carrier Offset Frequency (Hz)				
		12.5	25	50	100	250
+ 4.3	-148	-123.2	-125.7	-128.2	-130.7	-134.2
- 5.7	-154	-133.7	-137.2	-140.7	-143.2	-146.7
-15.7	-156	-146.7	-149.7	-152.7	-154.7	-156.7
-25.7	-165	-156.7	-159.7	-162.7	-164.7	-166.7
-35.7	-165	-158.2	-162.7	-165.7	-166.7	-167.7

Table 3-3

Mixer M2 Conversion Loss and Calculated Receiver Noise Figure for a Series of Signal Levels

Mixer M2 Signal Level (dBm)	Mixer M2 Conversion Loss (dB)	Noise Figure (dB)
+ 4.3	14	24
- 5.7	8	18
-15.7	6	16
-25.7*	6	7
-35.7*	6	7

* The Low Noise Pre-Amp was used for these measurements.

Table 3-2 shows clearly that for most signal levels and offset frequencies, the actual sensitivity is less than that predicted by using the noise figure data. Only for small signal levels and relatively large offset frequencies do the measured sensitivities agree with the values calculated from the noise figure. The table has been divided into two regions by a dashed line. Above the dashed line the sensitivity is controlled by the receiver 1/f noise while below the line the sensitivity is controlled by thermal noise and in this region it is predicted by Eq. 3-43.

In the region above the dashed line where flicker noise predominates the equivalent noise figure for the receiver can be calculated with the following equation:

$$F_{eq} = \text{Actual Sensitivity (dBm)} + 172. \qquad (3\text{-}46)$$

For example, at an offset frequency of 12.5 Hz and at a signal strength of +4.3 dBm the equivalent receiver noise figure is

$$F_{eq} = -123.2 + 172 = 48.8 \text{ dB}.$$

This is 24.8 dB larger than the noise figure that would be expected from Eq. 3-42.

The receiver sensitivity can also be improved if the time averaging capabilities of the spectrum analyzer are employed. If a sample of the audio oscillator signal is fed to the external trigger input as a synchronizing signal, the effective signal to noise ratio can be improved by up to 24 dB. Figure 3-27 compares the receiver sensitivity with 256-sample, time averaging to the sensitivity with 64-sample RMS averaging.

3.3 Calibration

Although the signal reflected from a linearly vibrating target can be

calculated, many factors must be known as the signal passes from the receiver input to the analyzer display that affect the measurement of the vibration amplitude. Among these are the phase detector constant k_ϕ, the gain of the baseband amplifier and the calibration of the spectrum analyzer. The purest method of verifying the calibration of the receiver is to provide a vibrating object which has a known vibration frequency and amplitude in the same ranges that are expected from the samples to be placed in the exposure cell. A piezoelectric crystal fulfills this need well.

An eleven-thirty-seconds inch (8.73 mm) diameter by one-eighth inch thick piezoelectric crystal (Wilcoxon Research, Rockville, MD, Model PZT 5H) was placed in the center of the calibration cell as shown in Fig. 3-3. Wires were soldered to each side of the crystal and routed to a coaxial connector mounted on an X-band waveguide flange. The wires were positioned perpendicular to the X-band field to minimize scattering from the wires. One wire was grounded at the waveguide flange.

The vibration amplitude of the crystal can be determined through the piezoelectric charge coefficient. The charge coefficient relates the charge generated by the crystal when a force is applied, or the displacement of the crystal when a voltage is applied. For the Model PZT 5H the charge coefficent is 590×10^{-12} m/V. If the crystal is excited by a four volt peak-to-peak sine wave signal, the crystal will vibrate at the excitation frequency with an amplitude of 2.36 nm pp.

The sideband to carrier ratio for the received signal was derived in Chapter 2 (Eq. 2-26). In that expression, x_o was half the peak-to-peak amplitude of the vibration. Calculating the sideband to carrier ratio for the 2.36 nm crystal vibration we get

$$SSBCR = 20 \log_{10} \frac{\pi(2x_o)}{\lambda} \qquad (3\text{-}47)$$

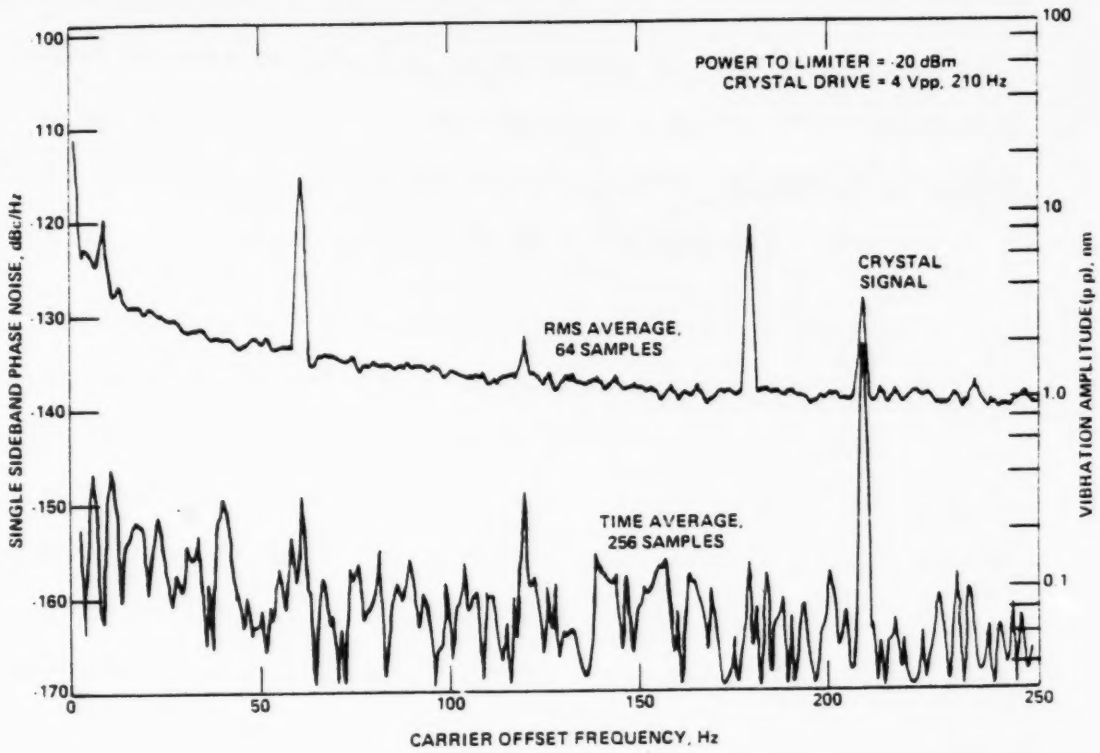

Figure 3-27. Receiver Sensitivity Versus Carrier Offset Frequency with Time Averaging.

$$SSBCR = 20 \log_{10} \frac{\pi \cdot 2.36 \text{ nm}}{28.5 \times 10^6 \text{ nm}} = -131.7 \text{ dBc}$$

where λ is the wavelength of the X-band oscillator frequency.

In Section 3.2.1, Eq. 3-39 was developed for making phase noise measurements. Since the phase noise is a broadband signal, the terms L(f) and V_{anal} are specified on a per root hertz basis. Now with application of a discrete signal to the piezoelectric crystal, the expected receiver output signal will also be a discrete signal. Hence, Eq. 3-39 can be modified as follows to yield the Single Sideband to Carrier Ratio (SSBCR)

$$SSBCR\Big|_{db} = + V_{anal}\Big|_{dBV} - 65 \text{ dB} - 20 \log (2k_\phi). \qquad (3\text{-}48)$$

To make quantitative measurements of displacement, the phase detector constant must be measured as well as the signal from the receiver to the spectrum analyzer (V_{anal}). We may observe at this time that the limiting amplifier will tend to keep k_ϕ fairly constant because the limiting amplifier provides a nearly constant output signal over a large range of input signal levels. The phase detector constant was measured by switching the waveguide switch to the calibration cell, turning on the receiver components and adjusting the manual phase shifter for a maximum DC voltage at the phase detector output. (A DC voltmeter was temporarily connected to the phase detector output for this step and for the step to follow.) The phase detector constant in units of V/rad is numerically equal to the voltmeter reading in volts. The manual phase shifter was then adjusted for zero volts DC to set up the receiver for quadrature phase detection as discussed in Section 3.2.1. The voltmeter was then disconnected and the Low Noise Baseband Amplifier reconnected to the phase detector. With the receiver set up for quantitative measurements, the audio oscillator was activated with the signal to the piezoelectric crystal adjusted to 4 V peak to peak.

Since we wished to determine whether the calibration would be affected by the received power level, an RF attenuator was temporarily placed between the splitter and the circulator (Fig. 3-3). Table 3-4 presents the measured and expected SSBCR for a series of power levels at port R of mixer M2. Table 3-4 shows that the receiver is accurate to within 5.9 dB over a 40 dB range of input power levels.

Table 3-4

Comparison of Measured and Expected Single Sideband Carrier Ratios (SSBCR) for a Series of Received Power Levels

Mixer M2 Input Power (dBm)	Expected SSBCR (dBc)	Measured SSBCR (dBc)	Error (dB)
+ 4.31	-131.7	-126.9	+4.8
- 5.69	-131.7	-125.8	+5.9
-15.69	-131.7	-127.6	+4.1
-25.69*	-131.7	-125.9	+5.8
-35.69*	-131.7	-126.6	+5.1
		mean:	+5.1

*The Low Noise Pre-Amp was used for these measurements.

Chapter IV

EXPOSURE CELL DESIGN

4.1 Exposure Cell Design Approach

An exposure cell was needed to allow for the simultaneous exposure of a tissue sample to a low frequency or low-frequency amplitude-modulated electric field while permitting the simultaneous non-contacting monitoring of the expected mechanical vibration of the sample by an X-band RF signal. Waveguide is an excellent transmission line for X-band signals because losses are low and the waveguide dimensions are reasonable. An exposure cell design was therefore sought which incorporated a waveguide; however a waveguide cannot by itself support the propagation of a low frequency field, i.e. a field with a frequency below the waveguide cutoff frequency. A rectangular coaxial line (or strip line) on the other hand can support waves having a frequency from zero hertz on up. The upper frequency limit of a strip line is usually set by the cutoff frequency of the first higher order mode. The strip line offers shielding from external fields, a uniform field near the center of the cross section and wide frequency coverage. An exposure cell integrating a strip line and a waveguide was thought therefore to be a suitable design. A drawing of the cell is shown in Fig. 4-1.

4.2 Properties of the Exposure Cell

The properties of the exposure cell can be divided into two groups: 1) the waveguide properties for the X-band signal; 2) the strip line properties

EXPOSURE CELL

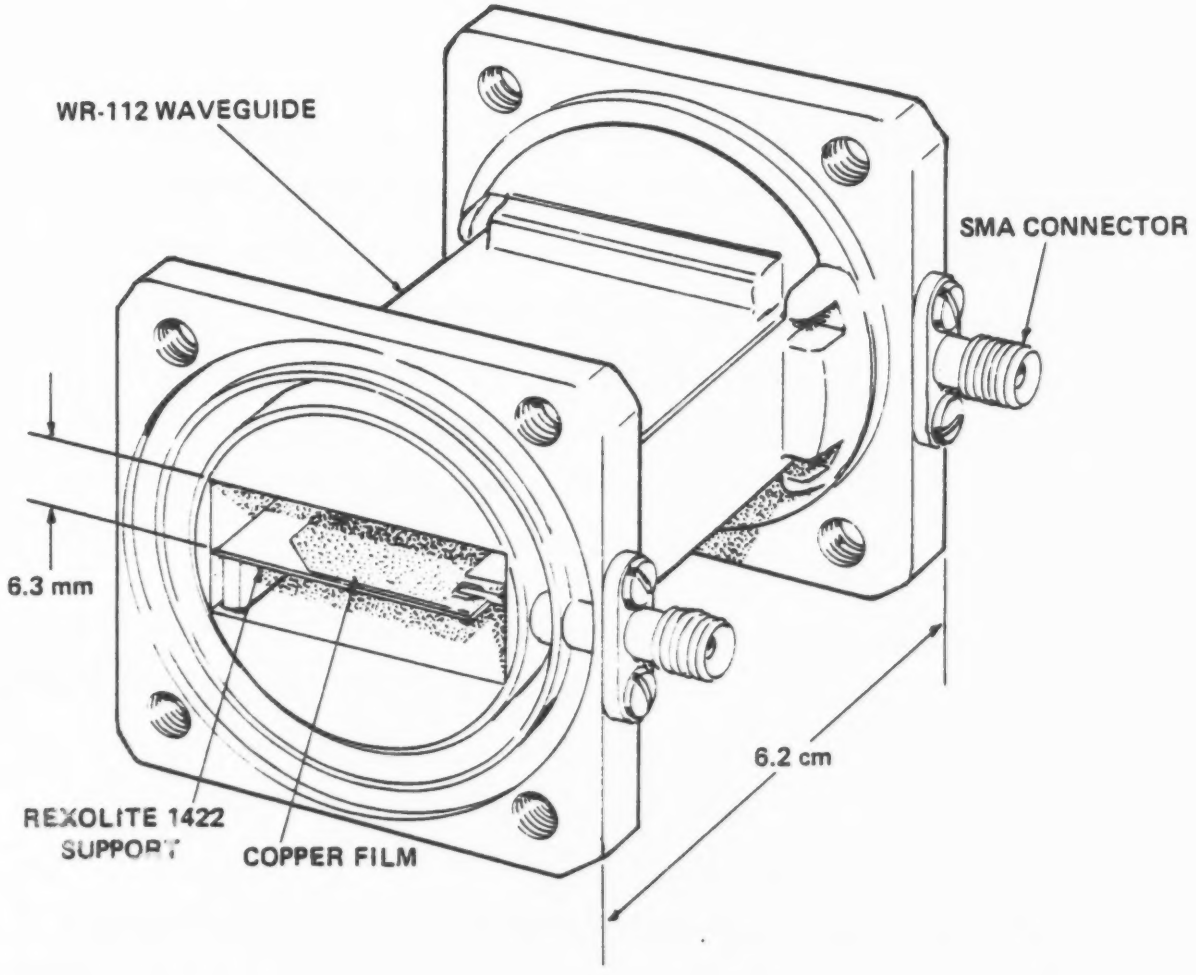

Figure 4-1. The Exposure Cell.

for the low frequency or modulated signal. The X-band signal propagates through the waveguide in the TE_{10} (transverse-electric) mode which means that there is no electric field due to the X-band signal along the length of the waveguide, that there is no change in electric field between the broad walls of the waveguide, and that the magnitude of the electric field between the narrow walls of the guide varies as a half-sinusoid from one narrow wall to the other. The TE_{10} mode has a cutoff frequency given by Eq. 4-1

$$(f_c)TE_{10} = 1/2a\sqrt{\mu\varepsilon} \tag{4-1}$$

where a is the width of the broad wall in meters. For the WR-112 waveguide shown in Fig. 4-1, the cutoff frequency of the TE_{10} mode is 5.26 GHz. Since electric-field lines terminate on the broad walls, each imaginary straight line between the narrow walls of the waveguide is along an equipotential surface. A conductor can be placed along an equipotential surface without disturbing the electric field. Therefore the center conductor of the strip line is expected to only minimally perturb the field of the X-band signal.

For a waveguide cross section as shown in Figure 4-2, the mode cutoff frequencies are given by Eq. 4-2

$$(f_c)_{mn} = \frac{1}{2\sqrt{\mu\varepsilon}} \sqrt{(m/a)^2 + (n/b)^2} \tag{4-2}$$

where m and n are integers. If the ratio of Eq. 4-2 to Eq. 4-1 is formed we get

$$\frac{(f_c)_{mn}}{(f_c)_{TE_{10}}} = a\sqrt{(m/a)^2 + (n/b)^2} \tag{4-3}$$

which is the ratio of the cutoff frequency of any mode to the cutoff frequency of the TE_{10} mode. Evaluating this for the first four higher order modes we get the results shown in Fig. 4-3. Since the TE_{10} cutoff frequency for WR-112

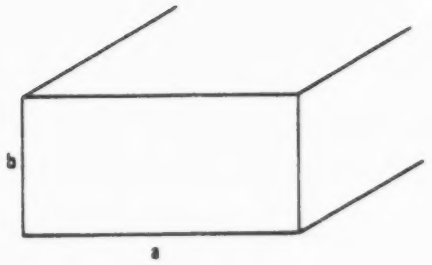

Figure 4-2. Waveguide Cross-Section.

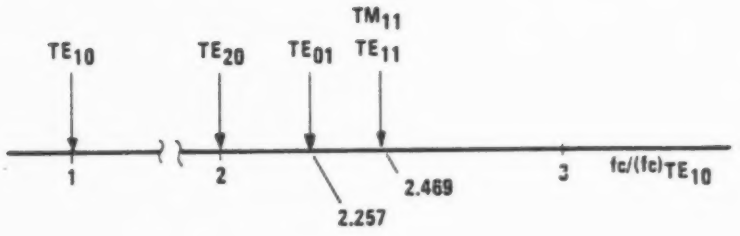

Figure 4-3. Diagram of the First Few Field Modes of WR-112 Waveguide.

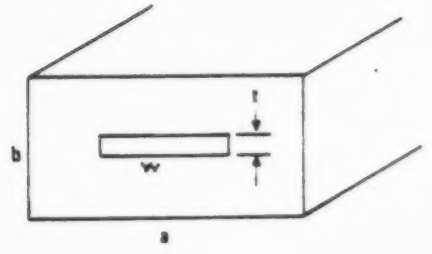

Figure 4-4. Exposure Cell Cross-Section.

waveguide is 5.26 GHz, the cutoff frequencies of the higher order modes for this waveguide are 10.52 GHz for the TE_{20}; 11.87 GHz for the TE_{01}; and 12.99 GHz for the TE_{11} and TM_{11} modes. The TE_{01}, TE_{11} and the TM_{11} higher order modes will not be generated in the exposure cell because the operating frequency of 10.525 GHz is below the cutoff frequency for these modes. Although the TE_{20} mode could conceivably be excited, the operating frequency is so close to the TE_{20} mode cutoff frequency that this mode would have a large attenuation constant.

The stripline portion of the exposure cell incorporates several design considerations: characteristic impedance; operating frequency range and impedance match of the end connections. The characteristic impedance of strip lines are a function of the cross-sectional dimensions of the line shown in Fig. 4-4. Once a/b is selected, w/b and t/b determine the characteristic impedance with Z_0 increasing as w/b decreases and Z_0 increasing as t/b decreases. Since the exposure cell uses WR-112 waveguide, the a and b dimensions are fixed and the ratio a/b is 2.257. The strip line center conductor as shown in Fig. 4-1 is made with 1 oz. copper clad 1/32" Rexolite 1422 which is a cross-linked styrene copolymer having a low dissipation factor up to 24 GHz. For a 1 oz. copper plating, the actual copper film thickness is 0.00135". Joines [1964] derived the effect of a center conductor with finite but small thickness, t, on the characteristic impedance of the strip line. Weil [1978] plotted the results of Joines' theoretical work. Using Weil's curves in Fig. 2 of his paper it is evident that the copper foil thickness in our exposure cell strip line is so thin that it does not influence the characteristic impedance. Joines' derivation is valid for the ratio $t/b \leq 0.1$ and for the ratio $w/(b-t) \geq 0.35$. These two ratios for the exposure cell strip line are 0.003 and 1.4 respectively. Therefore Joines'

work is applicable to this case. Since the center conductor does not influence the characteristic impedance, then a simpler model - the model for a zero thickness center conductor strip line - derived by Cohn [1955] can be used to determine the width of the center conductor. Using a design curve prepared by Weil [1978] in his Fig. 1, a value of w equal to 0.688 in. was selected. The equations that determine the characteristic impedance for a strip line with zero thickness center conductor are

$$Z_0 = \frac{376.73}{4[w/(b-t) + C_f'/\varepsilon]} \tag{4-4}$$

and

$$\frac{C_f'}{\varepsilon} = \frac{2}{\pi} \ln[1 + \coth \pi\left(\frac{a-w}{2b}\right)]... \tag{4-5}$$

where C_f' is the fringing capacitance per unit length. Using these equations to check the value of center conductor width determined graphically we get a computed characteristic impedance of 50.4 ohms. The actual strip line will have a characteristic impedance somewhat below this value because Eq. 4-4 and 4-5 were solved using an air dielectric. The center conductor is actually a section of microstrip line and the dielectric base of the section will increase the capacitance of the strip line slightly thus lowering the effective characteristic impedance.

The desired mode of operation for the strip line portion of the exposure cell is the TEM mode. However any TEM line such as a coaxial cable, rectangular coaxial lines and parallel plate lines can support higher order modes if these lines are driven with a high enough frequency. The problem then becomes knowing at what frequency the higher order modes can begin to propagate. Until recently it was thought that the first higher order mode in a rectangular coaxial line would be the first waveguide mode, i.e. the TE_{10} mode [Crawford, 1974]. Recent work by Gruner [1979] and Weil et al [1981] have shown that

tnis is not always true. For example, for an a/b ratio of 1.0, i.e. a square cross-section, the TE_{01} mode has a lower cutoff frequency than the TE_{10} mode for all values of w/a and hence will be the first mode to be excited as the frequency is increased. For larger aspect ratios, as the a/b ratio is called, the TE_{01} mode has the lowest cutoff frequency only if the w/a ratio is above some value. For the exposure cell used here, the aspect ratio (a/b) is 2.257 and the w/a ratio is 0.620. For these values Weil's curves indicate that the TE_{10} mode, the dominant waveguide mode, has the lowest cutoff frequency. This frequency was computed above and is 5.26 GHz. Therefore to expose a biological sample in the cell to a uniform and predictable electric-field pattern, the frequency of the signal applied to the strip line must be kept below 5.26 GHz.

4.3 Performance

The performance of the exposure cell was determined by performing certain standard measurements on the cell. As explained in an earlier section the signal scattered back to the receiver from the target must be the largest signal that the receiver sees in order to maintain system calibration. If the strip line were to scatter a larger portion of the incident X-band signal back to the receiver than the target, calibration would be lost. The voltage standing wave ratio (VSWR) of the exposure cell with one end of the waveguide terminated with a waveguide load was measured. The measured value of VSWR, 1.06, means that less than 0.1% of the incident X-band power will be reflected back toward the receiver. Since a typical tissue-equivalent sample is expected to scatter a much larger portion of the incident energy, the performance of the strip line should be perfectly adequate.

The performance of the strip line portion of the cell was measured using a scalar network analyzer (Pacific Measurements, Inc., Palo Alto, CA, Model 1038) to measure the return loss. Return loss is the ratio of the RF power reflected at a port to the power incident to that port and it is usually expressed in decibels. An arbitrary return loss of 20 db was selected as the minimum value required for suitable operation. If the return loss is greater than 20 dB, this implies that the VSWR is less than 1.22 and that the reflected power is less than 1%. The return loss data for the exposure cell with one of the coaxial ports terminated with a coaxial 50 ohm load is shown in Fig. 4-5 which shows that the return loss remains greater than 20 dB up to 1 GHz. It was shown above that the first higher order mode occurs at 5.26 GHz therefore a signal introduced to the strip line through the coaxial ports should remain in the TEM mode at least up to 1 GHz.

The information shown in Fig. 4-5 is complemented very nicely by the information obtained with a time domain reflectometer (TDR). Whereas the return loss plot gives impedance matching information versus frequency but no spatial information concerning where the transmission line is mismatched, the TDR provides spatial information but no frequency information. In an earlier version of the exposure cell a TDR (Hewlett Packard, Palo Alto, CA Model 1815B/1817A) was very useful in revealing where a relatively strong mismatch was occurring. Fig. 4-6 shows the TDR plot obtained with the exposure cell. The two large upward peaks are due to the coax-to-strip line transitions. The width and height of these peaks indicate the series inductance present at the transitions. The region between the peaks indicate the strip line section and the region to the right of 1.4 ns represents the coaxial load.

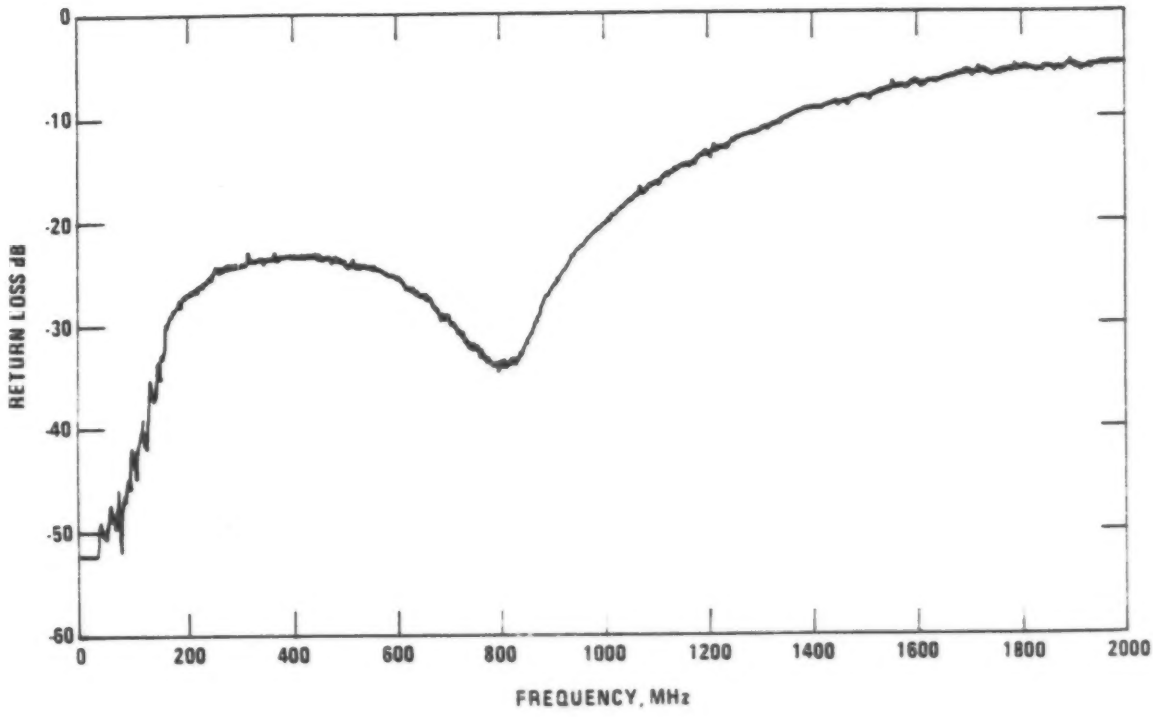

Figure 4-5. Exposure Cell Return Loss at the Coaxial Port.

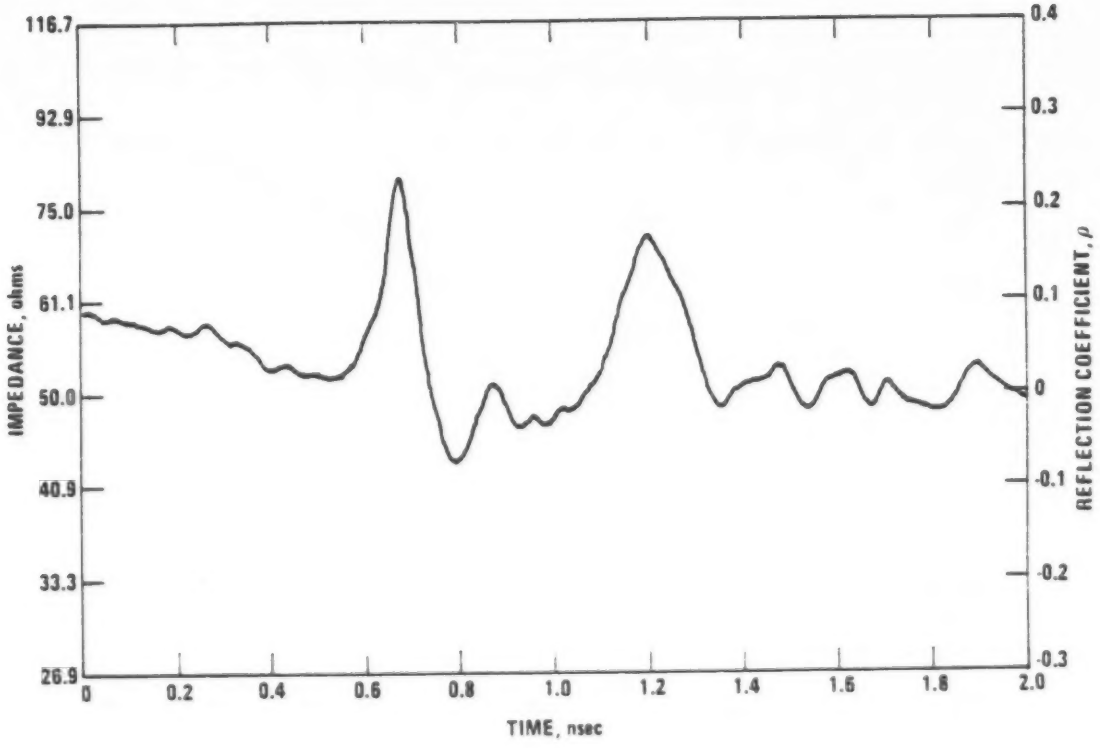

Figure 4-6. Exposure Cell TDR Plot at the Coaxial Port.

Chapter V

DEFLECTION OF TISSUE MODELS

5.1 Derivation of Electrostrictive (Maxwell Stress) Force

In this section the force per unit area at a dielectric interface due to electrostrictive forces will be derived for the cases of the electric fields normal and tangent to the dielectric interfaces. These results will be used in subsequent sections to compute the forces and motion of certain molded tissue models for comparison with experimental data.

If we have a region V in space containing a charge distribution, ρ, and a current density distribution, $\overline{J}$, the total force acting on the system of charges and currents is given by the Lorentz force law [Paris and Hurd, 1969]:

$$\overline{F} = \int_V [\rho\overline{E} + \overline{J}x\overline{B}]dv \qquad (5\text{-}1)$$

where the field vectors represent the total field due to sources both inside and outside the region, V. This expression can be developed into a surface integral containing only surface fields. The development follows the outline presented by Joines et al [1981]. Two of Maxwell's equations are

$$\nabla X\overline{H} = \overline{J} + \frac{\partial\overline{D}}{\partial t} \qquad (5\text{-}2)$$

or

$$\overline{J} = \nabla X\overline{H} - \frac{\partial\overline{D}}{\partial t} \qquad (5\text{-}3)$$

and

$$\overline{\nabla}\cdot\overline{D} = \rho. \qquad (5\text{-}4)$$

Substituting Eq. 5.4 and Eq. 5.3 into Eq. 5.1 we get

$$\overline{F} = \int_V [(\nabla\cdot\overline{D})\overline{E} + (\nabla X\overline{H} - \frac{\partial\overline{D}}{\partial t})X\overline{B}]dv. \tag{5-5}$$

Note that

$$(\nabla\cdot\overline{B})\overline{H} + (\nabla X\overline{E} + \frac{\partial\overline{B}}{\partial t})X\overline{D} = 0 \tag{5-6}$$

because by Maxwell's equations

$$\nabla\cdot\overline{B} = 0 \tag{5-7}$$

and

$$\nabla X\overline{E} = -\frac{\partial\overline{B}}{\partial t}. \tag{5-8}$$

It is possible to add the terms on the left of the equals sign in Eq. 5-6 to the integrand of Eq. 5-5 without changing the equation. The result is

$$\overline{F} = \int_V [(\nabla\cdot\overline{D})\overline{E} + (\nabla X\overline{H} - \frac{\partial\overline{D}}{\partial t})X\overline{B} + (\nabla\cdot\overline{B})\overline{H} + (\nabla X\overline{E} + \frac{\partial\overline{B}}{\partial t})X\overline{D}]dv \tag{5-9}$$

Collecting terms we get

$$\overline{F} = \int_V [\overline{E}(\nabla\cdot\overline{D}) - \overline{D}X(\nabla X\overline{E})]dv + \int_V [\overline{H}(\nabla\cdot\overline{B}) - \overline{B}X(\nabla X\overline{H})]dv$$
$$- \int_V [\frac{\partial\overline{D}}{\partial t}X\overline{B} - \frac{\partial\overline{B}}{\partial t}X\overline{D}]dv. \tag{5-10}$$

The last integral can be rewritten as follows (assuming μ and ε are scalars)

$$-\int_V [\frac{\partial\overline{D}}{\partial t}X\overline{B} - \frac{\partial\overline{B}}{\partial t}X\overline{D}]dv = -\int_V \mu\varepsilon[\frac{\partial\overline{E}}{\partial t}X\overline{H} + \overline{E}X\frac{\partial\overline{H}}{\partial t}]dv. \tag{5-11}$$

Note that (Hildebrand, p. 271)

$$\frac{d(\overline{a}X\overline{b})}{dt} = \overline{a}X\frac{d\overline{b}}{dt} + \frac{d\overline{a}}{dt}X\overline{b}. \tag{5-12}$$

Therefore

$$-\int_V \mu\varepsilon[\frac{\partial\overline{E}}{\partial t}X\overline{H} + \overline{E}X\frac{\partial\overline{H}}{\partial t}]dv = -\int_V \mu\varepsilon\frac{\partial}{\partial t}(\overline{E}X\overline{H})dv. \tag{5-13}$$

Therefore

$$\overline{F} = \int_V [\overline{E}(\nabla\cdot\overline{D}) - \overline{D}X(\overline{\nabla}X\overline{E})]dv + \int_V [\overline{H}(\nabla\cdot\overline{B}) - \overline{B}X(\nabla X\overline{H})]dv$$
$$- \int_V \mu\varepsilon\frac{\partial}{\partial t}(\overline{E}X\overline{H})dv. \tag{5-14}$$

The first two integrals in Eq. 5-14 can be expressed as surface integrals. The derivation of the surface integrals is lengthy and therefore not shown but results in the following expression for the force:

$$\overline{F} = \int_S [\varepsilon \overline{E}(\overline{E}\cdot\overline{n}) - \frac{\varepsilon \overline{E}^2 \overline{n}}{2}]ds + \int_S [\mu \overline{H}(\overline{H}\cdot\overline{n}) - \frac{\mu \overline{H}^2 \overline{n}}{2}]ds$$

$$- \int_V \mu\varepsilon \frac{\partial}{\partial t}(\overline{E} \times \overline{H})dv. \qquad (5\text{-}15)$$

where $\overline{n}$ is an outward unit vector normal to the surface, S. For static and slowly time varying fields the volume integral is small relative to the surface integrals. The remaining integrals yield the electrostrictive forces (first integral) and the magnetostrictive forces (second integral).

5.2 Force at a Dielectric Interface

Let us examine the first integral in Eq. 5-15 at the interface between two dielectrics ε_1 and ε_2.

Case 1. E normal to the dielectric interface

For the surfaces and fields and unit normal vectors shown in Fig. 5-1, the first integral in Eq. 5-15 reduces to

$$\overline{F}/A = (-\varepsilon_1 E_{n_1}^2 + \frac{1}{2}\varepsilon_1 E_{n_1}^2)\overline{a}_z + (\varepsilon_2 E_{n_2}^2 - \frac{1}{2}\varepsilon_2 E_{n_2}^2)\overline{a}_z \qquad (5\text{-}16)$$

or

$$\overline{f}_z = \overline{F}/A = (-\frac{1}{2}\varepsilon_1 E_{n_1}^2 + \frac{1}{2}\varepsilon_2 E_{n_2}^2)\overline{a}_z. \qquad (5\text{-}17)$$

But the boundary condition at the interface between the two materials is

$$D_{n_1} = D_{n_2} \qquad (5\text{-}18)$$

or

$$\varepsilon_1 E_{n_1} = \varepsilon_2 E_{n_2}$$

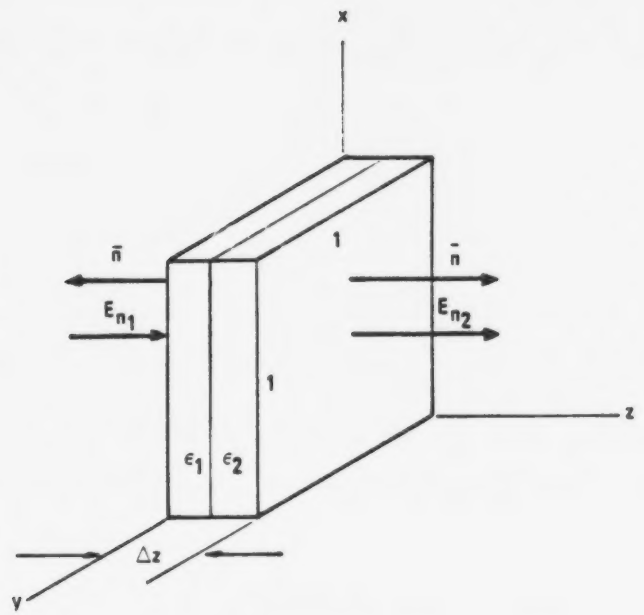

Figure 5-1. Field Vector Definitions for Fields Normal to a Dielectric Interface.

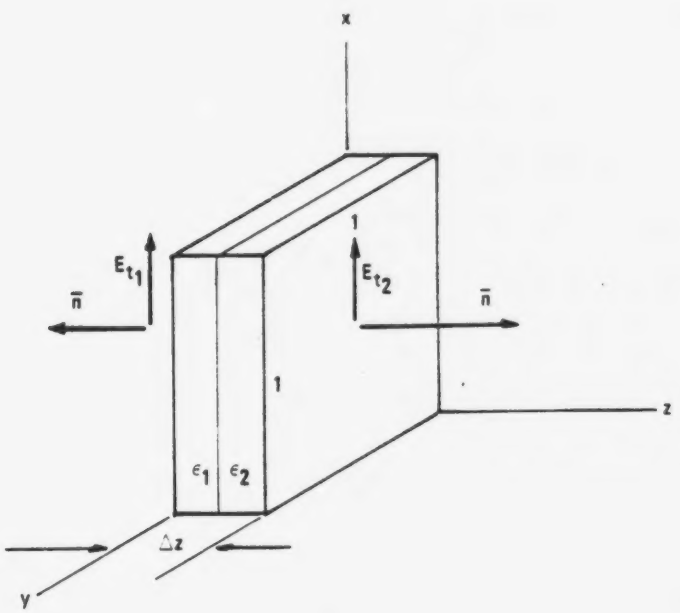

Figure 5-2. Field Vector Definitions for Fields Parallel to a a Dielectric Interface.

$$E_{n_2} = \frac{\varepsilon_1}{\varepsilon_2} E_{n_1} \quad . \tag{5-19}$$

Substituting Eq. 5-19 into 5-17 we get

$$\bar{f}_z = (-\frac{1}{2}\varepsilon_1 E_{n_1}^2 + \frac{1}{2}\varepsilon_2(\varepsilon_1/\varepsilon_2)^2 E_{n_1}^2)\bar{a}_z$$

or

$$\bar{f}_z = \frac{1}{2}\varepsilon_1(\frac{\varepsilon_1}{\varepsilon_2}-1)E_{n_1}^2\bar{a}_z. \tag{5-20}$$

It is interesting to note here that the direction of the force does not depend on the sign of the electric field and also that the force is always directed from the region with the higher dielectric constant to the region with the lower dielectric constant.

Case 2. E tangent to the dielectric interface

Again applying the first integral of Eq. 5-15 to the fields shown in Fig. 5-2 we get

$$\bar{F}/A = \frac{1}{2}\varepsilon_1 E_{t_1}^2 \bar{a}_z - \frac{1}{2}\varepsilon_2 E_{t_2}^2 \bar{a}_z \tag{5-21}$$

or

$$\bar{f}_z = \bar{F}/A = (\frac{1}{2}\varepsilon_1 E_{t_1}^2 - \frac{1}{2}\varepsilon_2 E_{t_2}^2)\bar{a}_z. \tag{5-22}$$

But the boundary condition at the interface between the two materials is

$$E_{t_1} = E_{t_2}. \tag{5-23}$$

Substituting into Eq. 5-22 we get

$$\bar{f}_z = (\frac{1}{2}\varepsilon_1 E_{t_1}^2 - \frac{1}{2}\varepsilon_2 E_{t_1}^2)\bar{a}_z$$

or

$$\bar{f}_z = \frac{1}{2}(\varepsilon_1-\varepsilon_2)E_{t_1}^2 \bar{a}_z. \tag{5-24}$$

As in Case 1 again the force is directed from the region with the higher permittivity to the region of the lower permittivity and does not depend on the sign of the tangential electric field.

Since the form of the magnetostrictive force integral in Eq. 5-15 is identical to the electrostrictive force integral, the above results would apply if μ and H are substituted for ε and E. From Eqs. 5-20 and 5-24 we can see that for nonmagnetic materials ($\mu = \mu_0$), the magnetostrictive forces are zero.

For the tissue models to be considered below, the exposure situation is an air/dielectric interface. The dielectric is almost totally composed of water and the exposure fields are of very low frequencies. For water the dielectric constant becomes very large at low frequencies. In terms of the fields on the surface of a water based dielectric this is equivalent to saying that the dielectric behaves like a conductor at low frequencies. The electric field will terminate normal to the dielectric surface and the internal field will be very small. If in Fig. 5-1 region one is assumed to be air and region two is assumed to be a high water content dielectric then at low frequencies Eq. 5-20 becomes

$$\bar{f}_z = -\frac{1}{2}\,\varepsilon_0 E_n {}_1\bar{a}_z \qquad (5\text{-}25)$$

or

$$\bar{f}_n = \frac{1}{2}\,\varepsilon_0 E_n {}_1\bar{a}_n. \qquad (5\text{-}26)$$

5.3 E Field Normal to the Surface of a Dielectric Ellipsoid in a Uniform Field

An ellipsoidal object with a permittivity ε_2 is surrounded by a medium

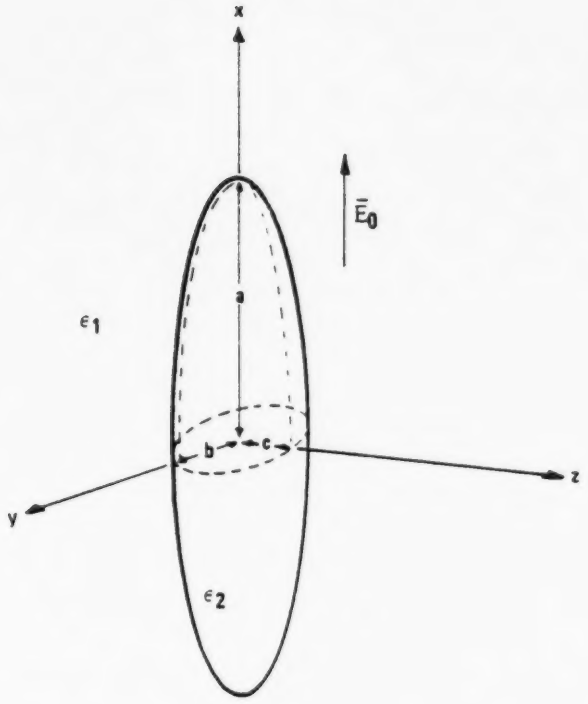

Figure 5-3. A Dielectric Ellipsoid in an Electric Field.

with permittivity ε_1 and immersed in a uniform field $E_0\,\bar{a}_x$ which is assumed parallel with the major axis of the ellipsoid as shown in Fig. 5-3. The equation of the ellipsoid is

$$\frac{x^2}{a^2} + \frac{y^2}{b^2} + \frac{z^2}{c^2} = 1 \tag{5-27}$$

where $a \geq b \geq c$.

The potential V_1 at any point outside the ellipsoid has been reported [Sillars, 1937] and is

$$V_1 = -xE_0 \left[1 - \frac{\varepsilon_2 - \varepsilon_1}{4\pi\varepsilon_1 + (\varepsilon_2 - \varepsilon_1) l_a} \int_{\alpha}^{\infty} \frac{d\alpha}{(a^2+\alpha)\beta}\right] \tag{5-28}$$

where

$$l_a \equiv \int_0^{\infty} \frac{d\alpha}{(a^2+\alpha)\beta} \tag{5-29}$$

and

$$\beta \equiv \sqrt{(a^2+\alpha)(b^2+\alpha)(c^2+\alpha)} \tag{5-30}$$

and where the integrals in Eq. 5-28 are elliptic of the second kind. For certain degenerate cases which will be considered below, namely the sphere and the prolate spheroid, the integrals can be solved analytically. For the general case, values for the integrals can be obtained from tables [Abramowitz et al, 1972]. The term α is a positive root of the equation

$$\frac{x^2}{a^2+\alpha} + \frac{y^2}{b^2+\alpha} + \frac{z^2}{c^2+\alpha} = 1 \tag{5-31}$$

which is the equation of a family of confocal ellipsoids if where $\alpha > -c^2$ where α is one of the three ellipsoidal coordinates.

The potential inside the ellipsoid is

$$V_2 = -xE_0 \frac{4\pi\varepsilon_1}{4\pi\varepsilon_1 + (\varepsilon_2 - \varepsilon_1) l_a} . \tag{5-32}$$

This equation follows from Eq. 5-28 in which α is set equal to zero. The integral is then replaced by l_a in Eq. 5-29. Finally applying the boundary conditions that the potential is continuous from just inside the surface of the ellipsoid to just outside the surface, we arrive at Eq. 5-32.

The exterior electric field normal to the surface of the ellipsoid is

$$E_{n_1} = -\frac{\partial V}{\partial n}_1 . \tag{5-33}$$

But

$$D_{n_1} - D_{n_2} = \rho_s = 0. \tag{5-34}$$

Therefore

$$\varepsilon_1 E_{n_1} = \varepsilon_2 E_{n_2}$$

or

$$E_{n_1} = \frac{\varepsilon_2}{\varepsilon_1} E_{n_2}. \tag{5-35}$$

But

$$E_{n_2} = \bar{E}_2 \cdot \bar{n} = -\nabla V_2 \cdot \bar{n}$$

$$= -\left(\frac{\partial V}{\partial x}_2 \bar{a}_x + \frac{\partial V}{\partial y}_2 \bar{a}_y + \frac{\partial V}{\partial z}_2 \bar{a}_z\right) \cdot \bar{n}. \tag{5-36}$$

Since V_2 has only dependence on x, by Eq. 5-32

$$\frac{\partial V}{\partial y}_2 = 0, \quad \frac{\partial V}{\partial z}_2 = 0. \tag{5-37}$$

Therefore, substituting Eq. 5-36 into Eq. 5-35,

$$E_{n_1} = -\frac{\varepsilon_2}{\varepsilon_1} \frac{\partial V}{\partial x}_2 \bar{a}_x \cdot \bar{n} \tag{5-38}$$

where the term $\bar{a}_x \cdot \bar{n}$ is the direction cosine [Hildebrand , 1962, pp. 264, 288]. Taking the derivative of V_2 with respect to x we get

$$\frac{\partial V_2}{\partial x} = -E_0 \frac{4\pi\varepsilon_1}{4\pi\varepsilon_1 + (\varepsilon_2 - \varepsilon_1) l_a} \tag{5-39}$$

which together with Eq. 5-37 shows that the electric field inside the dielectric ellipsoid is uniform and in the x direction for a dielectric ellipsoid immersed in a uniform field parallel to its major axis. To compute the direction cosine, the unit normal vector must first be found.

If

$$f = \frac{x^2}{a^2} + \frac{y^2}{b^2} + \frac{z^2}{c^2} - 1 = 0 \tag{5-40}$$

then

$$\nabla f = \frac{2x}{a^2} \bar{a}_x + \frac{2y}{b^2} \bar{a}_y + \frac{2z}{c^2} \bar{a}_z \tag{5-41}$$

$$n \equiv \frac{\nabla f}{|\nabla f|} = \frac{\frac{2x}{a^2} a_x + \frac{2y}{b^2} a_y + \frac{2z}{c^2} a_z}{\sqrt{\frac{4x^2}{a^4} + \frac{4y^2}{b^4} + \frac{4z^2}{c^4}}} . \tag{5-42}$$

Letting

$$p \equiv 1/\sqrt{\frac{x^2}{a^4} + \frac{y^2}{b^4} + \frac{z^2}{c^4}} \tag{5-43}$$

we get

$$\bar{n} = \frac{xp}{a^2} \bar{a}_x + \frac{yp}{b^2} \bar{a}_y + \frac{zp}{c^2} \bar{a}_z . \tag{5-44}$$

The direction cosine therefore is

$$\bar{a}_x \cdot \bar{n} = \frac{xp}{a^2} \tag{5-45}$$

and with Eq. 5-38 results in

$$E_{n_1} = -\frac{\varepsilon_2}{\varepsilon_1}\left[-E_0 4\pi\varepsilon_1 \cdot \frac{1}{4\pi\varepsilon_1 + (\varepsilon_2 - \varepsilon_1) l_a}\right]\frac{xp}{a^2} \tag{5-46}$$

or rearranging terms

$$E_{n_1} = \frac{E_0}{\left[\frac{\varepsilon_1}{\varepsilon_2} + \frac{(\varepsilon_2 - \varepsilon_1) l_a}{4\pi}\right] \sqrt{1 + \frac{a^4}{x^2}\left(\frac{y^2}{b^4} + \frac{z^2}{c^4}\right)}} . \tag{5-47}$$

This is the general expression for the electric field in medium one normal to the surface of a dielectric ellipsoid immersed in a uniform field. In the next two sections two special cases will be considered: a sphere and a prolate spheroid.

5.3.1 Special Case: Spheroid

Applying Eq. 5-47 to the sphere and prolate spheroid is accomplished by restricting the allowed values of the major and minor axes of the ellipsoid and evaluation of the term "l_a". For the sphere

$$a = b = c. \tag{5-48}$$

Substituting "a" for "b" and "c" in Eq. 5-47 we get

$$E_{n1} = \frac{E_0}{\left[\frac{\varepsilon_1}{\varepsilon_2} + \left(\frac{\varepsilon_2-\varepsilon_1}{\varepsilon_2}\right)\frac{l_a}{4\pi}\right] \sqrt{(x^2+y^2+z^2)/x^2}} . \tag{5-49}$$

But for a sphere

$$x^2 + y^2 + z^2 = a^2. \tag{5-50}$$

Substituting in Eq. 5-49 we get

$$E_{n1} = \frac{E_0\, x}{\left[\frac{\varepsilon_1}{\varepsilon_2} + \left(\frac{\varepsilon_2-\varepsilon_1}{\varepsilon_2}\right)\frac{l_a}{4\pi}\right] a} . \tag{5-51}$$

If θ is the angle between the radius vector and the x axis, then on the surface of the sphere

$$x = a \cos \theta . \tag{5-52}$$

Substituting into Eq. 5-51 we get

$$E_{n1} = \frac{E_0 \cos \theta}{\left[\frac{\varepsilon_1}{\varepsilon_2} + \left(\frac{\varepsilon_2-\varepsilon_1}{\varepsilon_2}\right)\frac{l_a}{4\pi}\right]} . \tag{5-53}$$

Turning now to the evaluation of l_a for the sphere

$$l_a = \int_0^\infty \frac{d\alpha}{(a^2+\alpha)\beta} \tag{5-54}$$

where

$$\beta \equiv \frac{\sqrt{(a^2+\alpha)(b^2+\alpha)(c^2+\alpha)}}{2\pi abc}. \tag{5-55}$$

Now substituting

$$a = b = c \tag{5-56}$$

into Eq. 5-55 we get

$$\beta = \frac{(a^2+\alpha)^{3/2}}{2\pi a^3} . \tag{5-57}$$

The term, l_a, is therefore

$$l_a = \int_0^\infty \frac{2\pi a^3 d\alpha}{(a^2+\alpha)^{5/2}} = -\frac{2}{3}(a^2+\alpha)^{-3/2} 2\pi a^3 \Big|_0^\infty = \frac{4\pi}{3} . \tag{5-58}$$

Substituting this value of l_a into Eq. 5-53 yields

$$E_{n_1} = \frac{3\varepsilon_2 E_0 \cos\theta}{2\varepsilon_1 + \varepsilon_2} . \tag{5-59}$$

This is the expression for the electric field normal to the surface of a dielectric sphere immersed in a uniform field, E_0. If the numerator and denominator of Eq. 5-59 are divided by ε_2, we get

$$E_{n_1} = \frac{3E_0 \cos\theta}{\frac{2\varepsilon_1}{\varepsilon_2} + 1} . \tag{5-60}$$

For a conductor $\varepsilon_2 \to \infty$, therefore

$$E_{n_1} \to 3E_0 \cos\theta \tag{5-61}$$

which is the familiar expression for the field at the surface of a conducting sphere placed in a uniform field, E_0.

5.3.2 Special Case: Prolate Spheroid

For the prolate spheroid

$$b = c \tag{5-62}$$

in Fig. 5-3 and Eq. 5-47 becomes

$$E_{n1} = \frac{E_0}{\left[\frac{\varepsilon_1}{\varepsilon_2} + \left(\frac{\varepsilon_2-\varepsilon_1}{\varepsilon_2}\right)\frac{l_a}{4\pi}\right]\sqrt{1+\frac{a^4}{b^4}\left(\frac{y^2+z^2}{x^2}\right)}}. \tag{5-63}$$

The term l_a must now be evaluated. Substituting Eq. 5-62 into Eq. 5-30 we get

$$\beta = \frac{\sqrt{(a^2+\alpha)(b^2+\alpha)^2}}{2\pi ab^2}. \tag{5-64}$$

Therefore l_a is

$$l_a = 2\pi ab^2 \int_{\alpha=0}^{\infty} \frac{d\alpha}{(a^2+\alpha)^{3/2}(b^2+\alpha)}. \tag{5-65}$$

Let us make the following substitutions to simplify the integral:

$$y = b^2 + \alpha \tag{5-66}$$

$$dy = d\alpha \tag{5-67}$$

$$\alpha = y-b^2 \tag{5-68}$$

$$a^2 + \alpha = a^2 + y - b^2 \tag{5-69}$$

$$= y + a^2 - b^2. \tag{5-70}$$

Let

$$k^2 = a^2 - b^2 \tag{5-71}$$

then

$$a^2 + \alpha = y + k^2. \tag{5-72}$$

Substituting into Eq. 5-65 we get

$$l_a = 2\pi ab^2 \int_{b^2}^{\infty} \frac{dy}{(y+k^2)^{3/2}y}. \tag{5-73}$$

This expression is still not in a form found in a table of integrals. We therefore try the substitution

$$y = z^2 \tag{5-74}$$

$$dy = 2z\,dz. \tag{5-75}$$

Then

$$l_a = 2\pi ab^2 \int_b^\infty \frac{2z\,dz}{(z^2+k^2)^{3/2}z^2} \tag{5-76}$$

$$= 4\pi ab^2 \int_b^\infty \frac{dz}{z\sqrt{(z^2+k^2)^3}}. \tag{5-77}$$

From the table of integrals [Weast et al, 1964 p. A-132]

$$l_a = 4\pi ab^2\left[\frac{1}{k^2\sqrt{z^2+k^2}} - \frac{1}{k^3}\ln\left(\frac{k+\sqrt{z^2+k^2}}{z}\right)\right]\Bigg|_b^\infty. \tag{5-78}$$

Evaluating Eq. 5-78 we get

$$l_a = 4\pi ab^2\left[(0) - \left\{\frac{1}{k^2\sqrt{b^2+k^2}} - \frac{1}{k^3}\ln\left(\frac{k+\sqrt{b^2+k^2}}{b}\right)\right\}\right]. \tag{5-79}$$

But

$$\sqrt{b^2+k^2} = a. \tag{5-80}$$

Therefore

$$l_a = -4\pi ab^2\left[\frac{1}{(a^2-b^2)a} - \frac{1}{(a^2-b^2)\sqrt{a^2-b^2}}\ln\left(\frac{\sqrt{a^2-b^2}+a}{b}\right)\right]. \tag{5-81}$$

Let

$$e = \text{eccentricity} = \sqrt{1-b^2/a^2} \tag{5-82}$$

or

$$e^2 = \frac{a^2-b^2}{a^2}. \tag{5-83}$$

Now

$$l_a = -4\pi ab^2\left[\frac{1}{ae^2a^2} - \frac{1}{e^3a^3}\ln\left(\frac{ea+a}{b}\right)\right] \tag{5-84}$$

$$= 4\pi\left[-\frac{b^2}{e^2a^2} + \frac{b^2}{a^2e^3}\ln\left(\frac{e+1}{b/a}\right)\right]. \tag{5-85}$$

This expression for l_a can be expressed in a form containing only the term,

e, the eccentricity:

$$-\frac{b^2}{e^2a^2} = \frac{a^2-b^2-a^2}{a^2-b^2} = 1 - \frac{a^2}{a^2-b^2} = 1 - \frac{1}{(a^2-b^2)/a^2} \tag{5-86}$$

$$= 1 - \frac{1}{e^2} \tag{5-87}$$

Substituting into Eq. 5-85 we get

$$l_a = 4\pi[1 - \frac{1}{e^2} + \frac{b^2}{a^2e^3} \ln \frac{(e+1)}{b/a}]. \tag{5-88}$$

Note that from Eq. 5-83

$$b/a = \sqrt{1-e^2} = \sqrt{(1+e)(1-e)}. \tag{5-89}$$

Then

$$l_a = 4\pi[1 - \frac{1}{e^2} + \frac{b^2}{a^2e^3} \ln \frac{(1+e)}{(1+e)^{1/2}(1-e)^{1/2}}] \tag{5-90}$$

$$l_a = 4\pi[1 - \frac{1}{e^2} + \frac{b^2}{2a^2e^3} \ln \frac{(1+e)}{1-e}]. \tag{5-91}$$

Using Eq. 5-89 in Eq. 5-91 we get

$$l_a = 4\pi[-(\frac{1}{e^2}-1) + \frac{(1-e^2)}{2e^3} \ln \frac{(1+e)}{1-e}] \tag{5-92}$$

$$= 4\pi[-(\frac{1}{e^2}-1) + \frac{1}{2e}(\frac{1}{e^2}-1)\ln \frac{(1+e)}{1-e}] \tag{5-93}$$

$$= 4\pi(\frac{1}{e^2}-1)[\frac{1}{2e} \ln \frac{(1+e)}{1-e}-1]. \tag{5-94}$$

In summary, the electric field normal to the surface of a dielectric prolate spheroid with permittivity ε_2 surrounded by a medium with permittivity ε_1 and immersed in a uniform electric field E_0 parallel to the major axis of the object is from Eq. 5-63

$$E_{n1} = \frac{E_0}{[\frac{\varepsilon_1}{\varepsilon_2} + (\frac{\varepsilon_2-\varepsilon_1}{\varepsilon_2})\frac{l_a}{4\pi}] \sqrt{1+\frac{a^4}{b^4}(\frac{y^2+z^2}{x^2})}} \tag{5-95}$$

where

$$l_a = 4\pi(\frac{1}{e^2}-1)[\frac{1}{2e} \ln \frac{(1+e)}{1-e}-1] \tag{5-96}$$

and e, the eccentricity, is given by Eq. 5-82.

5.4 Derivation of the Vertical Force on a Half-Prolate Spheroid with its Base on a Ground Plane

In section 5.2 the force per unit area acting on the surface of dielectric with a large permittivity was derived (see Eq. 5-26). In the previous section the normal electric field at the surface of a prolate spheroid was derived. In combining these two expressions and taking the component of the force in the x direction, the total vertical force acting to stretch the half-prolate spheroid can be computed. The total force in the x direction is

$$F_x = \int_S (f_n \cos\theta') d\sigma \tag{5-97}$$

where $\cos\theta'$ is the direction cosine for the x axis, $d\sigma$ is the differential element of surface area and f_n is given by Eq. 5-26. The term $d\sigma$ can be replaced by an element of area which is the projection of $d\sigma$ on the y-z plane by the expression

$$d\sigma = \frac{d_y d_z}{\cos\theta'}. \tag{5-98}$$

The vertical force is then

$$F_x = \int_A f_n d_y d_z \tag{5-99}$$

where the integration is performed over the projected area, A, in the yz plane [Hildebrand, 1962, p. 289]. Using Eqs. 5-95 and letting ε_2, the permittivity, become very large as it does at low frequencies we get

$$E_{n1} = \frac{E_0}{\frac{1}{4\pi}\frac{a}{} \sqrt{1 + \frac{a^4}{b^4}\left(\frac{y^2+z^2}{x^2}\right)}}. \tag{5-100}$$

Substituting this expression into Eq. 5-26 we obtain

$$f_n = \frac{8\pi^2 E_0^2 \varepsilon_0}{l_a^2 \left[1+\frac{a^4}{b^4}\left(\frac{y^2+z^2}{x^2}\right)\right]}. \tag{5-101}$$

Let

$$P_{max} = \frac{8\pi^2 E_0^2 \varepsilon_0}{l_a^2},$$

then

$$f_n = \frac{P_{max}}{\left[1 + \frac{a^4}{b^4}\left(\frac{y^2+z^2}{x^2}\right)\right]}. \tag{5-102}$$

F_x is therefore

$$F_x = \int_A \frac{P_{max}}{\left[1 + \frac{a^4}{b^4}\left(\frac{y^2+z^2}{x^2}\right)\right]} dy dz. \tag{5-103}$$

In order to evaluate the integral, x must be expressed in terms of y and z. This is found from the equation of a prolate spheroid:

$$\frac{x^2}{a^2} + \frac{y^2}{b^2} + \frac{z^2}{b^2} = 1. \tag{5-104}$$

Solving for x we obtain

$$x = a\sqrt{1 - \frac{y^2+z^2}{b^2}}. \tag{5-105}$$

Substituting into Eq. 5-103 we obtain after some manipulation

$$F_x = \int_A \frac{P_{max}}{1 + \frac{a^2}{b^2}\left(\frac{y^2+z^2}{b^2-(y^2+z^2)}\right)} dy dz. \tag{5-106}$$

Switching to polar coordinates will simplify the integral if we let

$$r^2 = y^2 + z^2 \tag{5-107}$$

$$r dr d\theta = dy dz$$

so that

$$F_x = 4 \int_{r=0}^{b} \int_{\theta=0}^{\pi/2} \frac{P_{max}}{1+\frac{a^2}{b^2}\left(\frac{r^2}{b^2-r^2}\right)} r d\theta dr \tag{5-108}$$

$$= \frac{-4P_{max}b^2}{a^2-b^2} \iint \frac{r^3-b^2r}{r^2+\frac{b^4}{a^2-b^2}} \, d\theta dr. \tag{5-109}$$

Let

$$d = \frac{b^4}{a^2-b^2} \tag{5-110}$$

then

$$F_x = \frac{-4\pi P_{max}b^2}{2(a^2-b^2)} \int_0^b [r - \frac{(b^2+d)r}{r^2+d}]dr \tag{5-111}$$

$$= \frac{2\pi b^2 P_{max}}{(a^2-b^2)} [\frac{a^2b^2}{a^2-b^2} \ln \frac{a}{b} - \frac{b^2}{2}]. \tag{5-112}$$

Now let

$$e^2 = \frac{a^2-b^2}{a^2} \tag{5-113}$$

as we did in Eq. 5-83.

Then

$$F_x = \frac{2\pi b^2 P_{max}}{e^2} [\frac{b^2}{a^2-b^2} \ln \frac{a}{b} - \frac{b^2}{2a^2}]. \tag{5-114}$$

But

$$\frac{b^2}{a^2} = 1 - e^2; \tag{5-115}$$

therefore

$$F_x = \frac{2\pi b^2 P_{max}}{e^2} [\frac{b^2}{a^2-b^2} \ln \frac{a}{b} - (\frac{1-e^2}{2})] \tag{5-116}$$

$$F_x = \frac{\pi b^2 P_{max}}{e^2} [\frac{b^2}{a^2-b^2} \ln \frac{1}{(1-e^2)} - (1-e^2)]. \tag{5-117}$$

But

$$\frac{b^2}{a^2-b^2} = \frac{1}{e^2} - 1; \tag{5-118}$$

therefore

$$F_x = \frac{\pi b^2 P_{max}}{e^2} [(\frac{1}{e^2} -1) \ln \frac{1}{(1-e^2)} - (1-e^2)] \tag{5-119}$$

$$= \frac{\pi b^2 p_{max}}{e^2}\left[\left(1-\frac{1}{e^2}\right)\ln(1-e^2) + (e^2-1)\right] \qquad (5\text{-}120)$$

$$F_x = \frac{\pi b^2 p_{max}}{e^2}(e^2-1)\left[\frac{1}{e^2}\ln(1-e^2) + 1\right]. \qquad (5\text{-}121)$$

Equation 5-121 is an exact analytical expression for the total vertical (long-axis direction) force acting on a high-permittivity-valued dielectric half-prolate spheroid. It will be used in the following section to compute an estimate of the displacement or strain resulting from this force.

5.5 Calculation of Displacement and Expected Receiver Signal

5.5.1 Mechanics of Elastic Bodies

The approach taken so far has been to choose a geometrical shape for which an exact solution to the force acting to elongate an object could be calculated. The force you will recall is due to the immersion of the dielectric object in a uniform electric field. The mechanics and composition of the dielectric object must now be considered. The half prolate spheroid will be constructed of a material with a high water content and with a Young's modulus [Sears, 1958] such that the material models biological tissue in these two respects. The material must be homogeneous and isotropic and for the small forces to be considered here it will also obey Hooke's law, that is

$$\frac{\Delta F}{A} = E\,\frac{\Delta l}{L}, \qquad (5\text{-}122)$$

where the term E is Young's modulus. In words this equation says that stress is proportional to strain. Another quantity used in materials science is the Poisson's ratio, μ, [Sears, 1958] which is the ratio of transverse to longitudinal strain. For a prismatic bar with a square cross-section the

change in lateral width (contraction) due to an axial elongation is given by

$$\Delta w = w\mu\varepsilon \tag{5-123}$$

where w is the initial width and ε, the strain, is the ratio of Δl divided by L. For all materials the Poisson's ratio ranges between zero and one-half with the value of one-half implying no change in volume under an axial compression or elongation. The value of μ was determined experimentally for the material used in the experiments to be described below.

Equation 5-122 is adequate to describe the elongation (or contraction) that occurs under static or quasistatic conditions. However a solid dielectric object is a continuous system, that is a system of an infinite number of mass particles interconnected in a lattice of springlike molecular bonds. Therefore as in all continuous mechanical systems, an infinite number of natural resonance frequencies exist for the object. If the object is acted upon by a force whose frequency is well below the first resonance frequency, the resulting elongation (or vibration amplitude) can be described by Eq. 5-122. However as the frequency of the forcing function is raised, the object will exhibit a series of resonant frequencies at which the vibration amplitude may be larger than for the static case and be dependent on the amplitude of the forcing function and the damping constant of the material. As the frequency of the forcing function is increased still further, the vibration amplitude will approach zero as the inertial forces become overwhelming.

In the sections to follow an approximate value of the vibration amplitude will be calculated and compared to experimental data for the case of the forcing function frequency well below resonance.

5.5.2 Approximation of Half-Prolate Spheroid by a Prismatic Bar

Because of the mathematical difficulty in computing the exact displace-

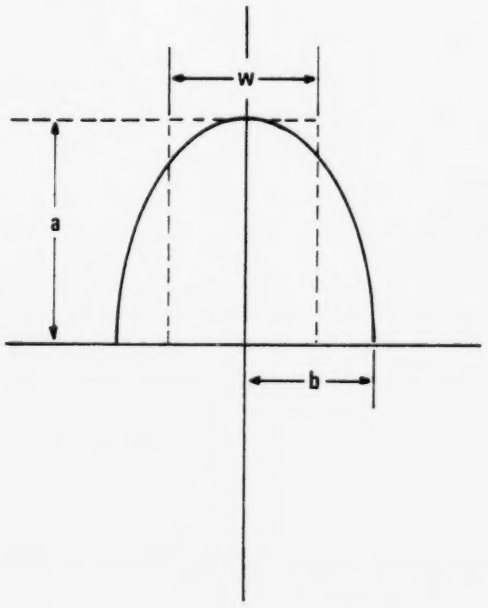

Figure 5-4. Approximation of a Half-Prolate Spheroid by a Prismatic Bar.

ment of a half prolate spheroid Agar gel solid when acted upon by a non-uniform force over its entire surface area, an approximate value of the expected deformation was found. The half prolate spheroid was assumed to be replaceable by a prismatic bar of square cross-section having the same height as the half-prolate spheroid and sides which allow the prismatic bar to have the same volume as the half-prolate spheroid as shown in Fig. 5-4. Since the volume of a half-prolate spheroid is

$$V_{ps} = \frac{2}{3}\pi ab^2 \tag{5-124}$$

then if the volumes of the two shapes are equal we have

$$a\,w^2 = \frac{2}{3}\pi ab^2 \tag{5-125}$$

or

$$w = b\sqrt{2\pi/3} = 1.447b. \tag{5-126}$$

It will be assumed that the vertical force computed in section 5.4 acts on the top surface of the bar causing an elongation in the vertical direction and a contraction in the width.

When the half-prolate spheroid sample is placed in the exposure cell, the X-band signal will be scattered back to the receiver primarily by the front face of the object. Therefore the measured deformation of the test object will be half the contraction of the side of the object while the height is elongated under the action of the vertical stress. Expressing the change in position of the front face in terms of the total vertical force we first get

$$\Delta t = \frac{\Delta w}{2} = \frac{w\mu\ \Delta x}{2a}. \tag{5-127}$$

But, using Eq. 5-122,

$$\Delta x = \frac{F_x a}{w^2 E} \tag{5-128}$$

where F_x is given by Eq. 5-121. Substituting Eq. 5-128 into Eq. 5-127 yields

$$\Delta t = \frac{\mu F_x}{2wE}. \qquad (5\text{-}129)$$

In order to evaluate this equation, the values of E and μ must first be determined.

5.5.3 Measurement of Young's Modulus and Poisson's Ratio for Agar Gels

Agar gels were chosen to model tissue primarily because it was observed to have about the same elasticity as biological tissue, [Lin, 1976] particularly brain tissue. Two kinds of gels are readily available in the laboratory, agar and gelatin. Although the elasticity of gelatin gels is suitable for this application, the fact that gelatin becomes liquid aboves 28 °C is a serious disadvantage. Agar, a carbohydrate extracted from certain marine algae, remains in the solid state up to a temperature of about 40 °C. It was therefore preferred over gelatin and used exclusively.

Gel samples were prepared by mixing the desired proportions (by weight) of agar and deionized water in a beaker and bringing the solution to a boil. The beaker was then placed on the balance and weighed and enough water was added to replace that lost in the boiling process. The beaker was then immediately covered with aluminum foil to prevent further evaporation and then it was set aside for a few hours to allow the gel to solidify at room temperature. This procedure ensured that the gel was at the desired concentration even after boiling.

Young's modulus of the agar gels was measured for a series of concentrations over the 0.6% to 1.0% range through measurement of the terms in the following equation

$$E = \frac{\Delta F / \Delta l}{A \quad L}. \qquad (5\text{-}130)$$

The agar gel was sliced into approximately 1.5 cm cubes, its dimensions were measured and then it was placed on the apparatus shown in Fig. 5-5. A small

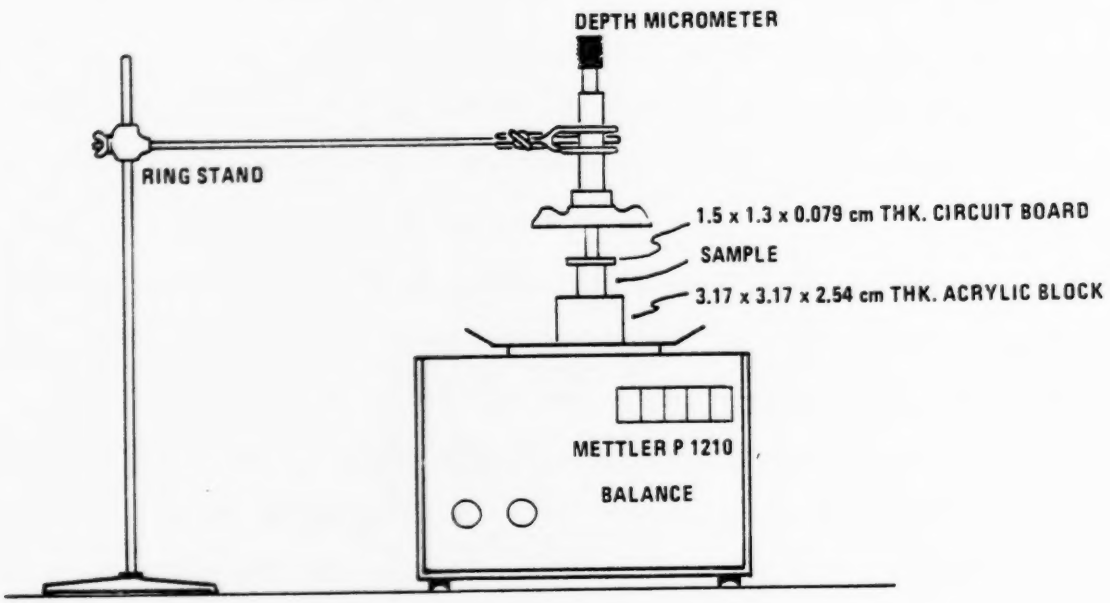

Figure 5-5 Apparatus for Measurement of Young's Modulus.

Table 5-1

Experimental Data for the Determination of Young's Modulus of Agar Gels

Concentration (%)	Trial	Area (mmxmm)	Initial Length (mm)	ΔL (mm)	Force (nt)	Young's Modulus (E) (10^3nt/m^2)
0.6	1	14x14	13.0	0.820	0.0784	6.34
0.6	2	15x11.5	13.5	1.024	0.0784	6.00
0.6	3	13.5x13	13.0	0.770	0.0784	7.55
0.6	4	12.5x16	14.0	0.922	0.0784	5.96
0.6	5	15x12	13.0	0.897	0.0784	6.32
		Young's Modulus (E, 10^3nt/m^2):		mean = 6.43, σ = 0.58		
0.7	1	12x13.5	14.0	0.843	0.0833	8.57
0.7	2	11x12	11.2	0.922	0.0784	7.19
0.7	3	14x12	12.2	1.140	0.0800	5.09
0.7	4	13x11.5	11.5	0.836	0.0801	7.38
0.7	5	11x13	10.0	0.719	0.0784	7.59
		Young's Modulus (E, 10^3nt/m^2):		mean = 7.16, σ = 1.14		
0.8	1	11.5x14	14.0	0.790	0.0981	10.80
0.8	2	14x14	10.0	0.561	0.0981	8.91
0.8	3	13x11.5	11.5	0.739	0.0981	10.20
0.8	4	12x11	11.0	0.663	0.0981	12.32
0.8	5	12x10.5	12.0	0.739	0.0981	12.64
		Young's Modulus (E, 10^3nt/m^2):		mean = 10.97, σ = 1.38		
0.9	1	14.5x14	15.0	0.912	0.1180	9.57
0.9	2	14x11	12.0	1.013	0.1180	9.08
0.9	3	15x12.5	12.5	0.638	0.0980	10.30
0.9	4	13x13	13.5	0.714	0.0980	10.98
0.9	5	12x10	11.0	0.693	0.0784	10.36
		Young's Modulus (E, 10^3nt/m^2):		mean = 10.10, σ = 0.66		
1.0	1	12.5x11.5	10.0	0.582	0.1180	14.12
1.0	2	11x10	12.0	0.785	0.1180	16.42
1.0	3	16x11	13.0	0.683	0.1180	12.76
1.0	4	11x11	12.5	0.787	0.1220	16.03
1.0	5	10.5x13.5	11.0	0.658	0.1180	13.92
		Young's Modulus (E, 10^3nt/m^2):		mean = 14.65, σ = 1.37		

Table 5-2

Experimental Data for the Determination of Poisson's Ratio of 0.6%c Agar Gel

Trial	Area (mmxmm)	w_1 (mm)	w_2 (mm)	l_1 (mm)	l_2 (mm)	Poisson's Ratio μ
1	12x12	12.01	12.52	9.40	8.26	.35
2	12.3x9.5	12.32	13.00	10.54	9.02	.38
3	11.5x11.5	11.51	11.94	9.19	8.28	.38

Poisson's Ratio: mean = 0.37, σ = 0.014

piece of circuit board was placed on top of the gel sample to distribute the force to be applied over the entire top surface of the sample. The balance was then tared and the depth micrometer adjusted to just touch the top of the circuit board. The micrometer reading was then noted. The micrometer adjusting screw was then turned to apply a compressive force on the sample of about 8 to 12 grams and the micrometer dial was again read and recorded as well as the balance reading. In measuring the compression of the sample, allowance had to be made for the travel of the balance pan as weight or force was applied. Prior to any sample measurements, therefore, the pan travel versus weight was measured. The depth micrometer was used to measure pan travel, while the force was measured with the balance itself. The pan travel was found to be 2.09 mils per gram. The measured data for all the samples is presented in Table 5-1. The data is plotted in Fig. 5-6 along with the regression line.

To obtain maximum deflection of a sample when placed in the exposure cell and exposed to an electric field, one would want to use a material with as small a Young's modulus as possible. Below an agar concentration of about 0.55%, the agar did not gel properly, therefore a 0.6% concentration was chosen for all deflection measurements described below. The Poisson's ratio is also needed for the gel sample and it was determined by measuring the parameters in the defining equation

$$\mu = \frac{(w_2 - w_1)}{w_1} \Big/ \frac{(l_1 - l_2)}{l_1} \qquad (5\text{-}131)$$

where the subscripts one and two refer to the initial and final lengths respectively. The measured data for 0.6% c agar is given in Table 5-2. The mean value of μ was 0.37 with a standard deviation of $\pm$ 0.014.

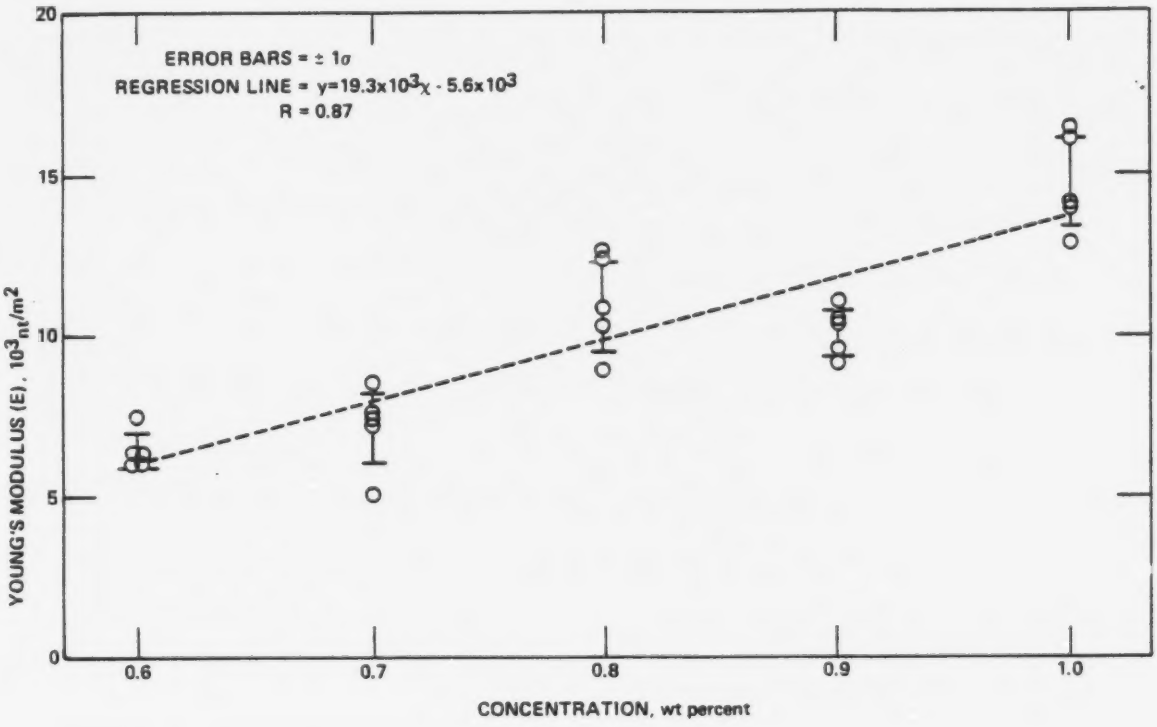

Figure 5-6. Young's Modulus Versus Concentration for Agar Gels.

5.5.4 Calculation of Displacement

Having dispensed with all the prelminary derivations, the displacment of the prismatic bar can now be calculated. Referring to Fig. 5-4 for a half-prolate spheroid with dimensions

$$a = 2.0 \text{ mm}$$

$$b = 1.00 \text{ mm}$$

the prismatic bar approximation will have a width (see Eq. 5-126) of

$$w = 1.447b = 1.447 \times 10^{-3} m.$$

The motion of the front face of the prismatic bar is by Eq. 5-128

$$\Delta t = \frac{\mu F_x}{2wE} \tag{5-132}$$

where E is 6.43×10^3 nt/m^2 for 0.6% c Agar gel as determined in the previous section. Poisson's ratio was measured as 0.37 for 0.6% c Agar gel. From Eq. 5-121

$$F_x = \frac{\pi b^2 p_{max}(e^2-1)}{e^2}\left[\frac{1}{e^2}\ln(1-e^2)+1\right] \tag{5-133}$$

where

$$P_{max} = \frac{8\pi^2 E_o^2 \varepsilon_o}{l_a^2} \tag{5-134}$$

and from Eq. 5-94

$$l_a = 4\pi\left(\frac{1}{e^2}-1\right)\left(\frac{1}{2e}\ln\left(\frac{1+e}{1-e}\right)-1\right) \tag{5-135}$$

where

$$e = \sqrt{1-(b/a)^2} = 0.866$$

$$e^2 = 0.75$$

and therefore

$$l_a = 2.179.$$

The separation between the center strip of the exposure cell and the ground plane (the waveguide broad wall) is 0.6 cm. The exposure cell center conductor was energized with the voltage

$$V_m = 50 \cos \omega_m t \text{ volts}$$

which creates an electric field in the exposure cell of

$$E_0 = \frac{50 \cos \omega_m t}{.006 \text{ m}} = 8{,}333 \cos \omega_m t \text{ V/m.} \qquad (5\text{-}136)$$

Using Eq. 5-134 P_{max} is

$$P_{max} = \frac{8\pi^2(8.33\times10^3)^2 8.85\times10^{-12}}{(2.179)^2} = 0.0102 \text{ nt/m}^2.$$

F_x is therefore from Eq. 5-133

$$F_x = \frac{\pi(1.00\times10^{-3})^2 \cdot 0.0102 \cdot (-0.25)[-0.8484]}{0.75}$$

$$= 0.906\times10^{-8} \text{nt.}$$

Substituting in the formula for Δt (Eq. 5-129) we get

$$\Delta t = \frac{0.37(0.906\times10^{-8})}{2(1.447\times10^{-3})(6.43\times10^3)} = 0.180 \text{ nm.}$$

If this motion is written as a function of time we get

$$\Delta t(t) = \Delta t \sin^2 \omega_m t. \qquad (5\text{-}137)$$

This equation can be expressed as

$$\Delta t(t) = \frac{\Delta t}{2} - \frac{\Delta t}{2} \cos 2\omega_m t. \qquad (5\text{-}138)$$

Therefore the amplitude of the AC component of the deflection is

$$\Delta t_{AC}(t) = \frac{\Delta t}{2} \cos 2\omega_m t \ . \qquad (5\text{-}139)$$

For the sample under discussion

$$\Delta t_{AC}(t) = 0.090 \cos 2\omega_m t \text{ nm.}$$

Equation 5-138 shows that if a dielectric object is placed in an alternating electric field, the object experiences a constant strain as well as an alternating strain at twice the frequency of the applied field.

For a given exposure cell plate separation, an object whose height is one third or less of this separation is generally considered to have little effect on the exposure field when such an object is placed in the cell. The half-prolate spheroid sample in the calculation just preceeding had a height, a, equal to 2 mm and therefore satisfies the one third height criterion.

Notwithstanding this guideline, some targets larger than one third the plate separation were also used for reasons that will be explained later. For an object larger than one-third the plate separation, the presence of the object causes significant charge redistribution on the plate above the sample and this perturbation must at least be approximated. The electric field on the surface of these larger half-prolate spheroid targets was assumed to have the same distribution as calculated in Section 5.3.2. In addition, an approximate effective exposure field was calculated using an effective plate separation equal to the actual plate separation minus two-thirds the height of the half-prolate spheroid. For example, for a half-prolate spheroid with dimension a equal to 5 mm, the effective plate separation would be 6 mm (the actual plate separation) minus 3.33 mm (two-thirds of a) equals 2.67 mm. This serves to increase the effective exposure field to more realistically characterize the exposure conditions for samples larger than one-third the plate separation.

In addition to the 2 mm base half-prolate spheroid considered in this section, calculations for half-prolate spheroid samples with minor and major axes of 1.75 mm and 3.5 mm, and 2.5 mm and 5 mm, respectively, were also performed and these results are contained in Table 5-3.

5.5.5 Calculation of the Expected Receiver Signal

In Chapter two the single sideband to carrier ratio (SSBCR) was derived

for a linearly vibrating rigid body. The front surface of the prismatic bar is vibrating in this way when the object is exposed to an ELF electric field. In that development we found that the single sideband to carrier ratio of the received signal was (from Eq. 2-26)

$$SSBCR = 20 \log \frac{2\pi x}{\lambda}_0 \qquad (5\text{-}140)$$

where x_0 was the amplitude of the vibration. Replacing x_0 by $\Delta t/2$ in the present case we get

$$SSBCR = 20 \log \frac{\pi \Delta t}{\lambda} \qquad (5\text{-}141)$$

where Δt is the peak to peak vibration amplitude of the front surface of the prismatic bar and λ is the wavelength in nanometers of the X-band oscillator frequency. Evaluating this expression with Δt equal to 0.180 nm as calculated in the previous section we get

$$SSBCR = 20 \log \frac{\pi \cdot 0.180}{28.5 \times 10^6} = -154 \text{ dBc.}$$

This is the signal level that should be measured from the receiver output and this sideband will be at twice the drive frequency as shown in Eq. 5-138. The SSBCR was also calculated for the 3.5 mm and 5.0 mm base half-prolate spheroids and the results are contained in Table 5.3.

5.6 Measurement of Displacement

5.6.1 Experimental Data: Displacement of Half-Prolate Spheroid

In order to test the operation of the receiver with tissue-like samples, three different sized half-prolate spheroid aluminum molds were constructed (Fig. 5-7). The molds were machined to produce half-prolate spheroid samples with minor and major axes of 1 mm and 2 mm, 1.75 mm and 3.5 mm, and 2.5 mm

and 5 mm respectively. These dimensions correspond to "b" and "a" respectively in Figure 5-4. It should be noted that the eccentricity of the prolate spheroid as given by Eq. 5-82 was the same for each sample and had a value of 0.866. In all the experimental data to follow, a 0.6% c Agar solution was used to make the samples and each sample was placed on a 10 x 10 x 0.23 mm steel plate. The sample and plate were then placed in the exposure cell on the broad wall of the X-band waveguide.

The single sideband to carrier ratio (SSBCR) is related to the spectrum analyzer voltage reading in exactly the same way as it was for the vibrating piezoelectric crystal in Section 3.3. In that section we found (Eq. 3-48)

$$SSBCR\Big|_{dB} = V_{anal}\Big|_{dBV} - 65\ dB - 20\ \log\ (2k_{\phi}). \qquad (5\text{-}142)$$

The phase detector constant was determined as in section 3.3 except that the waveguide switch directed the X-band signal to the exposure cell which contained the sample and plate. With the receiver set up for quadrature phase detection the audio oscillator was activated and the signal to the exposure cell center plate was adjusted to 100 V peak to peak which produced an unperturbed sinusoidal electric field with an amplitude of 8,333 V/m.

Half-prolate spheroid samples were molded with 0.6% c Agar and with dimensions specified above. Each was placed in the exposure cell and individually exposed to an 8.333 kV/m electric field over the frequency range of 5 Hz to a maximum of 250 Hz. The measured SSBCR versus vibration frequency for the 2 mm, 3.5 mm and 5 mm base samples are shown in Figures 5-8, 5-9 and 5-10 respectively. On the right vertical axis of each plot the peak to peak vibration amplitude computed from the single sideband carrier ratio is also presented. It should be noted that the abscissa is vibration frequency, not audio oscillator frequency. The data confirmed our expectation that the

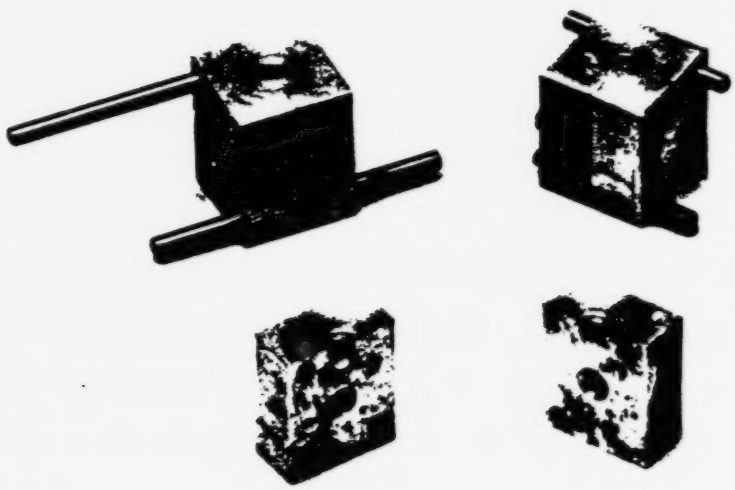

Figure 5-7. Half-Prolate Spheroid Molds.

Table 5-3

Comparisons of Calculated and Measured Vibration Amplitudes in The Sub-Resonant Region for 0.6% Agar Gel Half-Prolate Spheroid Samples on a Ground Plane in an 8.33 kV/m Electric Field

Base Diameter (mm)	Sample	Measured SSBCR (dBc)	Measured Vibration Amplitude pp (nm)	Calculated SSBCR (dBc)	Calculated Vibration Amplitude pp (nm)	Frequency of Major Resonance (Hz)
2.0	1	-133	2.03	-154	0.180	280
2.0	2	-130	2.86	-154	0.180	280
2.0	3	-141	0.809	-154	0.180	250
	mean:	-135				
3.5	1	-140	0.907	-141	0.845	164
3.5	2	-138	1.14	-141	0.845	152
3.5	3	-132	2.28	-141	0.845	142
	mean:	-137				
5.0	1	-128	3.61	-132	2.29	108
5.0	2	-123	6.42	-132	2.29	104
5.0	3	-121	8.09	-132	2.29	106
	mean:	-124				

vibration frequency would be double the audio oscillator frequency as discussed in Section 5.5.4. Each of the samples exhibited at least one resonant frequency but in each case the vibration amplitude approached a constant value as the vibration frequency was reduced. It is in this low frequency, subresonant region where our calculations in Section 5.5.5 can be compared to the measured SSBCR. The calculated value of the SSBCR from Section 5.5.5 for a 3.5 mm base sample is -141 dBc. This compares favorably with the -140 dBc value obtained from Figure 5-9 for the low vibration frequencies.

Three samples of each of the three sizes of the half-prolate spheroids were measured and the results are summarized in Table 5-3. Several observations can be made from the data in the table. There is a fairly large (19 dB) difference between the mean value of the measured SSBCR's for the 2 mm diameter base samples compared to the calculated value whereas this difference is only 4 dB and 8 dB for the 3.5 mm and 5 mm base samples respectively. The reason for the large difference for the smallest sample size was based on the very large return loss of the X-band signal when it reflects back from the 2 mm sample. The return loss of the 2 mm sample and plate when placed in a section of X-band waveguide just in front of an X-band termination with a return loss of 43 dB was about 30 dB. This return loss is comparable to the return loss at X-band of the exposure cell with the empty sample plate (27 dB). This means that the power reflected from the smallest sample is less than the power reflected from the exposure cell. Since the exposure cell is stationary, the signal reflected by the cell is a spectral line at the X-band oscillator frequency. The signal scattered from the vibrating sample on the other hand consists of spectral lines at the carrier frequency and two sidebands at

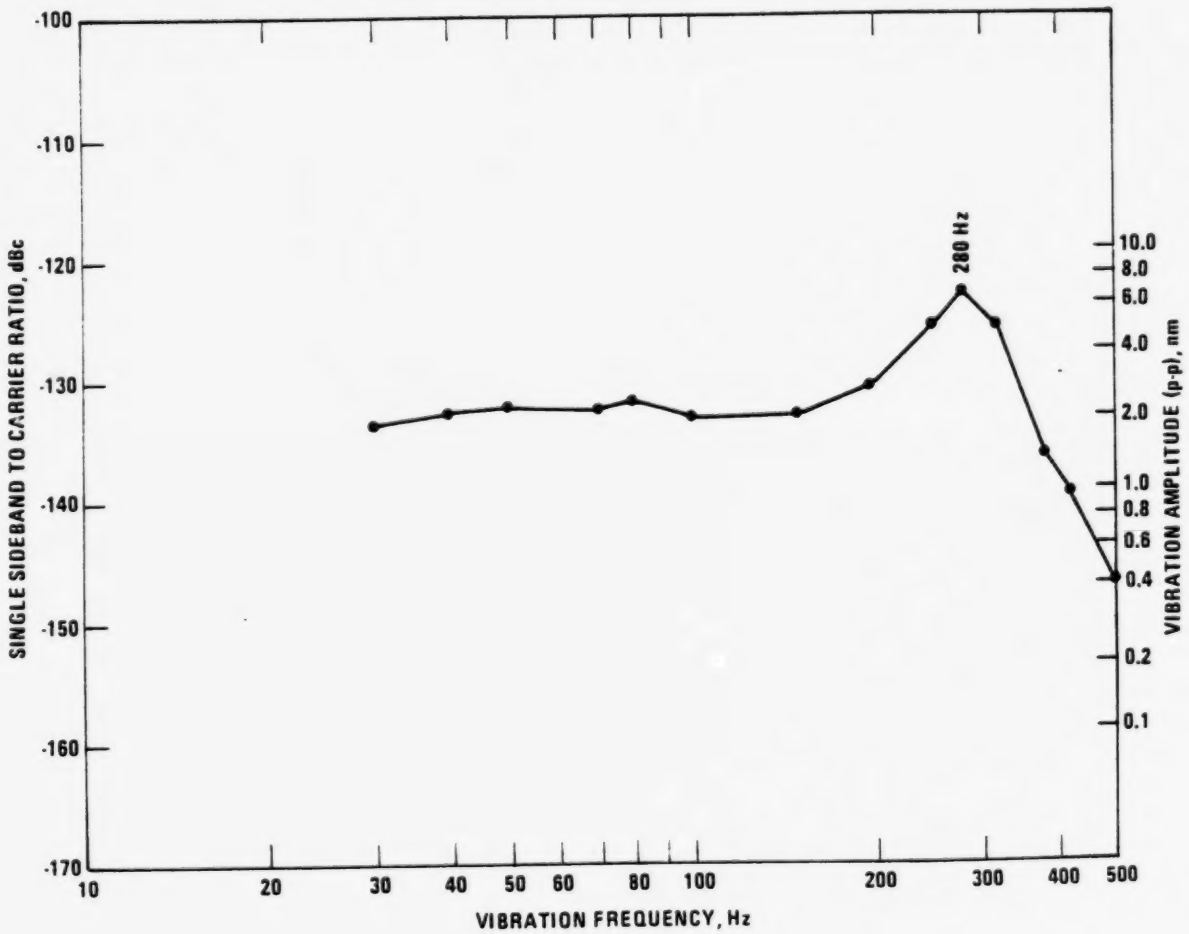

Figure 5-8. Measured Single Sideband to Carrier Ratio and Vibration Amplitude Versus Vibration Frequency for the 0.6% Agar Gel, 2 mm Dia. Base Half-Prolate Spheroid.

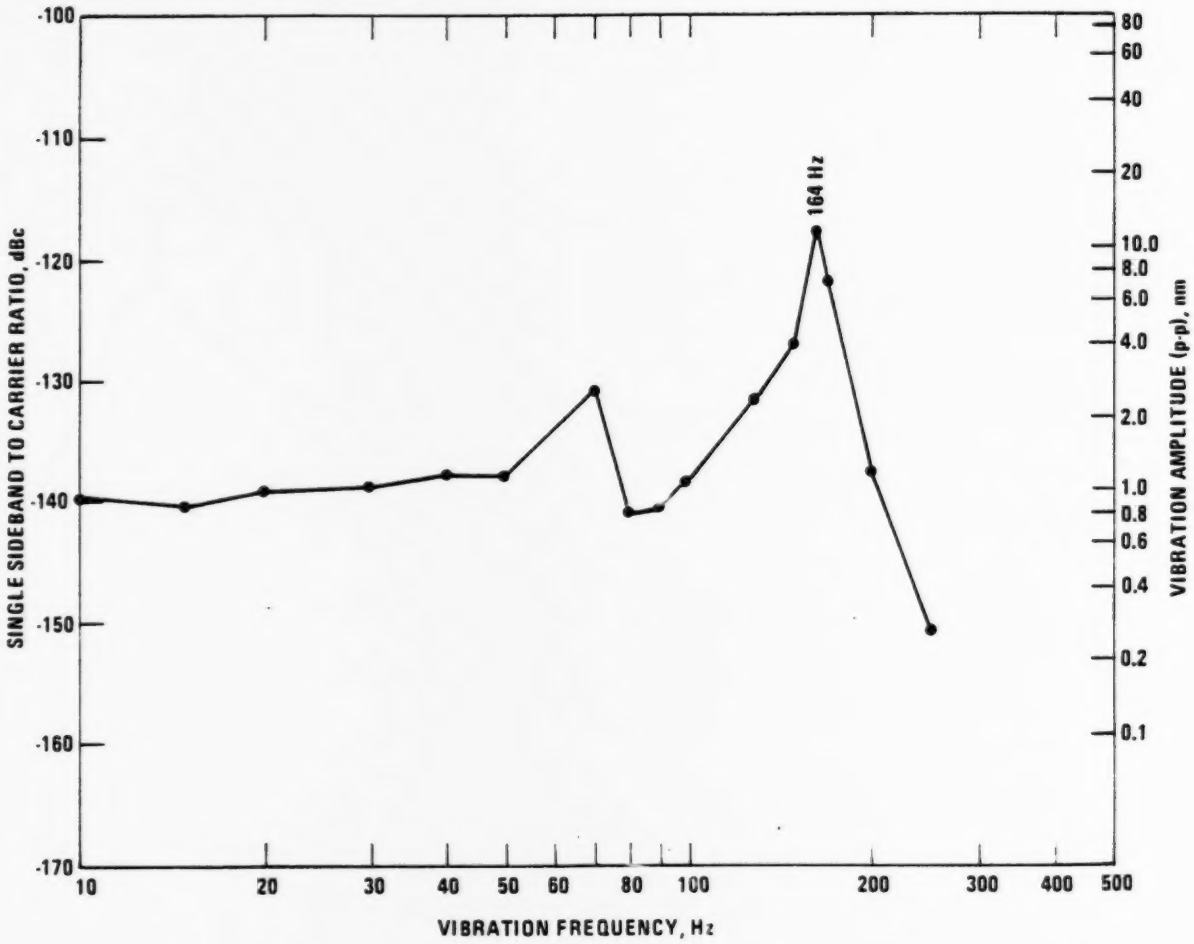

Figure 5-9. Measured Single Sideband to Carrier Ratio and Vibration Amplitude Versus Vibration Frequency for the 0.6% Agar Gel, 3.5 mm Dia. Base Half-Prolate Spheroid.

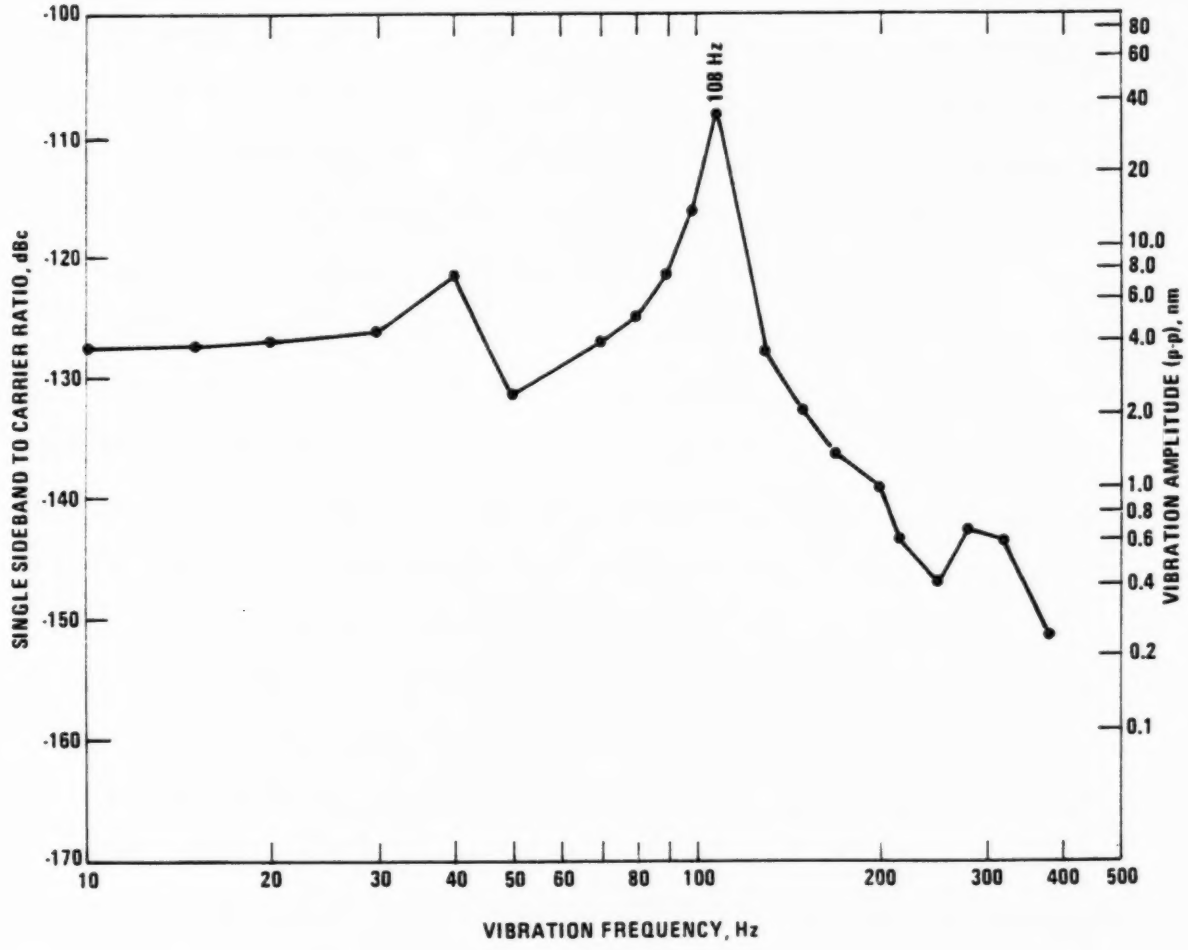

Figure 5-10. Measured Single Sideband to Carrier Ratio and Vibration Amplitude Versus Vibration Frequency for the 0.6 Agar Gel, 5 mm Dia. Base Half-Prolate Spheroid.

either side of the carrier frequency and separated from it by the vibration frequency. The spectral line from the exposure cell reflection will combine with the carrier frequency spectral line from the vibrating sample. If the relative phase between these two signals is 180° apart, a large portion of the carrier frequency spectral line of the vibrating target can be cancelled. This would reduce the magnitude of the measured sideband to carrier ratio and therefore the vibration amplitude would appear larger than it really was. A way to test this hypothesis is to cause the relative phase between these signals to change and to monitor the SSBCR to see if it is altered. A simple way to do this is to place the target at different positions along the length of the exposure cell. This will cause the scattered signal from the target to combine with varying phase differences with the signal reflected from the exposure cell. When this experiment was performed with the 2 mm base sample in the subresonant region with the audio oscillator at 50 Hz, the SSBCR changed by as much as 32 dB. It is for this reason that larger samples were used even though the larger samples cause uncertainty in the effective exposure field as discussed in Section 5.5.4. The return loss of the larger samples on the plate was 10 dB for the 5 mm base sample and 17 dB for the 3.5 mm base sample. Both of these values indicate that the reflection from the samples are considerably larger than the reflection from the exposure cell as desired.

5.6.2 Experimental Data: Resonance Frequencies

The sharp resonances observed in Figures 5-8, 9 and 10 present the opportunity to apply some simple models to possibly determine the type of

Table 5-4

Comparison of the Measured Major Resonance Frequencies of 0.6% Agar Gel Half-Prolate and Cubical Shaped Samples with Those Obtained from Basic Vibration Models of Elastic Bodies

		Resonance Frequencies from Various Models					
(a)	(b)	(c)	(d)	(e)	(f)	(g)	(h)
			Prismatic Bar (One End Fixed)		Transverse Vibration		
Base Width (mm)	Resonance Frequency* (Hz)	Mass-Spring Model (Hz)	Longitudinal (Hz)	Transverse (Hz)	Cyl. Rod (Hz)	Mean of (f,h) (Hz)	Conical Beam (Hz)
Half-Prolate Spheroid							
2.0	270	338	306	143	170	298	425
3.5	153	193	175	82	98	171	243
5.0	106	135	123	57	68.5	119	170
Cube							
2.0	223	338	306	198	NA	NA	NA
4.0	113	169	153	98.9	NA	NA	NA

* mean of three samples

vibration that is occurring. One may start by assuming that the vibration is longitudinal and that the sample can be modeled by a simple harmonic oscillator with a spring with a mass m_1. The resonance frequency of such a system [Sears, 1958, p. 309] is

$$f_0 = \frac{\sqrt{k/(m+m_1/3)}}{2\pi} \tag{5-143}$$

where k is the spring constant and m is the mass attached to the spring. The term k can be found from the defining equation of the Young's modulus:

$$F/A = E\ \Delta\ell/\ell. \tag{5-144}$$

Solving for F we obtain

$$F = \frac{AE}{\ell}\ \Delta\ell \tag{5-145}$$

where A is the cross-sectional area of the sample and ℓ is the length. From Eq. 5-145

$$k = AE/\ell. \tag{5-146}$$

If Eq. 5-146 and 5-143 are applied to the prismatic bar model of the half-prolate spheroid, the resonance frequencies shown in Table 5-4 are obtained. The term "m" in Eq. 5-143 has been set equal to zero in this evaluation because the prismatic bar is only approximated by a spring with mass. The actual resonance frequency does not agree very well with the frequency obtained from this model. One reason for the disagreement is that by setting the mass at the end of the spring equal to zero, the resonance frequency is raised and the assumption that all points of motion in the spring are in phase is no longer valid. In the mass/spring simple harmonic oscillator model the spring is assumed to be short compared to the resonance wavelength. The resonance wavelength can be calculated if the speed of sound in the material is known. This is given by [Timoshenko et al, 1974]:

$$c = \sqrt{E/\rho} \tag{5-147}$$

where ρ is the mass density. For a Young's modulus of 6×10^3 nt/m^2 and a density of 1000 kg/m^3 , the speed of sound in the material is 2.45 m/s. For the observed average resonance frequency for the 2 mm half-prolate spheroid samples of 270 Hz, the length of the samples are about one-fourth wavelength. Therefore travelling waves would exist and a different model must be used.

The model for the free longitudinal vibrations of a uniform bar of length L with one end fixed and the other free yields the following expression for the first resonance frequency [Timoshenko et al, 1974]:

$$f_0 = \frac{\sqrt{E/\rho}}{4L}. \tag{5-148}$$

The results of applying this model are again shown in Table 5-4. For example for the 3.5 mm base sample the observed resonance frequency averaged 153 Hz whereas Eq. 5-148 yielded a value of 175 Hz. While yielding a better agreement with the measured values, application of this model to the half-prolate spheroid is at best a rough approximation. Strictly speaking Eq. 5-148 applies to a prismatic bar with cross-sectional dimensions that are small compared to the length of the bar.

The motion of the half-prolate spheroid could be transverse vibration if the fields in the exposure cell were not symmetrical or if the sample were asymmetrical. The fundamental resonance frequency for transverse vibration of a prismatic bar with one end fixed is given by [Timoshenko et al, 1974]

$$f_1 = \frac{3.515}{\ell^2} \sqrt{gEI/w} \tag{5-149}$$

where w/g is the mass per unit length and I is the second moment of area [Timoshenko et al, 1962] and is given by

$$I = a^4/12 \tag{5-150}$$

where a is the width of the square cross-section of the prismatic bar. Applying Eq. 5-149 with dimensions of the prismatic bar approximation of the half-prolate spheroid in Section 5.5.2 yields the results in Table 5-4. Agreement with the measured data was poor for the model as can be seen from the table.

Timoshenko et al [1974] also consider the transverse vibrations of a cylindrical beam as well as a conical beam with the same length and base. The formula for the fundamental resonance frequencies for the cylindrical beam is

$$f_1 = \frac{1.758r}{2\pi\ell^2} \sqrt{E/\rho} \qquad (5\text{-}151)$$

where r is the radius of the base, and

$$f_1 = \frac{4.359r}{2\pi\ell^2} \sqrt{E/\rho} \qquad (5\text{-}152)$$

for the conical beam. If one visualizes the cross-sectional areas through the vertical axes of the cylindrical beam, the half-prolate spheroid and the conical beam - each with equal heights and bases, it is obvious that the cross-sectional area of the half-prolate spheroid is between the other two shapes. Therefore the transverse resonant frequency of the half-prolate spheroid will be between that of the other two shapes. Another estimate therefore of the transverse vibration resonance frequency can be obtained by averaging the calculated values for the cylindrical beam and the conical beam. These values are shown in Table 5-4 and are in close agreement to the measured resonance frequencies.

In the next series of experiments cubical shaped samples with 2 mm and 4 mm sides were prepared again using 0.6% Agar gels. It was thought that this shape would be closer to the prismatic bar shape required by the models and it is, in the sense that the cross-sectional area is constant along

the height of the cube. However the cubical shape does not meet the criterion that the length of the bar shall be long compared to the cross-sectional dimensions. With these considerations in mind the cubical shaped samples were placed in the exposure cell to see if their resonance frequencies were in closer agreement with the models. Three samples of each of the 2 mm and 4 mm cubical samples were tested and the average of the measured resonance frequencies for each size is presented in Table 5-4. Typical plots of the vibration of a 2 mm cube and a 4 mm cube versus vibration frequency are shown in Figures 5-11 and 5-12 respectively. The resonance frequencies were also calculated using the mass/spring model of Eq. 5-143 and the longitudinal and transverse vibration of a prismatic bar with one end fixed using Eq. 5-148 and Eq. 5-149 respectively.

The experimental data for the cubical samples agree most closely with the transverse bar vibration frequencies and this may indicate that for cubical samples the vibration is transverse. For the half-prolate spheroid samples, the average of the transverse vibration frequency of the rod model and the conical beam model produced close agreement to the experimental data as did the model for the longitudinal vibration of a prismatic bar with one end fixed. Therefore, it is impossible to conclude with certainty from these simple models whether the vibration of the half-prolate spheroid is transverse or longitudinal. However since the net force is oriented along the vertical direction, it is more likely that the longitudinal vibration mode is being excited for the half-prolate spheroid.

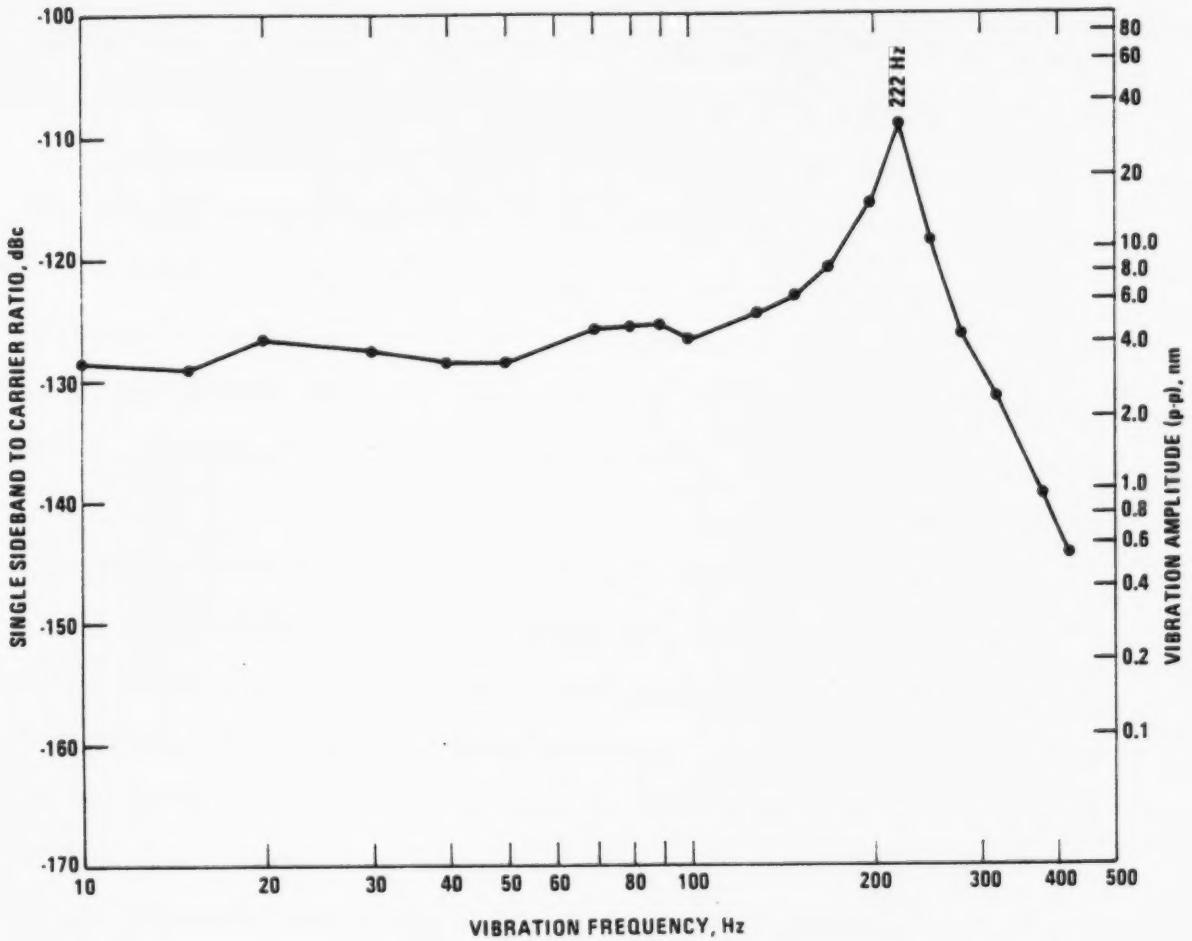

Figure 5-11. Measured Single Sideband to Carrier Ratio and Vibration Amplitude Versus Vibration Frequency for the 0.6% Agar Gel, 2 mm Cube.

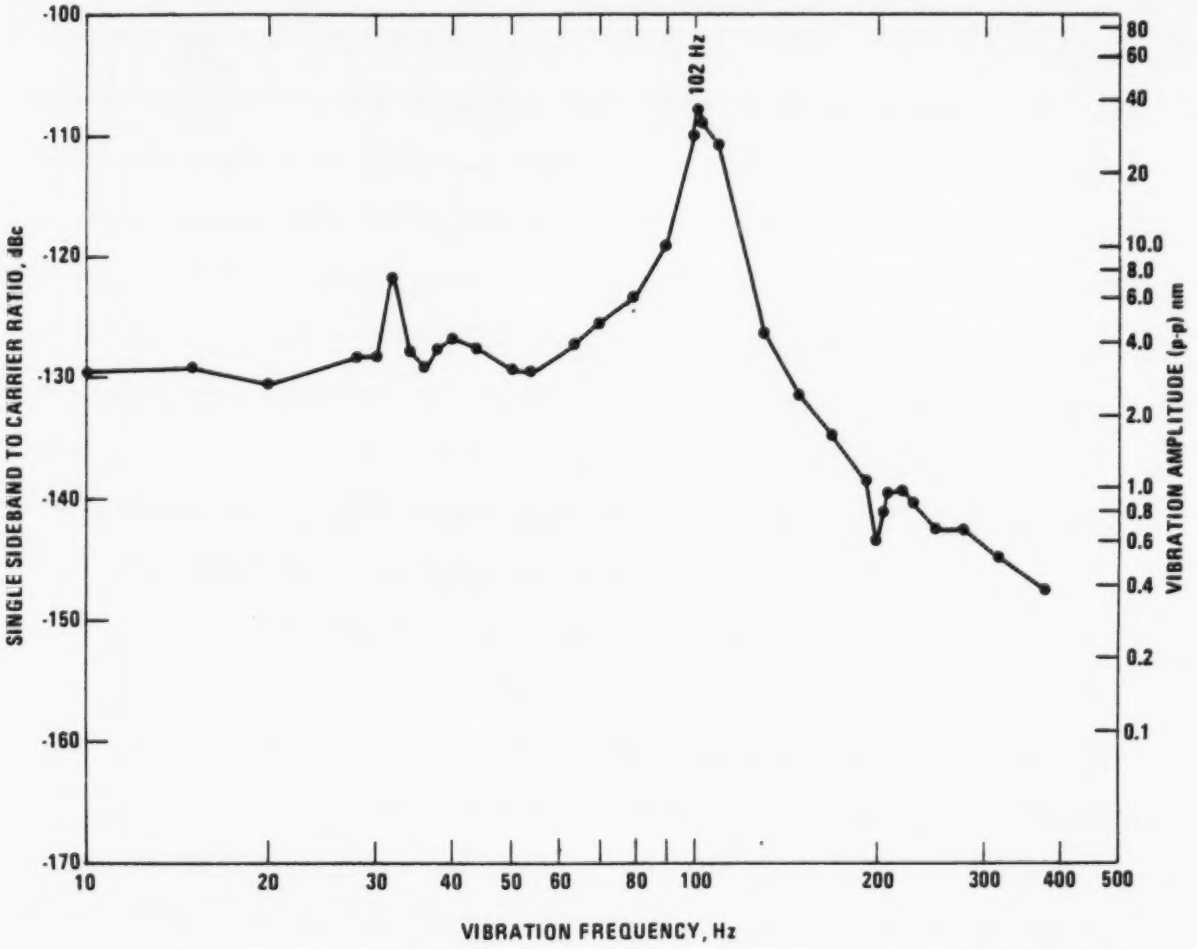

Figure 5-12. Measured Single Sideband to Carrier Ratio and Vibration Amplitude Versus Vibration Frequency for the 0.6% Agar Gel, 4 mm Cube.

Chapter VI

CONCLUSIONS

The characteristics of an RF field scattered from a linearly vibrating object were derived. The scattered signal was shown to be phase modulated with, for sinusoidal vibration, the phase modulation index proportional to the amplitude of the vibration. The spectral characteristics of this signal were derived and it was shown that for a small modulation index, only one pair of sidebands is significant. When the ratio of one sideband to the carrier was formed, this suggested a method of extracting the vibration amplitude information without a knowledge of the reflection coefficient of the vibrating object. The sideband to carrier ratio was shown to be dependent only on the vibration amplitude and the wavelength of the incident field.

Several receivers were considered for the recovery of the vibration information from the received signal. The Doppler transceiver offered the advantages of simplicity and good sensitivity; however the recovery of the vibration amplitude would requires a knowledge of the reflection coefficient of the target and in addition the receiver would have to be a certain distance from the target to establish phase quadrature between the transmitter reference signal and the received signal. The homodyne receiver incorporated a manual phase shifter which eliminates the special target-receiver spacing requirement; however knowledge of the reflection coefficient is still required for quantitative vibration measurements.

The sideband heterodyne receiver with an IF limiting amplifier was selected for the final receiver design because this design permitted quanti-

tative vibration measurements. It was initially thought that this receiver would also provide enhanced sensitivity over the Doppler and homodyne receivers because of the expected improvement in noise figure. However the sensitivity was not improved. Noise figure was not found to be a good measure of receiver sensitivity when the carrier to sideband ratio is large and when the sideband is close to the carrier. When the sensitivity is limited by flicker noise, as it is in this receiver, the actual sensitivity can be considerably less than predicted by the noise figure.

An analysis of the factors limiting sensitivity was performed. Phase noise theory was reviewed as well as modern techniques for its measurement. The quadrature phase detection method for high sensitivity phase noise measurements was described. A system for making quantitative phase noise measurements in terms of the single-sideband phase noise (L(f)) was assembled. The ultimate sensitivity of the quadrature phase detection method is limited by the flicker noise of the phase detector diodes. The sensitivity for the measuring systems used were presented graphically. Key receiver components such as an RF amplifier, the limiting amplifier, the low noise IF amplifier, the RF mixer and the phase detector were all characterized in terms of their residual single-sideband phase noise. The RF amplifier produced an excessive level of residual phase noise. The RF amplifier was therefore not used in the final receiver design because receiver sensitivity would have been degraded severely. The low noise IF amplifier had negligible residual phase noise compared to the limiting amplifier.

The phase detector RF drive level was found to be important for minimizing residual phase noise. For a fixed LO level the absolute level of the noise at the output at baseband frequencies increased with increasing RF drive level. However the phase detector constant increases with an increasing RF

drive level. When the residual phase noise was measured, which is computed from the ratio of the absolute noise level to the phase detector constant, the lowest noise performance was obtained with an RF drive level between 0.6 and 5.0 mW for a 5.5 mW LO drive level.

All oscillators exhibit phase noise and furthermore the oscillators used in this receiver have greater SSB phase noise than most of the other active components. However, because of the correlation effect and the short transit time experienced by a signal travelling from the transmitter to the target and other reflecting objects in the waveguide and back to receiver, the apparent oscillator phase noise is reduced substantially below the level of the phase noise of the other active components in the receiver. Therefore the oscillators do not limit the sensitivity of the receiver in this application. Examination of the single sideband phase noise data revealed that the microwave mixer (M2) and the limiting amplifier were the components that limited the sensitivity of the receiver.

A unique exposure cell was designed to simultaneously expose samples to an ELF or an ELF-modulated RF field while providing for the non-contact vibration monitoring of the sample with an X-band signal. The cell has a return loss of greater than 20 dB up to 1 GHz at the exposure field input port. Properties of the exposure cell however do place limitations on the size of the sample that can be accommodated. If the sample is larger than about one-third of the center plate to wall spacing, charge redistribution increases the effective field to which the sample is exposed. The effective field then becomes a strong function of the sample size and the gap between the object and the center plate and this tends to add large uncertainties to the calculations. If the sample is too small, on the other hand, the return loss of the sample begins to approach the return loss of the empty exposure

cell. When this happens, quantitative measurements become impossible because of an unknown amount of carrier cancellation or augmentation of the signal scattered from the vibrating sample.

Starting with the Lorentz force law, the force per unit area at a dielectric interface due to electrostrictive forces was derived for the cases of the electric fields normal and tangent to the dielectric interfaces. It was shown that for both the electric fields normal or tangent to the dielectric interface, the force at the interface is always directed from the region with the higher dielectric constant to the region with the lower dielectric constant and does not depend on the sign of the electric field. The electric field normal to the surface of a high dielectric constant or conducting prolate spheroid was calculated. From this expression the vertical force on a half-prolate spheroid with its base on a ground plane was derived. Agar gel was used as a mechanical model for tissue. The Young's modulus of agar gel was measured as a function of concentration and the modulus was found to increase linearly with the concentration of agar in deionized water. Poisson's ratio was also experimentally determined for a 0.6% c of agar gel. With these values estimates of the expected vibration amplitude and the expected receiver signals were computed for three sizes of half-prolate spheroid samples exposed to an ELF electric field.

Measured values of vibration amplitude for the half-prolate spheroid samples in a sub-resonant ELF field agreed most closely with the calculated values for the 3.5 mm base sample size. Samples of other sizes differed from the calculated values for the reasons stated above. The measured vibration frequency was always at twice the frequency of the exposure field as predicted by the theory.

The major resonance frequency of both the half-prolate spheroid and cubical samples were measured. Simple models including the simple harmonic oscillator model and others derived for the transverse or longitudinal vibration of continuous systems of standard shapes were applied. The resonance frequencies observed for the cubical-shaped samples agreed most closely to the calculated resonance frequencies for the transverse vibration of a prismatic bar. For the half-prolate spheroid samples it was impossible to conclude with certainty from the simple models employed whether the vibration at the major resonance frequency was longitudinal or transverse.

In conclusion, a receiver with an exposure cell has been designed and characterized that is capable of vibration measurement in the nanometer range. Vibrations in this range were predicted to occur in certain calcium ion efflux studies which demonstrated a biological effect. This system therefore promises to help unravel some of the uncertainty surrounding the interaction of RF fields with biological systems.

Appendix A

CORRELATION EFFECT OR THE REDUCTION IN APPARENT OSCILLATOR NOISE AT CLOSE RANGE

In a radar, a signal is transmitted, reflected by a target and a return signal detected. The time delay for the round trip of the signal is:

$$T = 2R/c \tag{A-1}$$

where R is the range and c is the velocity of light.

Consider a simple CW system as shown in Fig. A-1 where Z is a target. The signal returned to the receiver by the target is assumed to not be a function of range in the analysis below. This assumption is a very good approximation to the actual receiver used in this report.

If the range is large and the oscillator is noisy, the sensitivity of the receiver will be limited by the oscillator noise. A typical spectrum was given in Fig. 3-11. It is evident that the information sideband is lost in the transmitter phase noise. If the range is not large however, all is not lost.

Consider the result of the phase detection of an FM signal with a delayed replica of itself. The transmitted signal is

$$v_t = \sin\left(2\pi f_0 t + \frac{\Delta f}{f_m} \sin 2\pi f_m t\right) \tag{A-2}$$

where f_0 is the carrier frequency, f_m is the modulating frequency and Δf is

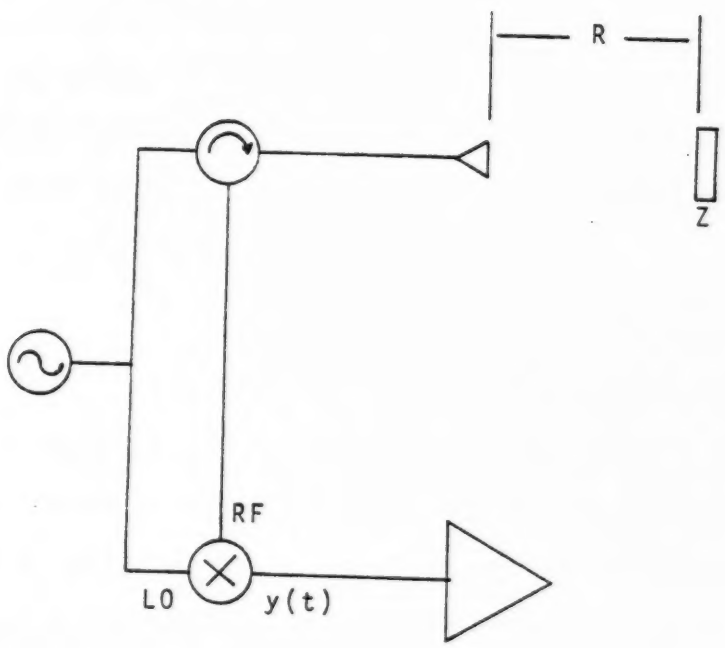

Figure A-1. A Simple Radar System for Analysis of the Correlation Effect.

the frequency deviation constant. Then

$$v_r = \sin(2\pi f_0(t-T) + \frac{\Delta f}{f_m} \sin 2\pi f_m(t-T)). \tag{A-3}$$

The phase detector output, $y(t)$, is

$$y = \sin \phi(t) \tag{A-4}$$

where ϕ is the phase difference between the received signal and the oscillator signal. Expanding Eq. A-4 using Eq. A-2 and A-3 we get

$$y(t) = \sin\{2\pi f_0 t + \frac{\Delta f}{f_m} \sin 2\pi f_m t - 2\pi f_0(t-T) - \frac{\Delta f}{f_m} \sin 2\pi f_m(t-T)\}$$

$$= \sin\{2\pi f_0 t + \frac{\Delta f}{f_m} \sin 2\pi f_m t - 2\pi f_0 t + 2\pi f_0 T - \frac{\Delta f}{f_m} \sin 2\pi f_m(t-T)\}$$

$$= \sin\{\frac{\Delta f}{f_m}[\sin 2\pi f_m t - \sin 2\pi f_m(t-T)] + 2\pi f_0 T\} \tag{A-5}$$

$$\sin 2\pi f_m(t-T) = \sin 2\pi f_m t \cos 2\pi f_m T - \cos 2\pi f_m t \sin 2\pi f_m T \tag{A-6}$$

$$y(t) = \sin\{\frac{\Delta f}{f_m}[\sin 2\pi f_m t - \sin 2\pi f_m t \cos 2\pi f_m T + \cos 2\pi f_m t \sin 2\pi f_m T] + 2\pi f_0 T\}$$

$$= \sin\{\frac{\Delta f}{f_m}[\sin 2\pi f_m t(1-\cos 2\pi f_m T) + \cos 2\pi f_m t \sin 2\pi f_m T] + 2\pi f_0 T\} \tag{A-7}$$

$$1 - \cos 2\pi f_m T = 2 \sin^2 \pi f_m T \tag{A-8a}$$

$$\sin 2\pi f_m T = 2 \sin \pi f_m T \cos \pi f_m T \tag{A-8b}$$

$$y(t) = \sin\{\frac{\Delta f}{f_m}[2 \sin 2\pi f_m t \sin^2 \pi f_m T + 2 \cos \pi f_m t \sin \pi f_m T \cos \pi f_m T] + 2\pi f_0 T\}$$

$$= \sin\{2\frac{\Delta f}{f_m} \sin \pi f_m T[\sin 2\pi f_m t \sin \pi f_m T + \cos 2\pi f_m t \cos \pi f_m T] + 2\pi f_0 T\} \tag{A-9}$$

$$y(t) = \sin\{2\frac{\Delta f}{f_m} \sin \pi f_m T[\cos 2\pi f_m t \cos \pi f_m T + \sin 2\pi f_m t \sin \pi f_m T]$$

$$+2\pi f_0 T\}$$

$$= \sin\{2\frac{\Delta f}{f_m} \sin \pi f_m T[\cos(2\pi f_m t - \pi f_m T)] + 2\pi f_0 T\}$$

$$= \sin\{2\frac{\Delta f}{f_m} \sin \pi f_m T[\cos 2\pi f_m (t-T/2)] + 2\pi f_0 T\}. \quad \text{(A-10)}$$

This equation is of the form

$$y(t) = \sin(\gamma\cos\theta + \phi) \quad \text{(A-11)}$$

where

$$\gamma = 2\frac{\Delta f}{f_m} \sin \pi f_m T \quad \text{(A-12a)}$$

$$\theta = 2\pi f_m (t-T/2) \quad \text{(A-12b)}$$

$$\phi = 2\pi f_0 T\}. \quad \text{(A-12c)}$$

Equation A-11 can be expanded:

$$y(t) = \cos\phi \sin(\gamma\cos\theta) + \sin\phi \cos(\gamma\cos\theta) \quad \text{(A-13)}$$

$$\sin(\gamma\cos\theta) = 2\sum_{n=1}^{\infty}(-1)^{n+1} J_{2n-1}(\gamma)\cos(2n-1)\theta \quad \text{(A-14a)}$$

$$\cos(\gamma\cos\theta) = J_o(\gamma) + 2\sum_{n=1}^{\infty}(-1)^n J_{2n}(\gamma)\cos 2n\theta\ . \quad \text{(A-14b)}$$

For small γ

$$J_0(\gamma) \approx 1;\ J_1(\gamma) \approx \gamma/2;\ J_{2,3}\ldots = 0 \quad \text{(A-15)}$$

$$y(t) \approx \sin\phi + \frac{2\cdot 2\Delta f}{2f_m} \sin(\pi f_m T)\cos 2\pi f_m (t-T/2)\cos\phi. \quad \text{(A-16)}$$

Choosing ϕ such tnat $\cos\phi = \sin\phi$ the power ratio of the sideband to the DC term is

$$P_{SB}/P_{DC} = \frac{[2(\Delta f/\sqrt{2}f_m)\sin(\pi f_m T)]^2}{1} \quad \text{(A-17)}$$

For $\pi f_m T \ll 1$, ie short transit time

$$2(\Delta f/f_m)^2 \sin^2(\pi f_m T) \simeq 2(\Delta f/f_m)^2(\pi f_m T)^2 \quad \text{(A-18)}$$

or

$$P_{SB}/P_{DC} \simeq 2(\Delta f/f_m)^2(\pi f_m T)^2 \quad \text{(A-19)}$$

Eq. A-19 shows that the noise out of the phase detector due to the oscillator noise goes to zero as the path delay, T, approaches zero. The term $(\Delta f/f_m)^2$ is related to the single sideband phase noise, L(f), of the source

$$L(f) = [\Delta\phi/2]^2\Big|_{1 \text{ Hz bandwidth}} \quad \text{(A-20)}$$

$$\Delta\phi = \Delta f/f_m \quad \text{(A-21)}$$

$$L(f) = [\Delta f/2f_m]^2\Big|_{1 \text{ Hz bandwidth}} \quad \text{(A-22)}$$

$$P_{SB}/P_{DC} = 2 \cdot 4[\Delta f/2f_m]^2(\pi f_m T)^2 = [\Delta f/2f_m]^2 \times 8(\pi f_m T)^2 \quad \text{(A-23)}$$

$$P_{SB}/P_{DC} = L(f) \cdot 8(\pi f_m T)^2 \quad \text{(A-24)}$$

Eq. A-24 shows that L(f), the single sideband phase noise, is reduced by the factor $8(\pi f_m T)^2$ for small values of $f_m T$, at the phase detector output.

Converting to dB:

$$P_{SB}/P_{DC}\Big|_{dB} = L(f)\Big|_{dB} + 10 \log 8\pi^2 + 20 \log(f_m T) \quad \text{(A-25)}$$

$$P_{SB}/P_{DC}\Big|_{dB} = L(f)\Big|_{dB} + 19 \text{ dB} + 20 \log(f_m T) \quad \text{(A-26)}$$

The reduction in apparent noise is given by the terms

$$\text{Reduction} = 19 \text{ dB} + 20 \log(f_m T)$$

This factor is evaluated in Table A-1.

Table A-1

Apparent Reduction in Oscillator Noise

$f_m T$(radians)	Reduction Factor (dB)
10^{-9}	-161
10^{-8}	-141
10^{-7}	-121
10^{-6}	-101
10^{-5}	-81
10^{-4}	-61
10^{-3}	-41

References

Abramowitz, M. and I.A. Stegun, eds., "Handbook of Mathematical Functions," National Bureau of Standards, Applied Mathematics Series, Vol. 55, US Gov't. Print. Office, December, 1972.

Adey, W.R., "Tissue Interactions with Nonionizing Electromagnetic Fields," Physiological Reviews, Vol. 61, pp 435-514, April, 1981.

Alexander, P.M., "Frequency Modulated (FM) and Amplitude Modulated (AM) in Millimeter Radar Due to Vibrating Structures," Millimeter Optics, Proc. Soc. Photo-Opt. Instru. Eng., Vol. 259, pp 172-178, 1980.

Anand, Y., "Low-Frequency Noise in Schottky-Barrier Diodes," Proc. IEEE, Vol. 57, No. 5, pp 855-856, May, 1969.

Barnes, F.S., "Model for Some Nonthermal Effects of Radio and Microwave Fields on Biological Membranes," IEEE Trans. Microwave Theory Tech., Vol. MTT-25, No. 9, pp 742-746, September, 1977.

Bawin, S.M., W.R. Adey, and I.M. Sabbot, "Ionic Factors in Release of Calcium from Chick Cerebral Tissue by Electromagnetic Fields," Proc. Natl. Acad. Sci., USA 75, pp 6314-6318, 1978.

Bawin, S.M., L.K. Kaczmarek, and W.R. Adey, "Effects of Modulated VHF Fields on the Central Nervous System," Ann. NY Acad. Sci., Vol. 247, pp 74-81, February, 1975.

Blackman, C.F., S.G. Benane, J.A. Elder, D.E. House, J.A. Lampe, and J.M. Faulk, "Induction of Calcium-Ion Efflux from Brain Tissue by Radiofrequency Radiation: Effect of Sample Number and Modulation Frequency on the Power-Density Window," Bioelectromagnetics, Vol. 1, No. 1, pp 35-43, 1980.

Blackman, C.F., S.G. Benane, L.S. Kinney, W.T. Joines, and D.E. House, "Effects of ELF Fields on Calcium-Ion Efflux from Brain Tissue In Vitro," Radiation Research, Vol. 92, pp 510-520, 1982.

Blackman, C.F. and B.S. Wilson, "Distribution of Label in Studies of the Effects of Nonionizing Radiation on the Association of Calcium Ions with Brain Tissue," in Abstracts, The Bioelectromagnetics Society 5th Annual Scientific Session, p 73, Boulder, Colo., June 12-17, 1983.

Bramanti, M., "Some Experiments on the use of Microwaves to Detect Targets in Watery Dielectrics," Alta Frequenza, Vol. 50, No. 2, pp 106-112, Mar/Apr, 1981.

Brown, P.V.K. and N.C. Wyeth, "Laser Interferometer for Measuring Microwave-Induced Motion in Eye Lenses In Vitro," Rev. Sci. Instrum., Vol. 54, No. 1, pp 85-89, January, 1983.

Buchan, P.B. and D.B. Sattelle, "A Radar-Doppler Autocorrelation Analysis of Insect Activity," Physiol. Entomol., Vol. 4, No. 2, pp 103-109, 1979.

Carlson, A.B., "Communication Systems," McGraw-Hill Book Co., Inc., New York, 1975.

Cohn, S.B., "Shielded Coupled-Strip Transmission Line," IRE Trans. Microwave Theory Tech., Vol. MTT-3, pp 28-38, October, 1955.

Crawford, M.L., "Generation of Standard EM Fields Using TEM Transmission Cells," IEEE Trans. Electromagn. Compat., Vol. EMC-16, No. 4, pp 189-195, November, 1974.

Delgado, J.M.R., J. Leal, J.L. Monteagudo, and M.G. Gracia, "Embryological Changes Induced by Weak, Extremely Low Frequency Electromagnetic Fields," J. Anat., Vol. 134, No. 3, pp 533-551, 1982.

Drain, L.E., "The Laser Doppler Technique," John Wiley and Sons, Inc., New York, 1980.

Drake, A.D. and D.C. Leiner, "Fiber-Optic Interferometer for Remote Subangstrom Vibration Measurement," Rev. Sci. Instrum., Vol. 55, No. 2, pp 162-165, February, 1984.

Griffin, D.W., "MW Interferometers for Biological Studies," Microwave J., Vol. 21, pp 69-72, May, 1978.

Gruner, L., "Estimating Rectangular Coax Cutoff," Microwave J., Vol. 22, No. 4, pp 88-92, April, 1979.

Hewlett-Packard Co., Inc., "Applications and Measurements of Low Phase Noise Signals Using the 8662A Synthesized Signal Generator," Application Note 283-1, November, 1981.

Hewlett-Packard Co., Inc., "Flicker Noise in Schottky Diodes," Application Note 956-3, November, 1974.

Hildebrand, F.B., "Advanced Calculus for Applications," Prentice-Hall, Inc., Englewood Cliffs, N.J., 1962.

Joines, W.T., "The Characteristic Impedance of Symmetrical Strip Transmission Lines with Undesired Modes Suppressed," Ph.D. Dissertation, Duke Univ., Durham, N.C., May, 1964.

Joines, W.T. and B.S. Wilson, "Field-Induced Forces at Dielectric Interfaces as a Possible Mechanism of RF Hearing Effects," Bull. of Math. Biol. (GB), Vol. 43, No. 4, pp 401-413, 1981.

Kleinman, R.E. and R.B. Mack, "Scattering by Linearly Vibrating Objects," IEEE Trans. Ant. Prop., Vol. AP-27, No. 3, pp 344-352, May, 1979.

Kremer, F., C. Koschnitzke, L. Santo, P. Quick, and A. Poglitsch, "The Non-Thermal Effect of Millimeter Wave Radiation on the Puffing of Giant Chromosomes," in "Coherent Exitation in Biological Systems," H. Frohlich and F. Kremer, eds., Springer-Verlag, New York, 1983.

Lerner, E.J., ed., "Biological Effects of Electromagnetic Fields," IEEE Spectrum, pp 57-69, May, 1984.

Lin, J.C., "Microwave Induced Hearing: Some Preliminary Theoretical Observations," J. Microwave Power, Vol. 11, No. 3, pp 295-298, 1976.

Luymes, B.J., "Interferometric Measurements of Very Small Electrostrictive Strains," Rev. Sci. Instrum., Vol. 54, No. 1, pp 90-92, January, 1983.

Manassewitsch, V., "Frequency Synthesizers," John Wiley and Sons, Inc., New York, 1980.

Marsden, C.A. and B. King, "The Use of Doppler Shift Radar to Monitor Physio-Logical and Drug Induced Activity Patterns in the Rat," Pharmacol. Biochem. and Behav., Vol. 10, No. 5, pp 631-635, May, 1979.

Paris, D.T. and F.K. Hurd, "Basic Electromagnetic Theory," McGraw-Hill, Inc., New York, 1969.

Payne, J.B., "Three Techniques for Measuring and Interpreting Short-Term Frequency Stability," Communication Techniques, Inc., Appl. Note, June, 1982.

Prouty, B. and J. Gibbs, "Using Phase Noise Measurements to Improve Performance," Microwave J., Vol. 24, No. 12, pp 47-56, December, 1981.

Ramo, S., J.R. Whinnery, and T. Van Duzer, "Fields and Waves in Communication Electronics," John Wiley and Sons, Inc., New York, 1965.

Schwan, H., "Microwave Radiation: Biophysical Considerations and Standards Criteria," IEEE Trans. Biomed. Eng., Vol. BME-19, No. 4, pp 304-312, July, 1972.

Sears, F.W., "Mechanics, Wave Motion, and Heat," Addison-Wesley Publishing Co., Inc., Reading, Mass., 1958.

Shoaf, J.H., D. Halford, and A.S. Risely, "Frequency Stability Specification and Measurement: High Frequency and Microwave Signals," National Bureau of Standards, Boulder, Colo. NBS Technical Note 632, January, 1973.

Shreve, J.S., "Clutter Spreading Due to Oscillator Instability in Low Elevation Stationary Radars," Harry Diamond Labs, Washington, D.C., HDL Report No. R-510-66-2, June 1, 1966.

Sillars, R.W., "The Properties of a Dielectric Containing Semiconducting Particles of Various Shapes," Jour. IEEE (GB), Vol. 80, pp 378-394, 1937.

Skolnik, M.I., "Introduction to Radar Systems," McGraw-Hill Book Co., Inc., New York, 1962.

Skolnik, M.I., ed., "Radar Handbook", McGraw-Hill, Inc., New York, 1970.

Soderquist, D., "Keep Your Op-Amp Circuits Quiet," Electronic Design, Vol. 20, pp 88-93, September 27, 1975.

Spiegel, R.J., Personal Communication, 1983.

Spiegel, R.J., W.T. Joines, and C.F. Blackman, "Calcium Efflux From Isolated Brain Tissue: Is It Caused by Electromagnetically Induced Pressure on the Brain?", Abstracts of the 4th Annual Meeting Bioelectromagnetics Society, Los Angeles, Calif., p 3, June 28 to July 2, 1982.

Stuchly, S.S., M. Goldberg, A. Thansandote, and B. Carraro, "Monitoring of Arterial Wall Movement by Microwave Doppler Radar," Proc. 1978 Symp. on Electromag. Fields in Biol. Systems, Ottawa, Canada, June 28-30, 1978, pp 229-242. Publ.: IMPI Ltd., Edmonton, Canada, 1979.

Thansandote, A., S.S. Stuchly, and J.S. Wight, "Microwave Interferometer for Measurements of Small Displacements," IEEE Trans. Instrum. Meas., Vol. IM-31, No. 4, pp 227-232, December, 1982.

Timoshenko, S. and D.H. Young, "Elements of Strength of Materials," D. Van Nostrand Co., Inc., Princeton, N.J., 1962.

Timoshenko, S., D.H. Young, and W. Weaver, Jr., "Vibration Problems in Engineering," John Wiley and Sons, Inc., New York, 1974.

Weast, R.C., S.M. Selby, and C.D. Hodgman, eds., "Handbook of Chemistry and Physics," Chemical Rubber Co., Cleveland, Ohio, 1964.

Weil, C.M., "The Characteristic Impedance of Rectangular Transmission Lines with Thin Center Conductor and Air Dielectric," IEEE Trans. Microwave Theory Tech. Vol. MTT-26, No. 4, pp 238-242, April, 1978.

Weil, C.M., W.T. Joines, and J.B. Kinn, "Frequency Range of Large-Scale TEM Mode Rectangular Strip Lines," Microwave J., Vol. 24, No. 11, pp 93-100, November, 1981.